



TECHNISCHE
UNIVERSITÄT
WIEN
Vienna | Austria



DISSERTATION

Optimal control with radial force compensation for multiphase permanent magnet synchronous machines under multiple open-circuit faults

Ausgeführt zum Zwecke der Erlangung des akademischen Grades eines
Doktors der technischen Wissenschaften (Dr. techn.)

unter der Leitung von
Associate Prof. Dr.-Ing. Wolfgang KEMMETMÜLLER
Institut für Automatisierungs- und Regelungstechnik
E376

eingereicht an der
Technischen Universität Wien
Fakultät für Elektrotechnik und Informationstechnik

von
René LENZ
Matrikelnummer: e1429765

Wien, im Mai 2024

Studiendekan

Univ.-Prof. Dr.sc. Silvan SCHMID

Betreuer

Associate Prof. Dr.-Ing. Wolfgang KEMMETMÜLLER

Tag des Rigorosums

20.06.2024

Prüfungsvorsitzender

O.Univ.-Prof. Dr.techn. Manfred SCHRÖDL

Erster Gutachter

Prof. Dr.-Ing. Harald ASCHEMANN

Zweiter Gutachter

Univ.-Prof. Dr.techn. Andreas KUGI

Vorwort

Die vorliegende Dissertation ist im Zuge meiner Tätigkeit als wissenschaftlicher Mitarbeiter am Institut für Automatisierungs- und Regelungstechnik (ACIN) der Technischen Universität Wien entstanden. Die abwechslungsreichen Arbeiten in Forschung und Lehre haben mir viel Freude bereitet und durch die spannenden Herausforderungen habe ich mein Wissen stetig erweitert. Dabei konnte ich auf die vielzählige Unterstützung aus meinem beruflichen und privaten Umfeld bauen, für die ich mich herzlich bedanke.

Mein besonderer Dank gilt meinem Doktorvater Wolfgang Kemmetmüller für sein Vertrauen und die exzellente Betreuung. Seine fachliche Expertise und zielführenden Diskussionen zusammen mit einer raschen Gesprächsbereitschaft bei auftretenden Fragen haben wesentlich zum Gelingen dieser Arbeit beigetragen.

Andreas Kugi danke ich für die angenehmen Rahmenbedingungen am Institut, die Gesprächsbereitschaft und die Begutachtung meiner Dissertation. Ebenso danke ich Harald Aschemann für die Begutachtung meiner Dissertation.

Ich danke meinen aktuellen und ehemaligen Kolleginnen und Kollegen vom ACIN für ihre Hilfsbereitschaft, die angenehme Arbeitsatmosphäre und den spannenden Austausch zu den unterschiedlichsten Themen der Regelungstechnik. Besonders danke ich meinen langjährigen Bürokollegen Thomas Hausberger und Gerd Fuchs für den intensiven Gedankenaustausch zu jeglichen Themen.

Für die Unterstützung bedanke ich mich bei meinen Ansprechpartnern Ludwig Rossmeier, Alexander Ulbing und Dieter Härle vom Industriepartner Infineon Technologies AG und der KAI GmbH.

Für die abwechslungsreichen Momente außerhalb der Universität danke ich meinen Freundinnen und Freunden. Mein besonderer Dank gilt meiner Familie für ihre langjährige Begleitung, Inspiration und Unterstützung auf meinem bisherigen universitären Lebensabschnitt und darüber hinaus. Dieser bedingungslose Rückhalt ist eine große Stütze und hat maßgeblich zum Erfolg meiner Dissertation beigetragen.

Kurzzusammenfassung

Systemzuverlässigkeit und Ausfallsicherheit sind zentrale Themen für elektrische Antriebe in sicherheitskritischen Anwendungen der Industrie- und Automobilbranche. Stromkreisunterbrechungsfehler, engl. open-circuit (OC) faults, sind häufige Fehler in elektrischen Maschinen, die deren elektrische Freiheitsgrade reduzieren. Dies führt zu einem Leistungsabfall und zu unerwünschten Radialkräften, die wiederum Vibrationen und Lärm verursachen, bis hin zu einem Totalausfall des Antriebes. Mehrphasige Maschinen bieten zusätzliche Freiheitsgrade für den Betrieb, womit die Fehlerauswirkungen abgeschwächt werden können.

In dieser Arbeit wird eine optimale, fehlertolerante und echtzeitfähige Regelungsstrategie für mehrphasige Permanentmagnet-Synchronmaschinen (PMSM) unter Berücksichtigung mehrfacher Stromkreisunterbrechungsfehler präsentiert. Rastmomente, magnetische Sättigung und höhere harmonische Schwingungen sind die wichtigsten nichtlinearen Effekte der untersuchten PMSM. Die 12 individuell ansteuerbaren Einzelzahn-Statorwicklungen bieten die Flexibilität, verschiedene elektrische Spulenverschaltungen bei gleichem magnetischen Verhalten zu untersuchen und zu vergleichen. Für diese PMSM wird ein modellbasierter Ansatz für die Regelungsstrategie verwendet. Die dafür erforderliche Modellstruktur besteht aus einem nichtlinearen, magnetischen Reluktanznetzwerk, engl. magnetic equivalent circuit (MEC), welches systematisch alle relevanten magnetischen Eigenschaften abbildet. Die benötigte flexible Struktur zur Berücksichtigung verschiedener elektrischer Spulenverschaltungen und mehrfachen Stromunterbrechungsfehlern ist durch ein elektrisches Modell gegeben, das mit dem Reluktanznetzwerk kombiniert wird. Auf der Grundlage dieses flexiblen Modells werden Optimalströme mit Hilfe eines Optimierungsproblems berechnet, das die beiden klassischen Regelungsziele Drehmomentabweichung und Verlustleistung minimiert. Darüber hinaus werden dank der zusätzlichen Freiheitsgrade auch die auftretenden Radialkräfte im Falle von Stromkreisunterbrechungsfehlern minimiert. Diese optimierten Ströme werden approximiert und effizient in Lookup Tabellen gespeichert, um die Echtzeitfähigkeit zu gewährleisten. Die Herausforderungen für die Fehlerdiagnose und die fehlerto-

lerante Regelung, engl. fault-tolerant control (FTC), ergeben sich aus den höheren harmonischen Komponenten, die in den Referenzstrommustern enthalten sind.

Ein schnelles und zuverlässiges Fehlerdiagnoseverfahren wird entwickelt, das auf den Eigenschaften der Phasenstrommessungen im Zeitbereich beruht. Dabei sind keine zusätzlichen Sensoren oder Vorkenntnisse über die Verschaltungen der elektrischen Spulen oder Phasensysteme erforderlich. Bei einer Fehlerdiagnose wird die fehlertolerante Regelungsstrategie angepasst, um die Auswirkungen des Fehlers zu reduzieren. Die fehlertolerante Regelungsstrategie besteht aus einem nichtlinearen Vorsteuerungsterm, einem PI-Feedbackregler und einem iterativ lernenden Regelungskonzept, engl. iterativ learning control (ILC) strategy, um eine hohe Regelgüte auch bei unbekanntem, nichtlinearem Verhalten des Wechselrichters, engl. voltage source inverter (VSI), zu gewährleisten.

Anhand von Experimenten auf dem Prüfstand wird die Leistungsfähigkeit des Fehlerdiagnoseverfahrens und der fehlertoleranten Regelungsstrategie demonstriert. Insbesondere werden einfache, doppelte und dreifache Stromunterbrechungsfehler für ein viermal dreiphasiges System (4×3 -Konfiguration) und ein zwölfphasiges System (1×12 -Konfiguration) untersucht. Mit dem Fehlerdiagnoseverfahren werden alle untersuchten Stromunterbrechungsfehler erfolgreich innerhalb von 41 % einer Stromgrundwellenperiode erkannt und die Robustheit ist auch unter Lastwechseln gegeben. Durch die fehlertolerante Regelungsstrategie können die Stromfehler im eingeschwungenen Zustand auf das Zweifache der Stromsensorrauschamplitude reduziert werden. Mit dieser hohen Regelgüte können die in den Referenzströmen inkludierten Regelungsziele genau umgesetzt werden. In den untersuchten Szenarien für einfache, doppelte und dreifache Stromunterbrechungsfehler können bei gleichbleibender Drehmomentgenauigkeit die Radialkräfte um über 90 % reduziert werden. Ein umfassender Vergleich zwischen der 4×3 -Konfiguration und der 1×12 -Konfiguration unterstreicht die Vorteile der höheren Freiheitsgrade im Falle der 1×12 -Konfiguration, resultierend in höherer Radialkraftkompensation bei geringeren Verlustleistungen.

Abstract

System reliability and fault tolerance are vital issues for electric drives in safety-critical applications of the industrial and automotive sectors. Open-circuit (OC) faults in electric machines are common faults that decrease the machines' electrical degrees of freedom (DOFs), leading to a deterioration in performance and undesired radial forces that cause vibrations and noise, up to a total failure of the drive. Multiphase machines provide additional DOFs for the control of the machine, which allows to mitigate the impact of OC faults.

This work presents a real-time optimal fault-tolerant control (FTC) strategy for multiphase permanent magnet synchronous machines (PMSMs) considering multiple OC faults. Cogging torque, magnetic saturation, and non-fundamental wave behavior are the main nonlinear effects of the investigated PMSM. The 12 individually controllable single tooth stator windings offer the flexibility to study and compare different electrical coil interconnections while maintaining equal magnetic behavior. For this PMSM, a model-based approach is used for the FTC strategy. The required model structure consists of a nonlinear magnetic equivalent circuit (MEC), which systematically considers all relevant magnetic properties. The flexible structure required to consider different electrical coil connections and multiple OC fault cases is provided by an electrical model that is combined with the MEC. Based on this flexible model, the optimal currents are calculated by an optimization problem that minimizes the classical two control goals of torque tracking error and power loss. Furthermore, and thanks to the additional DOFs, the radial forces in the event of OC fault are also minimized. These optimized currents are then approximated and stored efficiently in lookup tables to ensure real-time capability. The challenges for fault diagnosis and fault-tolerant control arise from the higher harmonic components included within the reference current patterns.

A fast and reliable fault diagnosis method is developed based on the time-domain properties of the phase current measurements. Thereby, no additional sensors or prior knowledge about the electrical coil interconnections or phase systems are required. A successful fault diagnosis adapts the FTC strategy to mitigate the fault impact. The FTC strategy consists of a nonlinear feedforward term, a PI-

based feedback controller, and an iterative learning control (ILC) concept to ensure a high control performance even for unknown nonlinear voltage source inverter (VSI) behavior.

With experiments on a test stand, the performances of the fault diagnosis method and the FTC strategy are demonstrated. In particular, single, double, and triple OC faults are investigated for the quadruple three-phase system (4×3 configuration) and a twelve-phase system (1×12 configuration). With the fault diagnosis method, all investigated OC faults are successfully diagnosed within 41 % of a fundamental current period, and the robustness is also given under load changes. Thanks to the FTC strategy, the current tracking errors in the steady state are two times the current sensor noise amplitude. With this high control accuracy, the control goals included in the reference currents can be precisely implemented. In the scenarios investigated for single, double, and triple OC fault cases, the radial forces can be reduced by over 90 % while maintaining the same torque accuracy. A comprehensive comparison between the 4×3 configuration and the 1×12 configuration pronounces the advantages of the higher available DOFs in the case of the 1×12 configuration, resulting in higher radial force compensation with lower power losses.

Contents

1	Introduction	1
1.1	Review on fault-tolerant control in multiphase PMSMs	2
1.1.1	Multiple three-phase systems	3
1.1.2	Multiphase single star systems	4
1.2	Review on open-circuit fault diagnosis	5
1.3	Contributions of this work	8
1.3.1	Open-circuit fault mitigation	8
1.3.2	Fault-tolerant control	9
1.3.3	Fault diagnosis	9
1.4	Outline	10
2	Mathematical model of PMSMs	13
2.1	Multiphase PMSM description	14
2.2	Magnetic equivalent circuit (MEC)	16
2.2.1	Magnetic network equations	18
2.2.2	Torque and radial forces	19
2.2.3	Air gap permeances	20
2.3	Electric network	22
2.3.1	Dynamic model	23
2.3.2	Electric coil interconnections and model reduction	24
2.3.3	Multiple open-circuit fault cases	27
2.4	Application of the electric network	28
2.4.1	Quadruple three-phase system (4×3)	28
2.4.2	Single star twelve-phase system (1×12)	32
2.4.3	Single three-phase system (1×3)	34
3	Model calibration and validation	37
3.1	Test stand	37
3.1.1	Voltage source inverter	38
3.1.2	Open-circuit fault emulation	40

Contents

3.2	Model calibration	40
3.3	Model validation	43
4	Current optimization with radial force compensation	47
4.1	Current optimization problem formulation	47
4.2	Current optimization results	49
4.2.1	Cases without radial force compensation	49
4.2.2	Open-circuit fault cases with radial force compensation	51
4.3	Approximation for real-time application	53
4.3.1	Approximation results	57
5	Fault-tolerant control	63
5.1	Fault-tolerant control strategy	64
5.1.1	Current reference signals	64
5.1.2	Feedforward part	65
5.1.3	PI controller	66
5.1.4	Iterative learning control (ILC)	67
5.1.5	Terminal voltage mapping	70
5.1.6	Proportional integral resonant (PIR) controller	71
5.2	Control strategy results	72
5.2.1	Healthy-circuit case	73
5.2.2	Multiple open-circuit post-fault cases	77
5.2.3	Performance comparison of 1×12 and 4×3 configuration	84
6	Open-circuit fault diagnosis	87
6.1	Fault diagnosis method	87
6.2	Fault diagnosis results	89
6.2.1	Immunity to false diagnosis	89
6.2.2	Diagnosis speed of single open-circuit fault without mitigation	90
6.2.3	Multiple open-circuit fault diagnosis and mitigation	92
7	Conclusion and outlook	97
A	Appendix	101
A.1	Resonant controller	101
	Bibliography	103

1

Introduction

Parts of this chapter were published in similar form in the author's previous publications [1–3].

Permanent magnet synchronous machines (PMSM) are known for their high power density, efficiency, and dynamic performance. Thus, they are utilized in various applications ranging from industrial automation over robotics and wind power generation to transport applications, especially the growing sector of more electric airplanes, trains, ships, and vehicles [4–6]. This includes safety-critical applications, such as e.g., steer-by-wire systems in the automotive field [7, 8].

In these safety-critical applications the loss of the entire system due to a fault is intolerable. The possible occurring faults for such systems are classified into mechanical faults, i.e., bearing faults, eccentricity faults, broken rotor bars, and rotor magnet faults [4, 5, 9, 10], and electrical faults, i.e., short-circuit or open-circuit (OC) cases within the involved components [5, 9, 10].

Based on the fault severity and the applications' safety requirements, one of the three main fault-tolerance concepts fail-operational, fault-tolerant, or fail-safe has to be applied [11, 12]. Fail-operational concepts ensure a proper system operation with the same objectives as before a single fault occurrence. Typically, a second redundant system is integrated as backup, which requires space, resources and integration effort. The concept of fault-tolerant systems allows for a degradation of the systems' performance but the system is still available for operation. In fail-safe concepts, the system is transferred into a save state after the fault occurrence, which can include a (controlled) shutdown of the entire system. As this is unacceptable for safety-critical applications and to avoid the extra demands for fail-operational concepts, fault-tolerant strategies are favored as the recent survey literature shows [4–6, 10, 13–15].

1 Introduction

Classical three-phase PMSMs have two electrical degrees of freedom (DOFs), commonly used for torque tracking, loss reduction, or field weakening. In fault cases, these DOFs are reduced, which leads to performance deterioration up to a total failure of the system. The ability for fault-tolerance requires redundancy within the hardware components, which is not given for three-phase PMSMs. Therefore, multiphase PMSMs with n -phases ($n > 3$) are introduced, which can provide the required redundancy due to additional accessible, and therefore controllable, stator windings, increasing the electrical DOFs and preserve the system's integrity [4, 10].

OC faults are common electrical faults in electrical machines causing the disconnection from the supply of one or more phases, thus decreasing the system's available DOFs for post-fault control tasks [10, 16]. OC faults occur in stator windings, line wires, and voltage source inverter (VSI) switches [4, 14, 16]. Additionally, as short-circuit faults within the VSI switches are critical faults, short-circuit protection strategies involve fast fuses, which decouple the short-circuited switch and hence result in an OC fault [4, 16, 17]. An overview of fault-tolerant strategies, especially for power electronic converters, can be found in, e.g., [18]. The fault severity and impact depend on the stator geometry and winding distribution of the multiphase PMSM. In particular, the effects of an OC fault case are performance degradation, significant torque ripple, and vibrations due to unbalanced radial forces occurring in the PMSM [14, 19–21]. These unbalanced radial forces create undesired noise and stress the bearings [22–27]. Since up to 50% - 75% of the mechanical faults are attributed to the bearings [4, 17, 28], the compensation of radial forces in the event of OC faults is crucial to prevent the system from further damage.

1.1 Review on fault-tolerant control in multiphase PMSMs

Fault-tolerant control (FTC) strategies are introduced to mitigate the fault impact in a post-fault situation. Thereby, the detection of a fault is provided by a fault diagnosis method, see Section 1.2. The number of survey papers in the field of multiphase machines [5, 6, 10, 13–15] and, in particular, for multiphase PMSMs [4] has increased over the last decade, demonstrating the importance of suitable solutions for FTC strategies. In post-fault situations, the available DOFs for FTC depend on the winding interconnection of the multiphase machines, where star interconnections are favored [29]. Concentrated, non-overlapping windings (single tooth windings), see, e.g., Fig. 2.1, are suitable for safety-critical applications because the windings do not have physical contact, which impedes fault propagation [30]. The power losses are also lower because of shorter end-windings [31]. The drawbacks are pronounced non-fundamental wave back-electromotive force

1.1 Review on fault-tolerant control in multiphase PMSMs

(BEMF) and cogging torque, which have to be suppressed by the control strategy [8, 32–39]. Higher current harmonics are required to mitigate these drawbacks and must be set by the control strategy.

The goals of the FTC are described by [14] as maximum torque and minimum loss while tracking the desired torque, which are the common goals for three-phase machines but do not exploit the advantages of the higher number of DOFs. FTC strategies are typically divided into deriving suitable reference control values considering the particular OC fault case and adapting the control outputs to the available DOFs. Vector space decomposition (VSD) methods are frequently utilized for both tasks. General VSD methods are proposed in [40] for multiphase machines, including higher harmonic components, and in [41] for concentrated winding machines and star interconnections. However, these methods are devoted to the healthy-circuit (HC) case and are difficult to adapt systematically in multiple OC fault cases.

The literature of FTC strategies for OC faults is reviewed in the following, considering multiple three-phase and multiphase single star systems individually.

1.1.1 Multiple three-phase systems

The first of the two common winding configurations consists of $m > 1$ sets of three-phase systems ($m \times 3$), which are preferred in industrial practice because of the extensive three-phase system control knowledge that can be easily applied to any three-phase system. In the event of a single OC fault, there are two scenarios for FTC:

- a) The most straightforward strategy disconnects the entire faulty three-phase set without control strategy adaptation within the remaining healthy three-phase sets, resulting in maximum torque reduction and large torque ripples, see, e.g., [42, 43] for six phases and [44] for nine phases. Additionally, large radial forces are reported in [45] for a six-phase and in [46] for an eighteen-phase PMSM. In particular, the impact of rotor magnets placement (interior or surface mounted) and winding distribution on the performance is investigated in [45]. The FTC strategies with control strategy adaptation of the remaining healthy three-phase sets range from re-tuning the controller gains for a six-phase PMSM in [47] to minimum loss strategies for nine-phase PMSMs in [48, 49], achieving a lower torque ripple. However, vibration reduction is not reported or achieved in experiments.
- b) The second scenario for FTC control also utilizes the remaining two healthy phases of the faulty three-phase set to exploit the remaining DOFs better. One strategy consists of reconfigured dq-references proposed in [21, 42] for six-phase PMSMs, leading to lower power losses, and in [44, 50] for nine-phase

1 Introduction

PMSMs. In [50], a comparison of an SPMSM (surface-mounted PMSM) and a PMA-SRM (permanent magnet-assisted synchronous reluctance machine) is presented, where the resulting torque vibrations can be acceptably suppressed for the SPMSM but are still high for the PMA-SRM. In [44], higher current harmonics are introduced for a bearingless PMSM to lower the occurring radial forces. A maximum torque per ampere (MTPA) strategy is given in [20] for a six-phase PMSM, which additionally utilizes the second harmonic of dq-currents to achieve a higher maximum torque for constant current magnitudes. A model predictive control strategy is proposed in [51] for a simplified PMSM model, which can reduce the torque ripple in post-fault situations but has no radial force suppression.

The occurring radial vibrations are analyzed in [23] for a twelve-phase PMSM, where a compensation strategy for the magnetomotive force (mmf) is proposed. This analysis is extended for two single OC faults in different three-phase sets [52]. The direct comparison of FTC strategies with and without using the additional two healthy phases within the faulty three-phase set is investigated in [42, 44], resulting in lower power consumption but higher torque vibrations for the first case.

1.1.2 Multiphase single star systems

The second winding configuration employs one n -phase ($n > 3$) system with a single neutral point ($1 \times n$). This configuration always has more available DOFs for the same number of phases than multiple three-phase sets because each neutral point reduces the DOFs and is, therefore, preferred [29]. The FTC control strategies proposed in [21, 53] consider reconfigured dq-currents for five- and six-phase PMSMs, respectively. A method with hysteresis control combined with a minimum copper current reference generator is proposed in [54] for a five-phase PMSM. In [35], an approach based on instantaneous power balance is presented for a six-phase PMSM, which shows a torque ripple as in the HC case, but radial forces are increased under a single OC fault case. As fundamental harmonic strategies are limited for OC faults, the consideration of higher harmonics to suppress the torque ripple is proposed in [55] for a five-phase PMSM.

A different approach is based on proportional resonant control in [39, 56, 57] for five-phase PMSMs. This approach can be used as an equivalence for the dq representation for three-phase systems. A more promising approach consists of repetitive or iterative learning control (ILC) strategies based on torque errors investigated in [58, 59], or current errors in [60] for five-phase PMSMs. In [24, 61], mmf compensation methods are employed via finite element analysis to analyze and reduce the occurring radial forces, but torque vibrations remain.

A comparison between both winding configurations for a single OC fault case is given in [21], in which the higher number of DOFs of the 1×6 configuration results in lower torque ripples but higher copper losses compared to the 2×3 configuration with five active phases.

1.2 Review on open-circuit fault diagnosis

Fault diagnosis methods monitor the actual system state and report the system's malfunctions, which are given as abnormal system behaviors. The main objectives of fault diagnosis are classified into fault detection, fault localization or isolation, and fault identification or discrimination [17, 62, 63]. The first step of fault diagnosis is fault detection, in which system malfunctions are detected. With fault localization, the occurred fault is attributed to a faulty component, which can be within the sensors (voltage, current, encoder, torque transducer), the actuators (VSI), or the plant (PMSM) [4, 5, 9, 10]. The fault type is determined by the fault identification.

A reliable and fast fault diagnosis procedure is crucial to monitor abnormal system behavior and, in the event of a successful fault diagnosis, to trigger the FTC strategy for that particular fault [14]. Recent surveys of the wide variety of fault diagnosis methods can be found in [5, 63, 64], focusing on PMSMs in [4, 9, 16] and drawing particular attention to OC faults in [10].

Fault diagnosis methods are classified into data-based, model-based and signal-based methods, which are reviewed in detail in [4, 62–64]. For data-based methods, extensive historical system data at different operating points is required beforehand and compared against the monitored signals for fault diagnosis [62, 64]. Model-based methods compare the measured output of the system and the model output to determine abnormalities and hence diagnose faults [63]. In [65], an extended Kalman filter is used to estimate the stator resistance values based on the measured current values in a three-phase PMSM. Unphysically high resistance values are utilized for single-switch OC fault detection. A Luenberger observer for a three-phase PMSM is utilized in [66] to estimate the dq-currents. Single-switch OC faults are detected by residual comparison of the absolute normalized estimated and measured currents.

The basic requirements for a real-time capable OC fault diagnosis method of multiphase machines are given in [67]. By additionally considering the nonlinear behavior of the investigated PMSM, they include

- a) robust fault diagnosis independent of the machine's operational point,
- b) fast fault detection within one current fundamental period (c/fp),
- c) independence of the control strategy or the machine parameters,

1 Introduction

- d) utilization of the sensors for the control task, i.e., phase current sensors,
- e) low tuning and computational effort, and
- f) independence of the electrical coil interconnection.

These criteria imply that suitable OC fault diagnosis methods are directed towards time-domain signal-based methods, which are characterized by utilizing only measured signals, their properties, and a priori machine knowledge [10, 63]. Suitable methods of this field are discussed in the following.

In the literature, two indicators for OC fault cases are typically utilized, i.e., the measured phase currents and the phase current control errors motivated by the following facts. First, the measured current signal equals the sensor noise level after a phase OC fault case for the rest of the time. Second, depending on the operational point, the desired current is different from zero, and hence, a larger current error than in the HC case follows.

VSI switch OC faults are detected by averaging the absolute normalized phase currents of a three-phase PMSM in [68] and a three-phase IM in [69]. In the second step, fault identification uses fundamental wave assumptions and multiple thresholds. The authors of [68] proposed a similar approach in [70] utilizing the current phase errors. Again, averaging, normalization, fundamental wave assumptions, and multiple thresholds are employed. A phase OC fault, given by a sequence of two switch OC faults within the same VSI leg, is experimentally diagnosed.

As the OC post-fault operation in three-phase machines is difficult, research has recently been oriented toward suitable fault diagnosis methods for multiphase machines. A five-phase PMSM is investigated in [71], where OC faults are detected based on the absolute, normalized values of auxiliary variables, given by the currents processed by a quadrature-signal generator. Although this method avoids averaging, a robust fault identification threshold selection seems complicated. A fault diagnosis method suitable for multiple three-phase systems is presented in [72] for a six-phase induction machine (IM), where the OC fault detection variables are given by the averaged current values and the average of the absolute current values assuming sinusoidal currents. By comparing these detection variables with predefined theoretical values derived by a VSD, phase OC faults are experimentally diagnosed by a sequential double switch OC fault in the same VSI leg within 35 % and 60 % of the cfp. VSD methods are investigated in [73] for a five-phase and in [67] for a six-phase IM, where both authors propose a faster fault detection time by considering the averaging period as a tuning parameter with 40 % and 66 % of the cfp, respectively. The fault detection is based on averaging the normalized currents within the stator frame [73] or the rotor frame [67], assuming a sinusoidal current waveform. Both VSD approaches include a hysteresis band for noise rejection, a comparison with a threshold value for fault identification, and experiments for single and simultaneous double OC faults. The single OC faults

are identified within 15 % of the cfp in [73] and 18 % of the cfp in [67]. Additionally, the VSD method in [67] is compared with a similar method as in [68] but expanded for multiphase machines. Single and double OC faults are identified within 66 % of the cfp in the experiment.

In [74], OC faults are diagnosed within a bi-harmonic five-phase PMSM. Although the PMSM exhibits higher harmonics, the fault diagnosis method is based on VSD in the stationary frame, considering only the fundamental wave. The averaged and normalized current error values constitute the detection variables. The fault identification includes several diagnosis variables that require carefully selected thresholds to account for the nonlinear PMSM behavior. These are derived based on simulation results, which depend on the operational point considered. A single-phase OC fault is diagnosed experimentally within 32 % of the cfp.

Higher current harmonics are considered in [75] for a five-phase PMSM. After a VSD transformation of the currents into a stationary frame with the fundamental and third harmonic components, the OC fault detection variables are calculated by the absolute averaged first harmonic components and the averaged third harmonic components. The fault identification is based on several thresholds and counters. Single- and double-phase OC faults are diagnosed within 70 % and 83.3 % of the cfp. The OC fault diagnosis method proposed in [76] can consider several harmonic current components within symmetrical multiphase star interconnected drives. The fault detection is derived from two groups of phase currents that are further filtered and averaged. The higher current harmonics are considered in advance by an optimization problem to determine the worst case, simplifying the threshold selection for fault identification. A sequential phase OC fault up to triple faults is investigated within a nine-phase IM, where the fault identification requires 85.9 % of the cfp.

In [44], both fault indicators (currents and current errors) are combined for an OC fault diagnosis in a nine-phase bearingless PMSM. An OC fault is detected and identified based on thresholds for the current sensor noise and errors. A fault is diagnosed when both fault indicators exceed their thresholds over a time that is not closely specified. Because of its simple structure, this method seems suitable for fault diagnosis under higher current harmonics. Within 120 % of the cfp, a double-phase OC fault is experimentally diagnosed. The diagnosis time for a triple-phase OC fault is not reported.

1 Introduction

1.3 Contributions of this work

This work aims to provide a fault-tolerant solution for multiphase PMSMs in case of multiple OC faults, which mitigates the fault impacts not only for the primary control tasks of torque tracking error reduction and power loss minimization but systematically exploits the available DOFs for additional control goals, such as radial force reduction. For this task, a fault diagnosis method and FTC strategy are developed that consider the nonlinear behavior of the investigated single tooth winding PMSM. The 12 individually controllable stator coils enable the investigation of different electric coil interconnections. Two star configurations are investigated: a quadruple three-phase PMSM with four separate neutral points (4×3 configuration) to provide a multiphase configuration from the well-studied three-phase systems and a twelve-phase PMSM with a single neutral point (1×12 configuration), as this configuration provides the highest DOFs for 12 coils. The direct comparison of the two configurations while maintaining the identical stator and rotor setup is one contribution of this work to evaluate the performance of additional DOFs in multiple OC fault cases. Therefore, the overall concept for fault diagnosis and the FTC strategy is tailored so that both configurations can be considered without significant adjustments.

1.3.1 Open-circuit fault mitigation

The literature review in Section 1.1 shows different approaches for OC fault mitigation, mainly focusing on maintaining the pre-fault control goals in post-fault situations. However, the reviewed literature does not state systematic exploitation of the additional DOFs in multiphase drives for additional control goals in post-fault situations. The contribution of this work fills this gap by proposing a radial force compensation strategy in OC post-fault situations to mitigate the undesired vibration and noise effects of occurring radial forces. For this purpose, the reference currents for control are first derived from the solution of the model-based optimization problem, minimizing the classical control goals such as torque tracking error and power losses. In addition, the radial force compensation is introduced as a third optimization goal for the OC fault mitigation thanks to the additional DOFs of the multiphase PMSM. Thereby, the nonlinear effects of the PMSM have to be compensated, which requires an accurate model featuring nonlinear effects for the HC case and additional radial force calculation for arbitrary multiple OC fault cases. A nonlinear magnetic equivalent circuit (MEC) model is suitable for this task, and the framework proposed in [36] and [77] is extended in this work to describe the radial forces acting on the rotor in unbalanced OC fault cases. An electric network model is developed, considering different stator coil interconnec-

tions in a star configuration and arbitrary multiple OC fault cases. The included model reduction step ensures a model of minimum state, where the reduced currents correspond to the available DOFs and are still physically meaningful. The real-time capability is ensured by approximating the optimized currents, which include higher harmonic components in the current patterns. With the introduced radial force compensation, a significant radial force reduction is achievable to reduce noise and vibrations, which prevents the system from further damage.

1.3.2 Fault-tolerant control

The FTC strategies reviewed in Section 1.1 are tailored to a constant coil topology and are adapted for each OC fault case individually. Compared to the existing literature, this work fills the gap for a systematic approach for a flexible FTC strategy considering only the available DOFs for control. The developed high-performance FTC strategy includes a model-based feedforward term and a proportional integral (PI) feedback controller. The limited PI controller bandwidth requires an additional solution suitable for higher rotational speeds, where the current tracking errors are large. Therefore, an ILC concept is introduced to further reduce the current errors, which are mainly introduced due to the unknown nonlinear VSI behavior. Advantageously, the FTC strategy controls only the available DOFs, which differ for the two investigated electrical coil interconnections and are further reduced in OC fault cases. With this developed FTC strategy, a systematic comparison and experimental evaluation of n-phase and multiple three-phase systems under multiple OC faults at various operation scenarios, including high speed is presented.

1.3.3 Fault diagnosis

Based on the discussed literature in Section 1.2, a gap exists for a fault diagnosis method meeting all criteria a) - f). Thus, in this work, a real-time fault diagnosis method is developed for multiple OC fault cases in multiphase PMSMs with higher current harmonics. It combines both fault identifiers (phase currents and phase current errors) separately for each phase. The method is independent of prior system knowledge, e.g., VSD and electrical interconnection. In addition, the fault detection and identification processes are combined, and only one tuning parameter is required to achieve immunity to false diagnosis under load variations. Furthermore, the proposed method can diagnose multiple OC faults and sequentially arising OC faults below 41 % of a cfp for the 4×3 and the 1×12 configuration.

1.4 Outline

This work is structured as follows:

In Chapter 2, the derivation of the nonlinear mathematical model is presented. The magnetic part of the model is covered by a nonlinear MEC model that includes the nonlinear effects of the investigated PMSM and provides the radial force description based on an enhanced air gap permeance modeling. The different electric coil configurations and multiple OC fault cases are described in the derived electric part. Finally, the overall mathematical model is applied to a quadruple three-phase (4×3 configuration), a twelve-phase (1×12 configuration), and a three-phase PMSM (1×3 configuration), each with isolated neutral points.

Chapter 3 is devoted to the model calibration and validation of the derived model. First, the utilized test stand for all measurements is explained. This includes the compensation of the used multiphase VSI with its nonlinear behavior. Then, the model calibration procedure is given to calibrate the air gap permeances and the stator leakage permeances. Finally, the calibrated model is validated in static and dynamic conditions, demonstrating high model accuracy.

This calibrated and validated model is the basis for the current optimization with radial force compensation, presented in Chapter 4. The presented approach allows for the individual minimization of the commonly utilized control goals, such as torque tracking error and power losses, and the radial forces occurring in unbalanced OC fault cases by the introduced weighting factors. Their influence on the optimization results are discussed. To ensure real-time capability, these optimized currents are approximated by Fourier series, and the coefficients are stored efficiently in lookup tables. The reference current patterns include higher harmonic components to achieve a high performance of the PMSM.

The FTC strategy is derived in Chapter 5. The control challenges arise from the higher harmonic current components within the reference currents and the nonlinear VSI behavior. The FTC strategy consists of a nonlinear feedforward part, a PI feedback part, and an ILC part. Advantageously, only the available DOFs are controlled, adding flexibility to compare different electrical coil interconnections under multiple OC faults using the same FTC strategy. A PI resonant (PIR) controller as a state-of-the-art control strategy is presented for comparison. Experiments performed on the test stand compare the proposed FTC strategy and the PIR control strategy in the HC case for the 4×3 and the 1×12 configuration. Multiple OC fault cases are evaluated in detail by measurements with the FTC strategy. The performances with and without radial force reduction are analyzed in detail for single, double, and triple OC fault cases. Finally, a comparison of the performances for both configurations is given.

A fault diagnosis method is presented in Chapter 6. Only the measured phase current signals are utilized to reduce the methods' complexity and ensure real-time capability. The derived fault diagnosis method consists of a combined fault detection and isolation procedure, and requires only one tuning parameter to achieve immunity to false diagnosis. The effectiveness of this method is verified under different operation scenarios by measurements on the test stand. Sequential and simultaneous triple OC faults are investigated at different speeds for both the 4×3 and the 1×12 configuration.

Finally, this work is summarized in Chapter 7, and an outlook on future research topics is given.

2

Mathematical model of PMSMs

Parts of this chapter were published in similar form in the author's previous publications [1, 2].

This chapter presents a systematic derivation of the dynamic mathematical model of the considered permanent magnet synchronous machine (PMSM). It aims to derive an accurate and fast mathematical model that is the basis for the current optimization method with radial force compensation developed in Chapter 4 and the fault-tolerant control (FTC) strategy for multiple open-circuit (OC) faults presented in Chapter 5. Thereby, the model must take into account nonlinear effects, i.e., cogging torque, magnetic saturation, and non-fundamental wave behavior, provide a description for radial forces and support of a flexible structure to systematically incorporate different electric coil interconnections for the healthy-circuit (HC) case and multiple OC fault cases.

In the literature, there are three main modeling approaches for PMSMs. For highly accurate mathematical models of PMSMs, finite-element method (FEM) models are suitable. However, they require high computational power and are therefore not real-time capable. Magnetic equivalent circuit (MEC) models utilize flux tube approximations, which only allow for a magnetic flux direction perpendicular to the cross-section area, to reduce the computational effort while covering nonlinear magnetic effects [78]. Depending on the accuracy level, MEC models are utilized in real-time applications, cf. [79]. Popular fundamental wave models such as dq0-models provided by the Blondel-Park transformation are widely utilized for field-oriented control (FOC) because of their constant reference currents in the rotating reference frame and low computational effort, cf. [80]. However, a systematic consideration of nonlinear effects is difficult.

The dynamic mathematical model in this work is based on an MEC network, as this approach meets the requirements of describing the magnetic nonlinear effects,

2 Mathematical model of PMSMs

including radial forces, separately from the considered electrical network. The fundamentals of MEC modeling are given in, e.g., [78, 81–83]. The detailed magnetic description of the MEC model includes the nonlinear effects, while different electrical interconnections are considered only within the electric network. This concept is advantageous for this work because the magnetic part of the motor is identical, while different coil interconnections and multiple OC fault cases affect only the electrical network.

The dynamic mathematical model presented in this work follows the fundamental steps of the framework proposed in [77] and utilizes an enhanced magnetic network description of [36], as the PMSM in [36] is magnetically identical to the considered PMSM in this work. It is shown in [36] that the PMSM reveals a highly nonlinear behavior due to cogging torque and magnetic saturation effects, which are accurately described by the nonlinear MEC model. An enhanced air gap shape model extends this magnetic setup to describe the radial forces acting on the rotor, which becomes relevant in OC fault cases. An electric network approach is developed that systematically incorporates different electrical interconnections and their changes due to multiple OC fault cases. This approach systematically reduces the redundancy within the obtained dynamical model to a minimum number of states without losing the physical meaning of the states due to the electric network consideration.

This chapter is organized as follows: The setup of the considered multiphase PMSM is described in Section 2.1. The MEC network modeling in Section 2.2 is composed of the description of the magnetic equations systematically derived using graph theory in Section 2.2.1. In Section 2.3, the electric network is presented, including the systematic approach for different electric coil interconnections and multiple OC faults. The application of this electric network for the investigated electrical coil interconnections is given in Section 2.4.

2.1 Multiphase PMSM description

The investigated PMSM has 12 single tooth windings (concentrated, non-overlapping stator coil windings) and 8 interior NdFeB-permanent magnets, which gives a number of pole pairs $n_p = 4$, see Fig. 2.1. The stator and rotor are constructed of iron sheets. The considered PMSM was designed for an automotive power steering application, where self-blocking the steering shaft at standstill per construction is required [36]. This was achieved by the design of rotor iron combined with the permanent magnet placement, see Fig. 2.1, which leads to high cogging torques. While operating the PMSM with fundamental wave control strategies, these cog-

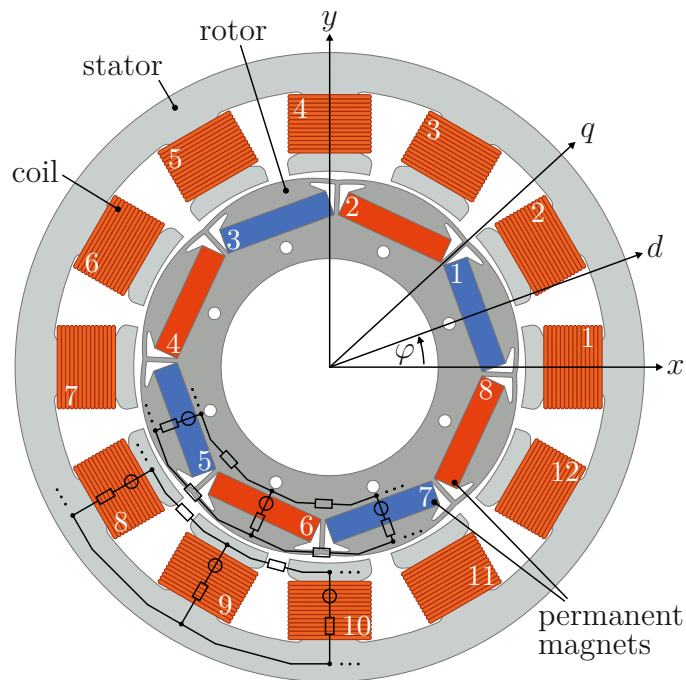


Figure 2.1: Sketch of the considered PMSM with the mechanical stator-fixed frame (xy), the rotor-fixed frame (dq), and the magnetic network for stator and rotor parts.

ging torques cannot be compensated and result in undesired torque vibrations, cf., [8, 32–39].

The initial electrical interconnection of this PMSM consisted of four stator coils connected in parallel to form a three-phase delta configuration, see [36], resulting in two degrees of freedom (DOFs) without offering FTC capabilities. To exploit the potential of this PMSM as a multiphase PMSM, in this work all stator coils are lead out individually. This transforms the PMSM into a multiphase PMSM with 12 individually controllable stator coils. In particular, two electrical interconnections are considered

- 4×3 : Four separate three-phase systems in star (wye) configuration with four separated and isolated neutral points, see Section 2.4.1.
- 1×12 : One twelve-phase system in star configuration with all 12 coils sharing a common isolated neutral point, see Section 2.4.2.

This choice considers the two main multiphase PMSMs' electrical interconnections concerning an m three-phase system as well as an n -phase system, each with the highest DOFs for the investigated PMSM, cf. Section 1.1.

2 Mathematical model of PMSMs

Additionally, the classical three-phase system (1×3) configuration is described in Section 2.4.3, which is the used electrical configuration for the model calibration procedure, see Section 3.2.

The investigated PMSM's magnetic behavior is described in the following sections.

2.2 Magnetic equivalent circuit (MEC)

The magnetic behavior of the PMSM is approximated by a nonlinear magnetic equivalent circuit (MEC) model. The derivation of the magnetic network follows the proposed framework in [77]. For completeness, the basic relationships and derivations are given in this section.

The magnetic network is represented by a MEC given in Fig. 2.2. The elements of the MEC consist of magnetomotive force (mmf) sources and permeances, which are used to describe the magnetic properties. The magnetic circuit relation is given

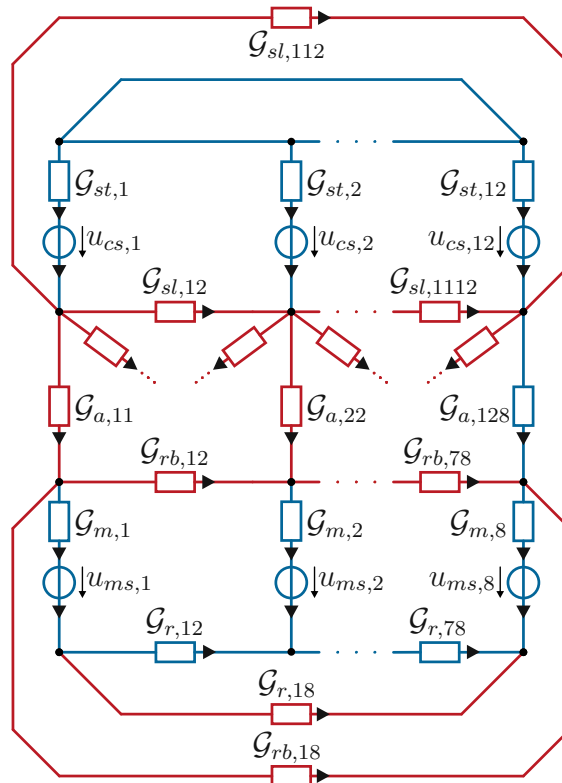


Figure 2.2: Schematic of the MEC network with the tree and co-tree indicated in blue and red, respectively.

2.2 Magnetic equivalent circuit (MEC)

by Hopkinson's law [81]

$$\phi = \mathcal{G}u = \frac{1}{\mathcal{R}}u, \quad (2.1)$$

with the magnetic flux ϕ , the mmf u and the reluctance \mathcal{R} as reciprocal of the permeance \mathcal{G} . Arrows indicate the magnetic flux direction in Fig. 2.2 and are given by the notation of the double number subscripts for elements between coils or permanent magnets. In particular, the mmf sources are given by the mmf sources of the stator coils $\mathbf{u}_{cs} = [u_{cs,1}, \dots, u_{cs,12}]$ and the mmf sources of the rotor permanent magnets $\mathbf{u}_{ms} = [u_{ms,1}, \dots, u_{ms,8}]$. The magnetic properties are covered within the description of the permeance

$$\mathcal{G} = \mu_0 \mu_r (|H|) \frac{\mathcal{A}}{\ell}. \quad (2.2)$$

A constant geometry of cuboid-shaped flux tubes is assumed, expressed by the cross-section area \mathcal{A} and the effective length ℓ of the flux tube. The isotropic magnetic material behavior is given by the permeability of vacuum $\mu_0 = 4\pi \text{Vs A}^{-1} \text{m}^{-1}$ and the nonlinear relative permeability $\mu_r (|H|)$ in dependency of the magnetic field strength $H = u/\ell$. Within (2.2), the constitutive relation $B = \mu_0 \mu_r (|H|) H$ between the magnetic flux density B and the magnetic field strength is applied. The permeances within the magnetic network consist of the magnetically nonlinear iron permeances of the stator teeth $\mathcal{G}_{st} (\mu_r (|\mathbf{u}_{st}|/\ell_{st}))$, the rotor yokes $\mathcal{G}_r (\mu_r (|\mathbf{u}_r|/\ell_r))$, the rotor bars $\mathcal{G}_{rb} (\mu_r (|\mathbf{u}_{rb}|/\ell_{rb}))$, the constant permanent magnets permeances $\mathcal{G}_m (\mu_r = \text{const.})$, and the magnetically linear leakage permeances $\mathcal{G}_{sl} (\mu_r = 1)$ between two adjacent stator tooth in the air. Thereby, $\mathbf{u}_{st} = [u_{st,1}, \dots, u_{st,12}]^T$, $\mathbf{u}_r = [u_{r,12}, \dots, u_{r,78}, u_{r,18}]^T$, and $\mathbf{u}_{rb} = [u_{rb,12}, \dots, u_{rb,78}, u_{rb,18}]^T$ indicate the mmfs of the stator teeth, the rotor yokes and the rotor bars, respectively. The last permeances are magnetically linear but position-dependent air gap permeances $\mathcal{G}_a (\varphi, \delta_x, \delta_y)$ linking the fluxes between stator and rotor in the air gap, with the rotor position φ and the (virtual) displacements δ_x and δ_y in x - and y -direction respectively, cf. Fig. 2.1. Due to their strong relation to torque and forces, see Section 2.2.2, the derivation of the air gap permeances is covered in Section 2.2.3. Note that the stator yoke permeances are large in comparison to the stator teeth permeances and hence are neglected, which is an advantage in reduced variables in contrast to the previous modeling approach on this PMSM presented in [36]. The parameter values of the permeances \mathcal{G}_{st} , \mathcal{G}_{sl} , \mathcal{G}_m , \mathcal{G}_r , and \mathcal{G}_{rb} are directly obtained by flux tube approximations of the considered PMSM's geometry and material properties [78]. Thereby, a rotational symmetric geometry is utilized to reduce the number of different parameters.

2 Mathematical model of PMSMs

2.2.1 Magnetic network equations

The network equations can be systematically derived by applying graph theory, see [84]. Therefore, the network is divided into tree (blue) and co-tree (red) elements of the directed graph in Fig. 2.2.

The tree, given by a graph without a circuit, comprises the elements of all mmf sources, i.e. the stator coil mmf sources \mathbf{u}_{cs} and the rotor permanent magnet mmf sources \mathbf{u}_{ms} . The allocation of the remaining components, i.e. the permeances, is arbitrary. In this work, the tree mmfs are given by

$$\mathbf{u}_{tg} = \left[\mathbf{u}_{st}^T \quad \mathbf{u}_m^T \quad \mathbf{u}_r^T \quad u_{a,128} \right]^T \quad (2.3)$$

with the mmfs of the stator teeth \mathbf{u}_{st} , the rotor permanent magnets $\mathbf{u}_m = [u_{m,1}, \dots, u_{m,8}]^T$, the rotor yoke parts \mathbf{u}_r , and the air gap permeance $u_{a,128}$ between the 12th coil and the 8th permanent magnet. The co-tree mmfs

$$\mathbf{u}_c = \left[u_{a,11} \quad \dots \quad u_{a,127} \quad \mathbf{u}_{sl}^T \quad \mathbf{u}_{rb}^T \quad u_{r,18} \right]^T \quad (2.4)$$

are then composed of the mmfs of the air gap permeances, the stator leakages $\mathbf{u}_{sl} = [u_{sl,12}, u_{sl,23}, \dots, u_{sl,1112}, u_{sl,112}]^T$, the rotor bars \mathbf{u}_{rb} , and the last rotor yoke part $u_{r,18}$. This network allocation is similar to [36, 77]. The tree and co-tree elements are linked by the incidence matrix \mathbf{D} in the form

$$\phi_t = \mathbf{D} \phi_c, \quad (2.5)$$

for the tree fluxes ϕ_t and co-tree fluxes ϕ_c . The entries within the incidence matrix are either -1 , 0 , or 1 and correspond to the flux direction. With Tellegen's theorem [81]

$$\phi_t^T \mathbf{u}_t + \phi_c^T \mathbf{u}_c = \mathbf{0}, \quad (2.6)$$

the relation between the mmf of the tree \mathbf{u}_t and co-tree \mathbf{u}_c is given by inserting (2.5) into (2.6) resulting in

$$\mathbf{u}_c = -\mathbf{D}^T \mathbf{u}_t \quad (2.7)$$

By applying Hopkinson's law (2.1) to the co-tree fluxes combined with (2.7) and inserting the result into (2.5) yields

$$\begin{bmatrix} \phi_{cs} \\ \phi_{ms} \\ \phi_{tg} \end{bmatrix} = - \begin{bmatrix} \mathbf{D}_c \\ \mathbf{D}_m \\ \mathbf{D}_g \end{bmatrix} \mathcal{G}_c \begin{bmatrix} \mathbf{D}_c^T & \mathbf{D}_m^T & \mathbf{D}_g^T \end{bmatrix} \begin{bmatrix} \mathbf{u}_{cs} \\ \mathbf{u}_{ms} \\ \mathbf{u}_{tg} \end{bmatrix}. \quad (2.8)$$

Therein, the tree elements are separated into the tree parts for stator coils ϕ_{cs} , \mathbf{D}_c , \mathbf{u}_{cs} , permanent magnets ϕ_{ms} , \mathbf{D}_m , \mathbf{u}_{ms} , and tree permeances ϕ_{tg} , \mathbf{D}_g , \mathbf{u}_{tg} .

2.2 Magnetic equivalent circuit (MEC)

The set of nonlinear algebraic equations

$$\begin{bmatrix} \mathbf{D}_c \mathcal{G}_c \mathbf{D}_c^T N_c & \mathbf{0} & \mathbf{D}_c \mathcal{G}_c \mathbf{D}_g^T \\ \mathbf{D}_m \mathcal{G}_c \mathbf{D}_c^T N_c & \mathbf{I} & \mathbf{D}_m \mathcal{G}_c \mathbf{D}_g^T \\ \mathbf{D}_g \mathcal{G}_c \mathbf{D}_c^T N_c & \mathbf{0} & \mathcal{G}_t + \mathbf{D}_g \mathcal{G}_c \mathbf{D}_g^T \end{bmatrix} \begin{bmatrix} \mathbf{i}_c \\ \phi_{ms} \\ \mathbf{u}_{tg} \end{bmatrix} = \begin{bmatrix} \frac{1}{N_c} \boldsymbol{\psi}_c \\ \mathbf{0} \\ \mathbf{0} \end{bmatrix} - \begin{bmatrix} \mathbf{D}_c \\ \mathbf{D}_m \\ \mathbf{D}_g \end{bmatrix} \mathcal{G}_c \mathbf{D}_m^T \mathbf{u}_{ms} \quad (2.9)$$

is derived by the rearranged equation (2.8) after several calculation steps, including the expression of the tree permeance fluxes $\phi_{tg} = \mathcal{G}_t \mathbf{u}_{tg}$ utilizing Hopkinson's law (2.1), the introduction of the stator coil flux linkages $\boldsymbol{\psi}_c = -N_c \phi_{cs}$, and the stator coils mmf sources $\mathbf{u}_{cs} = N_c \mathbf{i}_c$ expressed by the stator coil currents \mathbf{i}_c . Thereby, \mathbf{I} is the identity matrix of suitable size and the number of coil winding turns N_c is equal for all stator coils. With the constant mmf sources of the permanent magnets, the flux linkages are chosen as state variables to calculate the coil currents, the permanent magnet fluxes, and the mmf of the tree permeances. As the permanent magnet fluxes are irrelevant to the subsequent modeling of the PMSM and are decoupled in the equation (2.9), they can be neglected to reduce the system's dimensions. The relevant part of the nonlinear magnetic equivalent circuit can now be described by the set of nonlinear algebraic equations

$$\begin{bmatrix} \bar{\mathbf{D}}_c \mathcal{G}_c \bar{\mathbf{D}}_c^T & \bar{\mathbf{D}}_c \mathcal{G}_c \mathbf{D}_g^T \\ \mathbf{D}_g \mathcal{G}_c \bar{\mathbf{D}}_c^T & \mathcal{G}_t + \mathbf{D}_g \mathcal{G}_c \mathbf{D}_g^T \end{bmatrix} \begin{bmatrix} \mathbf{i}_c \\ \mathbf{u}_{tg} \end{bmatrix} = \begin{bmatrix} \boldsymbol{\psi}_c \\ \mathbf{0} \end{bmatrix} - \begin{bmatrix} \bar{\mathbf{D}}_c \\ \mathbf{D}_g \end{bmatrix} \mathcal{G}_c \mathbf{D}_m^T \mathbf{u}_{ms} , \quad (2.10)$$

with the diagonal matrices of the tree and co-tree permeances \mathcal{G}_t and \mathcal{G}_c , cf. [36, 77]. The incidence matrix $\bar{\mathbf{D}}_c = N_c \mathbf{D}_c$ is scaled by the number of coil windings.

The set of nonlinear equations (2.10) consists of $\dim(\mathbf{i}_c) + \dim(\mathbf{u}_{tg}) = 12 + 28 = 40$ algebraic variables. However, (2.10) has a redundant equation since the sum of flux linkages equals zero due to Gauss's law for magnetism. Following the framework of [77], this redundancy is eliminated as part of the electrical network consideration in Section 2.3.

2.2.2 Torque and radial forces

The electromagnetic torque τ is an essential quantity for electric drives. The torque can be directly obtained by applying the co-energy principle, which states that a (generalized) force is calculated by the partial derivative of the co-energy concerning the (generalized) displacement, see, e.g., [28, 78]. This yields

$$\tau = \frac{1}{2} \left(\mathbf{u}_{tg}^T \frac{\partial \mathcal{G}_t}{\partial \varphi} \mathbf{u}_{tg} + \mathbf{u}_c^T \frac{\partial \mathcal{G}_c}{\partial \varphi} \mathbf{u}_c \right) . \quad (2.11)$$

It is worth mentioning that only the air gap permeances are nonlinear functions of the rotor position φ but magnetically linear, which simplifies the torque calculation.

2 Mathematical model of PMSMs

To describe the radial force acting on the rotor, this approach is transferred analogously to derive the expressions for the forces. The forces F_x and F_y acting in x - and y -direction are determined analogously to (2.11)

$$F_x = \frac{1}{2} \left(\mathbf{u}_{tg}^T \frac{\partial \mathcal{G}_t}{\partial \delta_x} \mathbf{u}_{tg} + \mathbf{u}_c^T \frac{\partial \mathcal{G}_c}{\partial \delta_x} \mathbf{u}_c \right), \quad (2.12a)$$

$$F_y = \frac{1}{2} \left(\mathbf{u}_{tg}^T \frac{\partial \mathcal{G}_t}{\partial \delta_y} \mathbf{u}_{tg} + \mathbf{u}_c^T \frac{\partial \mathcal{G}_c}{\partial \delta_y} \mathbf{u}_c \right). \quad (2.12b)$$

Again, only the air gap permeances are nonlinear functions of the (virtual) displacements δ_x and δ_y of the rotor in x - and y -direction, cf. Fig. 2.1. The radial force is then given by

$$F_r = \sqrt{F_x^2 + F_y^2}. \quad (2.13)$$

It is evident from (2.11) and (2.12), that the torque and force descriptions heavily depend on the air gap permeance modeling and more precisely on their derivative with respect to the (rotor) positions, which is described in the next section.

2.2.3 Air gap permeances

An accurate model for the air gap permeances is essential for the model accuracy since the torque and forces are directly related to the partial derivative of \mathcal{G}_a with respect to φ , δ_x and δ_y , see (2.11) and (2.12) and cf. [36, 77, 78]. Due to the changing geometry of the rotor circumference over the rotor position, cf. Fig. 2.1, an accurate calculation of the air gap permeances $\mathcal{G}_a(\varphi, \delta_x, \delta_y)$ as a function of φ solely based on the geometry is not possible. However, symmetry in the rotational direction is given due to the equally distributed stator tooth and rotor magnets. In the literature, several approaches exist to describe the shape of the air gap permeances by functions. Due to the importance of the air gap permeance derivatives with respect to the positions, the air gap shape function has to be at least a twice continuously differentiable function. E.g. cosine functions are utilized in [36, 78], a Fourier series approximation is applied in [77] or two Gaussian functions are proposed in [28]. The parameters of these shape functions are then used to calibrate the model by measurements, see Chapter 3 and, e.g., [77]. While these shape functions are meaningful for three-phase motors, because of their periodicity, they are not well suited for multiphase motors. In particular for multiphase motors, it is required to truncate the cosine and Fourier series in order to represent the local coupling of the air gap permeances of the permanent magnet m with the coil tooth j , i.e. the air gap permeance $\mathcal{G}_{a,jm}$ is zero if the permanent magnet m is not placed near the coil tooth j . This is inherently covered by Gaussian functions.

2.2 Magnetic equivalent circuit (MEC)

The approach, including the sum of several Gaussian functions, enables the additional placement of symmetrically Gaussian functions to cover local shape effects, which are required for accurate torque and force descriptions. Furthermore, this symmetry feature reduces the calibration parameters. For this reason, a sum of Gaussian functions is utilized to cover the dependence of $\mathcal{G}_{a,jm}$ on the rotor angle φ

$$\mathcal{G}_{a,jm}^\varphi = A_0 e^{-\frac{\tilde{\varphi}^2}{2\sigma_0^2}} + \sum_{k=1}^{n_g} A_k \left(e^{-\frac{(\Delta\tilde{\varphi}_k^-)^2}{2\sigma_k^2}} + e^{-\frac{(\Delta\tilde{\varphi}_k^+)^2}{2\sigma_k^2}} \right), \quad (2.14)$$

with the abbreviations $\Delta\tilde{\varphi}_k^- = \tilde{\varphi} - \Delta\varphi_k$ and $\Delta\tilde{\varphi}_k^+ = \tilde{\varphi} + \Delta\varphi_k$. Therein, the relative rotation of the coil j to the permanent magnet m is modeled by $\tilde{\varphi} = \varphi - \varphi_{s,j} + \varphi_{r,m}$, with stator coil angular shift $\varphi_{s,j} = 2\pi(j-1)/n_c$, $j = 1, \dots, n_c$ and the rotor magnet angular shift $\varphi_{r,m} = 2\pi(m-1)/n_m$, $m = 1, \dots, n_m$ ($n_c = 12$ and $n_m = 8$ for the considered PMSM). The amplitudes A_k , the widths (variances) σ_k and the shifts $\Delta\varphi_k$ of $\mathcal{G}_{a,jm}^\varphi$ are used as DOFs in the model calibration. Please note that the symmetry of $\mathcal{G}_{a,jm}^\varphi$ with respect to $\tilde{\varphi}$ is guaranteed by the symmetrical placement of the n_g Gaussian functions.

To represent the dependency of the air gap permeance on the virtual displacements δ_x and δ_y (see Fig. 2.1), the overall air gap permeance $\mathcal{G}_{a,jm}$ is formulated as

$$\mathcal{G}_{a,jm}(\varphi, \delta_x, \delta_y) = \mathcal{G}_{a,jm}^\varphi(\varphi) h_{F,j}(\delta_x, \delta_y) \quad (2.15)$$

with

$$h_{F,j}(\delta_x, \delta_y) = \frac{1}{1 - \frac{\delta_x}{l_g} \cos(\varphi_{s,j}) - \frac{\delta_y}{l_g} \sin(\varphi_{s,j})}, \quad (2.16)$$

where l_g is the nominal length of the air gap. The term (2.16) is introduced for the radial force calculation, see, e.g., [78, 85]. The required derivatives of the air gap permeances (2.15) with respect to the (rotor) positions for the torque and force expression, see (2.11) and (2.12), are given by

$$\frac{\partial \mathcal{G}_{a,jm}}{\partial \varphi} = \frac{\partial \mathcal{G}_{a,jm}^\varphi}{\partial \varphi} h_{F,j} \quad (2.17a)$$

$$\frac{\partial \mathcal{G}_{a,jm}}{\partial \delta_x} = \mathcal{G}_{a,jm}^\varphi \frac{h_{F,j}^2}{l_g} \cos(\varphi_{s,j}) \quad (2.17b)$$

$$\frac{\partial \mathcal{G}_{a,jm}}{\partial \delta_y} = \mathcal{G}_{a,jm}^\varphi \frac{h_{F,j}^2}{l_g} \sin(\varphi_{s,j}) \quad (2.17c)$$

with

$$\frac{\partial \mathcal{G}_{a,jm}^\varphi}{\partial \varphi} = -\frac{\tilde{\varphi}}{\sigma_0^2} A_0 e^{-\frac{\tilde{\varphi}^2}{2\sigma_0^2}} - \sum_{k=1}^{n_g} \frac{A_k}{\sigma_k^2} \left(\Delta\tilde{\varphi}_k^- e^{-\frac{(\Delta\tilde{\varphi}_k^-)^2}{2\sigma_k^2}} + \Delta\tilde{\varphi}_k^+ e^{-\frac{(\Delta\tilde{\varphi}_k^+)^2}{2\sigma_k^2}} \right). \quad (2.18)$$

2 Mathematical model of PMSMs

This work focuses on torque and radial force description for concentric rotor placement, i.e., $\delta_x = \delta_y = 0$ is assumed.

Eccentricity faults

Eccentricity faults are caused by a misalignment of the rotor and stator axis to each other. Then, the air gap length is asymmetrical in the circumferential direction, causing asymmetric radial forces, cf. [17, 78, 86]. This effect is called an unbalanced magnetic pull (UMP), cf. [16, 17]. The consequences are unwanted vibration causing noise and bearing wear [27]. The main eccentricity faults are static, dynamic, and mixed eccentricity faults [17, 86]. Although no eccentricity faults are considered for the investigated PMSM in this work, the air gap permeance description can also describe these faults. The following explains the modeling for equal eccentricity fault cases on both motor sides.

Static eccentricity faults describe constant displacements of the rotor center point (RCP) related to the stator center point (SCP), see Fig. 2.3a. They are represented by the constant values $\delta_x = \Delta_x$ and $\delta_y = \Delta_y$ in the model approach. For dynamic eccentricity faults, where the RCP is dynamically rotating around the stator center point, the radial displacements are functions of the rotor position $\delta_x(\varphi)$ and $\delta_y(\varphi)$, see Fig. 2.3b. Both eccentricity faults combined are referred to as mixed eccentricity faults. They can be expressed by $\delta_x(\varphi) = \Delta_x + \Delta_r \cos(\bar{\varphi})$ and $\delta_y(\varphi) = \Delta_y + \Delta_r \sin(\bar{\varphi})$, see Fig. 2.3c, with a suitable expression for $\bar{\varphi}(\varphi)$ as a function of the rotor position. In this case, the term $h_{F,j}$ in (2.16) is additionally rotor position dependent, and hence the derivative of the air gap permeance with respect to the rotor position reads as

$$\frac{\partial \mathcal{G}_{a,jm}}{\partial \varphi} = \frac{\partial \mathcal{G}_{a,jm}^\varphi}{\partial \varphi} h_{F,j}(\varphi) + \mathcal{G}_{a,jm}^\varphi \frac{\partial h_{F,j}(\varphi)}{\partial \varphi} \quad (2.19)$$

with

$$\frac{\partial h_{F,j}(\varphi)}{\partial \varphi} = \frac{\Delta_r}{l_g} \left(\frac{\partial \bar{\varphi}}{\partial \varphi} \right) (\cos(\bar{\varphi}) \sin(\varphi_{s,j}) - \sin(\bar{\varphi}) \cos(\varphi_{s,j})) h_{F,j}^2(\varphi) . \quad (2.20)$$

2.3 Electric network

A general modeling method for the electric network with star interconnections is introduced in the following sections, which is also suitable to describe multiple OC fault cases. Commonly, within the MEC model, one constant electrical network for the HC case is considered, which simplifies the combination with the magnetic

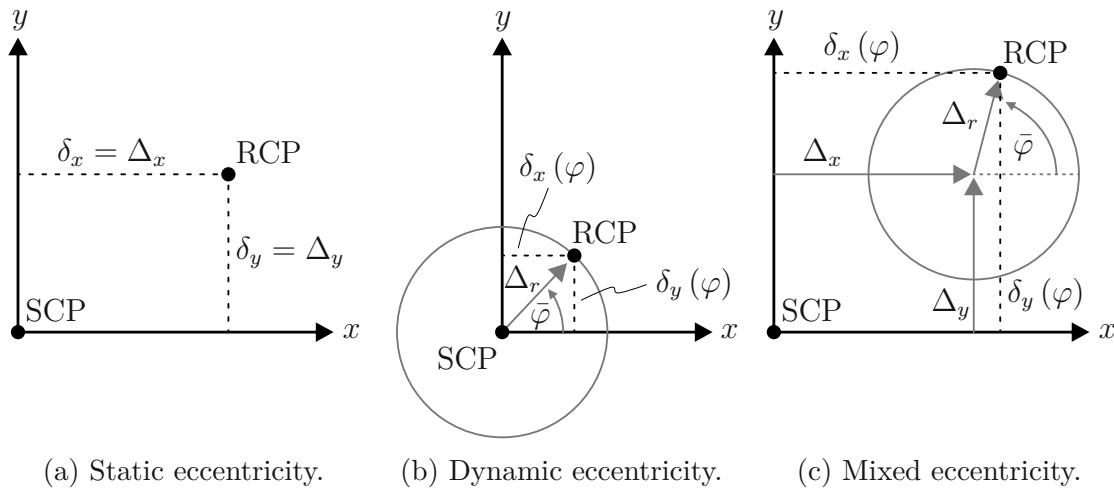


Figure 2.3: Eccentricity faults causing a displacement of the rotor center point (RCP) to the stator center point (SCP): a) Static eccentricity b) Dynamic eccentricity. c) Mixed eccentricity [16].

part [36, 37, 78]. However, fault cases introduce changes in the electrical network, which can be accounted for by switching the model structure or changing the model parameters to adapt the model to the fault case. A systematic framework for the electric circuit derivation is given in [77], where it is also applied to a multiphase PMSM with winding short-circuits. The fault case is considered in a separate model and this framework includes the model reduction, using auxiliary variables without direct physical interpretation.

The goals for the electrical network description of the investigated PMSM in this work are a general approach with flexibility for different electric coil interconnections and a systematical consideration of multiple OC fault cases. The derived electric network approach, including the system dynamics, generally applies to n_c stator coils. The utilized MEC model remains unchanged, but the set of algebraic equations is not uniquely solvable because it contains dependent variables. This model dependency is reduced within the electric network while the physical interpretation of the reduced set of variables is preserved. This is advantageous, as it simplifies considering multiple OC faults.

2.3.1 Dynamic model

In general, Faraday's law of induction describes the dynamic behavior of the PMSM

$$\frac{d}{dt}\boldsymbol{\psi}_c = -\mathbf{R}_c\mathbf{i}_c + \mathbf{v}_c, \quad (2.21)$$

2 Mathematical model of PMSMs

with the coil flux linkages $\boldsymbol{\psi}_c$, the coil currents \mathbf{i}_c , the electric coil voltages \mathbf{v}_c , and the diagonal stator coil resistance matrix

$$\mathbf{R}_c = \text{diag} \left[R_1 \quad \dots \quad R_{n_c} \right] \quad (2.22)$$

for n_c stator coils. For the HC case, $R_j = R_c$, $j = 1, \dots, n_c$, with the constant stator coil resistance R_c , holds. This is also assumed in the OC fault case for all healthy coils.

Combining the Faraday's induction law (2.21) together with the set of nonlinear algebraic equations (2.10) of the magnetic network yields

$$\frac{d}{dt} \boldsymbol{\psi}_c = -\mathbf{R}_c \mathbf{i}_c + \mathbf{v}_c \quad (2.23a)$$

$$\begin{bmatrix} \bar{\mathbf{D}}_c \boldsymbol{\mathcal{G}}_c \bar{\mathbf{D}}_c^T & \bar{\mathbf{D}}_c \boldsymbol{\mathcal{G}}_c \mathbf{D}_g^T \\ \mathbf{D}_g \boldsymbol{\mathcal{G}}_c \bar{\mathbf{D}}_c^T & \boldsymbol{\mathcal{G}}_t + \mathbf{D}_g \boldsymbol{\mathcal{G}}_c \mathbf{D}_g^T \end{bmatrix} \begin{bmatrix} \mathbf{i}_c \\ \mathbf{u}_{tg} \end{bmatrix} = \begin{bmatrix} \boldsymbol{\psi}_c \\ \mathbf{0} \end{bmatrix} - \begin{bmatrix} \bar{\mathbf{D}}_c \\ \mathbf{D}_g \end{bmatrix} \boldsymbol{\mathcal{G}}_c \mathbf{D}_m^T \mathbf{u}_{ms}, \quad (2.23b)$$

which represents a differential algebraic system of equations (DAE) of index 1. The model inputs are given by the coil voltages \mathbf{v}_c , which are considered as (virtual) control inputs described in Section 5.1.5.

2.3.2 Electric coil interconnections and model reduction

In this section, the electric network equations are derived for the HC case. The extension of this method for multiple OC fault cases will be given in Section 2.3.3. According to Kirchhoff's current law, it is apparent that the star interconnection implies that the sum of the coil currents at each neutral point NP is zero

$$\mathbf{i}_{c,\text{NP}} = \begin{bmatrix} \sum_{j=1}^{n_{\text{NP}1}} i_{c,j} \\ \sum_{j=1}^{n_{\text{NP}2}} i_{c,j} \\ \vdots \\ \sum_{j=1}^{n_{\text{NP}x}} i_{c,j} \end{bmatrix} = \mathbf{0}, \quad (2.24)$$

with n_{NP_x} representing the number of stator coils sharing the x -th common neutral point NP_x . This result introduces a dependent coil current for each neutral point, which decreases the DOFs for control tasks.

Furthermore, series connections of stator coils introduce dependent coil currents since the current is equal within series connection of stator coils. This also decreases the DOFs for control tasks, which can be considered as follows: For the

k -th phase with l series connected coils, let $i_{k,l}$ denote the l -th coil current. Then

$$\mathbf{i}_k = \begin{bmatrix} i_{k,1} - i_{k,2} \\ i_{k,1} - i_{k,3} \\ \vdots \\ i_{k,1} - i_{k,l} \end{bmatrix} = \mathbf{0} \quad (2.25)$$

holds and all n_k series connections are considered by

$$\mathbf{i}_{c,S} = [\mathbf{i}_1 \quad \mathbf{i}_2 \quad \dots \quad \mathbf{i}_{n_k}]^T = \mathbf{0} . \quad (2.26)$$

This concept is also suitable to describe distributed winding configurations in PMSMs.

The whole coil current dependencies are then combined by

$$\mathbf{i}_{c,d} = \begin{bmatrix} \mathbf{i}_{c,S} \\ \mathbf{i}_{c,NP} \end{bmatrix} = \mathbf{0} . \quad (2.27)$$

Note that the allocation of the vector entries in $\mathbf{i}_{c,d}$ is arbitrary. For consistency, lower coil numbers are stated first within each subgroup of $\mathbf{i}_{c,d}$. The elimination of these (dependent) coil currents from the set of variables is meaningful for numerical robustness and it assures faster computation times for the optimization and simulation tasks. Furthermore, the dependencies due to the star interconnection automatically removes the magnetic dependency within the algebraic set of equations as noted in Section 2.2.1.

The reduction step is introduced by the transformation

$$\begin{bmatrix} \mathbf{i}_{c,r} \\ \mathbf{i}_{c,d} \end{bmatrix} = \begin{bmatrix} \mathbf{H}_r^l \\ \mathbf{H}_d^l \end{bmatrix} \mathbf{i}_c = \mathbf{H}^l \mathbf{i}_c . \quad (2.28)$$

Thereby, the n_c coil currents \mathbf{i}_c are decomposed through the left-sided $n_c \times n_c$ matrix \mathbf{H}^l , with the entries -1 , 0 , or 1 , into a reduced set of n_r coil currents $\mathbf{i}_{c,r}$ and a dependent set of $n_d = n_c - n_r$ coil currents $\mathbf{i}_{c,d}$, with the total number of coils n_c and the number of reduced currents n_r , which corresponds to the available DOFs for control tasks. The specific choice of the reduced and dependent currents through the $n_r \times n_c$ matrix \mathbf{H}_r^l and the $n_d \times n_c$ matrix \mathbf{H}_d^l is arbitrary. Within this work, the following convention is used. First, the reduced currents comprise all coil currents sharing a common neutral point except the $n_{c,x}$ coil (coil with the highest number). Second, the row sum of \mathbf{H}_r^l equals one. The advantage of these specific choices of \mathbf{H}_r^l is that the currents $\mathbf{i}_{c,r}$ are identical to the respective coil currents. Analogously to the currents, the transformation of (2.28) is applied to split the flux linkages and voltages into a reduced set and a dependent set of variables. The

2 Mathematical model of PMSMs

application of this transformation (2.28) to all variables for currents, flux linkages and voltages to (2.23) yields the transformed system

$$\frac{d}{dt} \begin{bmatrix} \boldsymbol{\psi}_{c,r} \\ \boldsymbol{\psi}_{c,d} \end{bmatrix} = - \begin{bmatrix} \mathbf{H}_r^l \mathbf{R}_c \mathbf{H}_r^r & \mathbf{H}_r^l \mathbf{R}_c \mathbf{H}_d^r \\ \mathbf{H}_d^l \mathbf{R}_c \mathbf{H}_r^r & \mathbf{H}_d^l \mathbf{R}_c \mathbf{H}_d^r \end{bmatrix} \begin{bmatrix} \mathbf{i}_{c,r} \\ \mathbf{i}_{c,d} \end{bmatrix} + \begin{bmatrix} \mathbf{v}_{c,r} \\ \mathbf{v}_{c,d} \end{bmatrix} \quad (2.29a)$$

$$\begin{bmatrix} \mathbf{H}_r^l \bar{\mathbf{D}}_c \mathcal{G}_c \bar{\mathbf{D}}_c^T \mathbf{H}_r^r & \mathbf{H}_r^l \bar{\mathbf{D}}_c \mathcal{G}_c \bar{\mathbf{D}}_c^T \mathbf{H}_d^r & \mathbf{H}_r^l \bar{\mathbf{D}}_c \mathcal{G}_c \mathbf{D}_g^T \\ \mathbf{H}_d^l \bar{\mathbf{D}}_c \mathcal{G}_c \bar{\mathbf{D}}_c^T \mathbf{H}_r^r & \mathbf{H}_d^l \bar{\mathbf{D}}_c \mathcal{G}_c \bar{\mathbf{D}}_c^T \mathbf{H}_d^r & \mathbf{H}_d^l \bar{\mathbf{D}}_c \mathcal{G}_c \mathbf{D}_g^T \\ \mathbf{D}_g \mathcal{G}_c \bar{\mathbf{D}}_c^T \mathbf{H}_r^r & \mathbf{D}_g \mathcal{G}_c \bar{\mathbf{D}}_c^T \mathbf{H}_d^r & \mathcal{G}_t + \mathbf{D}_g \mathcal{G}_c \mathbf{D}_g^T \end{bmatrix} \begin{bmatrix} \mathbf{i}_{c,r} \\ \mathbf{i}_{c,d} \\ \mathbf{u}_{tg} \end{bmatrix} = \begin{bmatrix} \boldsymbol{\psi}_{c,r} \\ \boldsymbol{\psi}_{c,d} \\ \mathbf{0} \end{bmatrix} - \begin{bmatrix} \mathbf{H}_r^l \bar{\mathbf{D}}_c \\ \mathbf{H}_d^l \bar{\mathbf{D}}_c \\ \mathbf{D}_g \end{bmatrix} \mathcal{G}_c \mathbf{D}_m^T \mathbf{u}_{ms} , \quad (2.29b)$$

with right-sided matrix

$$\mathbf{H}^r = (\mathbf{H}^l)^{-1} = \begin{bmatrix} \mathbf{H}_r^r & \mathbf{H}_d^r \end{bmatrix} , \quad (2.30)$$

as the inverse of \mathbf{H}^l and the allocation of the $n_c \times n_r$ matrix \mathbf{H}_r^r and the $n_c \times n_d$ matrix \mathbf{H}_d^r .

The transformed system representation (2.29) allows the elimination of the dependent variables $\mathbf{i}_{c,d}$, $\boldsymbol{\psi}_{c,d}$, and $\mathbf{v}_{c,d}$ based on the following considerations:

1. The electric interconnection yields $\mathbf{i}_{c,d} = \mathbf{0}$.
2. Since equal coil resistances are assumed for all healthy coils, cf. Section 2.3.1, $\mathbf{H}_d^l \mathbf{R}_c \mathbf{H}_r^r = \mathbf{0}$ holds for the studied motor. This yields $\frac{d}{dt} \boldsymbol{\psi}_{c,d} = \mathbf{v}_{c,d}$. Since it is impossible to control $\mathbf{v}_{c,d}$ by means of the terminal voltages \mathbf{v}_t , $\boldsymbol{\psi}_{c,d}$ and $\mathbf{v}_{c,d}$ are irrelevant for the control task and hence not further considered. Note that the sum of vector entries in $\boldsymbol{\psi}_{c,d}$ for $\mathbf{i}_{c,d} = \mathbf{i}_{c, \text{NP}}$, e.g., no series connection, is always zero, which directly results from Gauss's law for magnetism.
3. Finally, this also allows eliminating the second row of (2.29b) from the set of equations.

By applying these considerations, the resulting reduced DAE system then reads as

$$\frac{d}{dt} \boldsymbol{\psi}_{c,r} = -\mathbf{H}_r^l \mathbf{R}_c \mathbf{H}_r^r \mathbf{i}_{c,r} + \mathbf{v}_{c,r} \quad (2.31a)$$

$$\begin{bmatrix} \mathbf{H}_r^l \bar{\mathbf{D}}_c \mathcal{G}_c \bar{\mathbf{D}}_c^T \mathbf{H}_r^r & \mathbf{H}_r^l \bar{\mathbf{D}}_c \mathcal{G}_c \mathbf{D}_g^T \\ \mathbf{D}_g \mathcal{G}_c \bar{\mathbf{D}}_c^T \mathbf{H}_r^r & \mathcal{G}_t + \mathbf{D}_g \mathcal{G}_c \mathbf{D}_g^T \end{bmatrix} \begin{bmatrix} \mathbf{i}_{c,r} \\ \mathbf{u}_{tg} \end{bmatrix} = \begin{bmatrix} \boldsymbol{\psi}_{c,r} \\ \mathbf{0} \end{bmatrix} - \begin{bmatrix} \mathbf{H}_r^l \bar{\mathbf{D}}_c \\ \mathbf{D}_g \end{bmatrix} \mathcal{G}_c \mathbf{D}_m^T \mathbf{u}_{ms} . \quad (2.31b)$$

The reduced system (2.31) is of minimum state, and the algebraic equations no longer contain any redundant equations, cf. [77] for a more detailed analysis.

2.3.3 Multiple open-circuit fault cases

An open connection in the electrical path between the power source and the common neutral point specifies an OC fault case of a particular stator coil. Thus, the faulty stator coil current equals zero. The fault can have different causes, i.e., broken cables or wire disconnections within the electrical path, malfunction or loose bond-wire contacts of the half-bridge, and wire disconnection within the stator coil, cf. [4, 10, 16]. However, the OC fault's particular cause is irrelevant to the subsequent modeling. Two different modeling approaches dealing with multiple OC faults are presented in the following. The first approach reduces the model structure to the available DOFs, while the second approach preserves the model structure.

Model structure reduction

Let $\mathbf{i}_{c,f}$ denote the vector of faulty coil currents. For OC faults, $\mathbf{i}_{c,f} = \mathbf{0}$ holds, which renders the coil currents uncontrollable by the control inputs. Thus, it makes sense to eliminate these coil currents and the corresponding flux linkages from the set of equations (2.31). To do so, the currents of the faulty coils extend the vector of dependent currents, cf. (2.27),

$$\mathbf{i}_{c,d} = \begin{bmatrix} \mathbf{i}_{c,f} \\ \mathbf{i}_{c,S} \\ \mathbf{i}_{c,NP} \end{bmatrix} = \mathbf{0} . \quad (2.32)$$

Again, note that the allocation of the vector entries in $\mathbf{i}_{c,d}$ is arbitrary. All faulty coil currents have to be removed from the reduced current vector $\mathbf{i}_{c,r}$. Suppose a faulty coil does not belong to the reduced currents, a substitute coil current is eliminated to take the reduced DOFs into account. The new allocation is then considered by the matrices \mathbf{H}^l and \mathbf{H}^r , which are adjusted accordingly.

This general procedure is applicable to all possible OC fault cases. Using this modeling approach for multiple OC cases results in changes in the model order depending on the position and number of OC faults. While this is irrelevant to calculating optimal current patterns (as will be described in Section 4.3), it makes dynamic simulations challenging, particularly if the occurrence of an OC during operation is studied. Furthermore, it can be interesting to study the transition from a healthy to a total OC fault, where a slow increase of the effective coil resistance characterizes the fault. Therefore, an approach preserving the model structure is presented next.

2 Mathematical model of PMSMs

Preserving model structure

A modeling approach preserving the model structure is beneficial for studying the transition from healthy to a total OC fault in simulation. Starting from the DAE model of (2.31), all investigated OC fault coils must be known in advance. As the consideration of reduced (independent) coil currents can be ambiguous, all affected OC fault coil currents must be considered as reduced currents. Then, OC fault cases are emulated by adding a fictive resistance ΔR in the electrical path of the corresponding faulty stator coils, which significantly increases the faulty coils' resistance values $R_{c,f} = R_c + \Delta R$. Choosing ΔR large enough yields very small coil currents, thus allowing to approximate even a total OC fault with sufficient accuracy. The ideal fictive resistance value would be infinity according to (2.31a). This leads to a numerically stiff system and is difficult to solve in an acceptable amount of time. Therefore, the fictive resistance value is selected to keep the affected OC fault coil current in the range of the current sensor's noise amplitude. Due to the impact of the rotational speed on the left side of (2.31a), the fictive resistance value is given by $\Delta R = R_c \omega / \omega_{ref}$, with the rotational speed ω and a suitable reference speed ω_{ref} . Utilizing a suitable solver, e.g., the solver ODE23TB of MATLAB/SIMULINK gives fast and accurate results for the multiple OC cases studied in this work. However, the model stiffness is pronounced for a higher number of considered faulty coils, leading to increased simulation times. For single, double, and triple adjacent OC fault cases, the simulation time increases about the factors 2, 2.5, and 3, respectively, compared to the HC case.

2.4 Application of the electric network

The electrical network is applied to the following three electrical coil interconnections for the investigated PMSM: a quadruple three-phase system, a single star system, and a single three-phase system with four coils connected in series in each case.

2.4.1 Quadruple three-phase system (4×3)

The quadruple three-phase system (4×3) is given by four sets of three-phase systems, with an isolated neutral point for each set. The electrical network for this coil interconnection is given in Fig. 2.4. The electric coil interconnection is

2.4 Application of the electric network

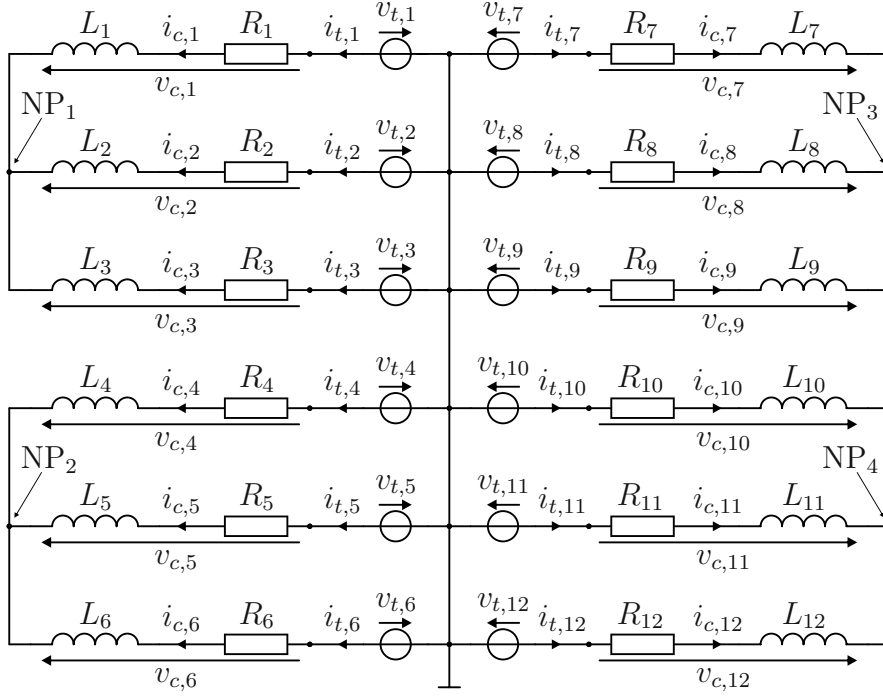


Figure 2.4: Electrical network for the healthy-circuit (HC) case in quadruple three-phase systems in star (wye) configuration with separate isolated neutral points (4×3).

considered by the dependent coil currents consisting of

$$\mathbf{i}_{c,d} = \mathbf{i}_{c,\text{NP}} = \begin{bmatrix} i_{c,1} + i_{c,2} + i_{c,3} \\ i_{c,4} + i_{c,5} + i_{c,6} \\ i_{c,7} + i_{c,8} + i_{c,9} \\ i_{c,10} + i_{c,11} + i_{c,12} \end{bmatrix} = \mathbf{0} \quad (2.33)$$

according to (2.27) and (2.24), resulting in $n_d = \dim(\mathbf{i}_{c,d}) = 4$. The independent currents are chosen as the first two coils of each three-phase system. Thus, the vector of reduced currents is given by

$$\mathbf{i}_{c,r} = [i_{c,1} \ i_{c,2} \ i_{c,4} \ i_{c,5} \ i_{c,7} \ i_{c,8} \ i_{c,10} \ i_{c,11}]^T. \quad (2.34)$$

With $n_r = \dim(\mathbf{i}_{c,r}) = 8$, this coil allocation reflects the eight DOFs and the matrices \mathbf{H}_r^l and \mathbf{H}_d^l are defined as

$$\mathbf{H}_r^l = \begin{bmatrix} \mathbf{H}_1 & \mathbf{0} & \mathbf{0} & \mathbf{0} \\ \mathbf{0} & \mathbf{H}_1 & \mathbf{0} & \mathbf{0} \\ \mathbf{0} & \mathbf{0} & \mathbf{H}_1 & \mathbf{0} \\ \mathbf{0} & \mathbf{0} & \mathbf{0} & \mathbf{H}_1 \end{bmatrix} \quad (2.35a)$$

2 Mathematical model of PMSMs

and

$$\mathbf{H}_d^l = \begin{bmatrix} \mathbf{H}_2 & \mathbf{0} & \mathbf{0} & \mathbf{0} \\ \mathbf{0} & \mathbf{H}_2 & \mathbf{0} & \mathbf{0} \\ \mathbf{0} & \mathbf{0} & \mathbf{H}_2 & \mathbf{0} \\ \mathbf{0} & \mathbf{0} & \mathbf{0} & \mathbf{H}_2 \end{bmatrix}, \quad (2.35b)$$

with

$$\mathbf{H}_1 = \begin{bmatrix} 1 & 0 & 0 \\ 0 & 1 & 0 \end{bmatrix}, \quad (2.35c)$$

$$\mathbf{H}_2 = [1, 1, 1]. \quad (2.35d)$$

The matrix \mathbf{H}^r is calculated analogously to (2.30) and is composed of the following matrices

$$\mathbf{H}_r^r = \begin{bmatrix} \mathbf{H}_3 & \mathbf{0} & \mathbf{0} & \mathbf{0} \\ \mathbf{0} & \mathbf{H}_3 & \mathbf{0} & \mathbf{0} \\ \mathbf{0} & \mathbf{0} & \mathbf{H}_3 & \mathbf{0} \\ \mathbf{0} & \mathbf{0} & \mathbf{0} & \mathbf{H}_3 \end{bmatrix}, \quad (2.36a)$$

$$\mathbf{H}_d^r = \begin{bmatrix} \mathbf{H}_4 & \mathbf{0} & \mathbf{0} & \mathbf{0} \\ \mathbf{0} & \mathbf{H}_4 & \mathbf{0} & \mathbf{0} \\ \mathbf{0} & \mathbf{0} & \mathbf{H}_4 & \mathbf{0} \\ \mathbf{0} & \mathbf{0} & \mathbf{0} & \mathbf{H}_4 \end{bmatrix} \quad (2.36b)$$

with

$$\mathbf{H}_3 = \begin{bmatrix} 1 & 0 \\ 0 & 1 \\ -1 & -1 \end{bmatrix}, \quad (2.36c)$$

$$\mathbf{H}_4 = [0 \ 0 \ 1]^T. \quad (2.36d)$$

Following the steps for the transformation of the system, a reduced set of equations of the form (2.31) is directly given for the HC case by applying the derived auxiliary matrices of (2.35a) and (2.36a). Each three-phase set contains two DOFs. The overall dimension of (2.31b) consist of $n_r + \dim(\mathbf{u}_{tg}) = 8 + 28 = 36$ unknown variables for the set of nonlinear algebraic equations.

Multiple OC fault cases (4×3)

A single OC fault within a three-phase set reduces the available DOFs by one, and both remaining coil currents are have the identical amplitude but opposite signs.

2.4 Application of the electric network

Double OC faults within a three-phase set are uncontrollable and automatically become a total failure of the whole three-phase set. This case is considered as a triple adjacent OC fault. Double OC faults in different three-phase sets reduce the available DOFs to six.

For example, the double OC fault case with the faulty coils $f_1 = 3$ and $f_2 = 4$ in the 4×3 configuration is explained. According to (2.32), the vector of dependent currents is extended to

$$\mathbf{i}_{c,d} = \begin{bmatrix} i_{c,3} \\ i_{c,1} + i_{c,2} + i_{c,3} \\ i_{c,4} \\ i_{c,4} + i_{c,5} + i_{c,6} \\ i_{c,7} + i_{c,8} + i_{c,9} \\ i_{c,10} + i_{c,11} + i_{c,12} \end{bmatrix}. \quad (2.37)$$

The loss of the two DOFs is accounted for in the vector of reduced currents

$$\mathbf{i}_{c,r} = [i_{c,1} \quad i_{c,5} \quad i_{c,7} \quad i_{c,8} \quad i_{c,10} \quad i_{c,11}]^T \quad (2.38)$$

by removing each faulty coil $\mathbf{i}_{c,f}$ or a substitute coil to consider the loss of DOFs. Here, instead of the faulty coil $i_{f,1} = i_{c,3}$, the coil $i_{c,2}$ is removed. Then, the auxiliary matrices \mathbf{H}_r^l and \mathbf{H}_d^l are redefined as

$$\mathbf{H}_r^l = \begin{bmatrix} \mathbf{H}_{1,f1} & \mathbf{0} & \mathbf{0} & \mathbf{0} \\ \mathbf{0} & \mathbf{H}_{1,f2} & \mathbf{0} & \mathbf{0} \\ \mathbf{0} & \mathbf{0} & \mathbf{H}_1 & \mathbf{0} \\ \mathbf{0} & \mathbf{0} & \mathbf{0} & \mathbf{H}_1 \end{bmatrix} \quad (2.39a)$$

and

$$\mathbf{H}_d^l = \begin{bmatrix} \mathbf{H}_{2,f1} & \mathbf{0} & \mathbf{0} & \mathbf{0} \\ \mathbf{0} & \mathbf{H}_{2,f2} & \mathbf{0} & \mathbf{0} \\ \mathbf{0} & \mathbf{0} & \mathbf{H}_2 & \mathbf{0} \\ \mathbf{0} & \mathbf{0} & \mathbf{0} & \mathbf{H}_2 \end{bmatrix}, \quad (2.39b)$$

with

$$\mathbf{H}_{1,f1} = \begin{bmatrix} 1 & 0 & 0 \end{bmatrix} \quad (2.39c)$$

$$\mathbf{H}_{1,f2} = \begin{bmatrix} 0 & 1 & 0 \end{bmatrix} \quad (2.39d)$$

$$\mathbf{H}_{2,f1} = \begin{bmatrix} 0 & 0 & 1 \\ 1 & 1 & 1 \end{bmatrix} \quad (2.39e)$$

$$\mathbf{H}_{2,f2} = \begin{bmatrix} 1 & 0 & 0 \\ 1 & 1 & 1 \end{bmatrix}. \quad (2.39f)$$

2 Mathematical model of PMSMs

and \mathbf{H}_1 and \mathbf{H}_2 from (2.35c) and (2.35d). Following the identical steps for the transformation of the system, a reduced set of equations of the form (2.31) is also obtained for the multiple OC fault case.

2.4.2 Single star twelve-phase system (1×12)

The electric network for a single star system with 12 stator coils is given in Fig. 2.5. The dependent coil current is given by the sum of all coil currents

$$i_{c,d} = i_{c, \text{NP}} = \sum_{j=1}^{12} i_{c,j} = 0 \quad (2.40)$$

according to (2.24) and (2.27) with $n_d = \dim(i_{c,d}) = 1$. The independent coil currents are chosen as the first eleven ones

$$\mathbf{i}_{c,r} = [i_{c,1} \ \dots \ i_{c,11}]^T, \quad (2.41)$$

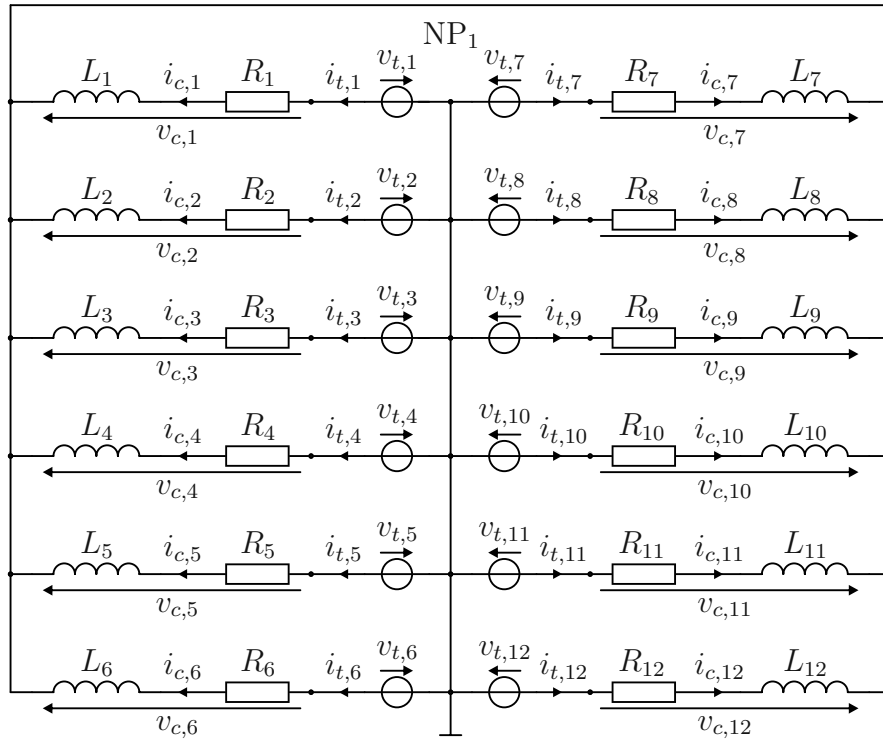


Figure 2.5: Electrical network for the healthy-circuit (HC) case in a single star configuration with common isolated neutral point (1×12).

which results in $n_r = \dim(\mathbf{i}_{c,r}) = 11$ DOFs. The auxiliary matrices then read as

$$\mathbf{H}_r^l = \begin{bmatrix} \mathbf{I}_{11 \times 11} & \mathbf{0}_{11 \times 1} \end{bmatrix} \quad (2.42a)$$

and

$$\mathbf{H}_d^l = \mathbf{1}_{1 \times 12}, \quad (2.42b)$$

with the vector $\mathbf{1}$ containing only ones of the suitable size. Analogously to (2.30), \mathbf{H}_r^r is given by

$$\mathbf{H}_r^r = \begin{bmatrix} \mathbf{I}_{11 \times 11} \\ -\mathbf{1}_{1 \times 11} \end{bmatrix} \quad (2.43a)$$

and

$$\mathbf{H}_d^r = \begin{bmatrix} 0 & \dots & 0 & 1 \end{bmatrix}^T. \quad (2.43b)$$

Again, following the identical transformation steps, with the matrices of (2.42a) and (2.43a), the reduced set of equations for the HC case is given by (2.31). The dimension of the differential equation (2.31a) is specified by $n_r = 11$. The algebraic system (2.31b) contains of $n_r + \dim(\mathbf{u}_{tg}) = 11 + 28 = 39$ unknown variables. For the single star system, the dependent flux linkages directly equal Gauss's law for magnetism, e.g., $\psi_{c,d} = \sum_{j=1}^{12} \psi_{c,j} = 0$.

Remark 1. The main difference between the 4×3 and the 1×12 configuration is the additional constraint due to Kirchoff's current law at the four neutral points in the 4×3 configuration, cf. Fig. 2.4 and Fig. 2.5. Although two neighboring three-phase systems are decoupled regarding the currents, they are still coupled due to the magnetic flux distribution.

Multiple OC fault cases (1×12)

Multiple OC fault cases in the 1×12 configuration are considered by augmenting the dependent currents. For example, the double OC fault case with the faulty coils $f_1 = 3$ and $f_2 = 4$ in the 1×12 configuration is explained. According to (2.32), the vector of dependent currents is extended to

$$\mathbf{i}_{c,d} = \begin{bmatrix} i_{c,3} \\ i_{c,4} \\ \sum_{j=1}^{12} i_{c,j} \end{bmatrix}, \quad (2.44)$$

2 Mathematical model of PMSMs

and \mathbf{H}_r^l and \mathbf{H}_d^l are defined as

$$\mathbf{H}_r^l = \begin{bmatrix} \mathbf{I}_{2 \times 2} & \mathbf{0}_{2 \times 2} & \mathbf{0}_{2 \times 7} & \mathbf{0}_{2 \times 1} \\ \mathbf{0}_{7 \times 2} & \mathbf{0}_{7 \times 2} & \mathbf{I}_{7 \times 7} & \mathbf{0}_{7 \times 1} \end{bmatrix} \quad (2.45a)$$

and

$$\mathbf{H}_d^l = \begin{bmatrix} \mathbf{0}_{2 \times 2} & \mathbf{I}_{2 \times 2} & \mathbf{0}_{2 \times 8} \\ \mathbf{I}_{1 \times 2} & \mathbf{I}_{1 \times 2} & \mathbf{I}_{1 \times 8} \end{bmatrix}. \quad (2.45b)$$

Following the identical steps for the transformation of the system, a reduced set of equations of the form (2.31) is also obtained for the multiple OC fault case. The reduced vector of coil currents reads as

$$\mathbf{i}_{c,r} = [i_{c,1} \quad i_{c,2} \quad i_{c,5} \quad \dots \quad i_{c,11}]^T \quad (2.46)$$

for the example of faulty coils $f_1 = 3$ and $f_2 = 4$ in the 1×12 configuration.

2.4.3 Single three-phase system (1×3)

The electric network of a single three-phase system for 12 stator coils is introduced for the utilization in the model calibration process, cf. Section 3.2. The stator coil interconnection is given in Fig. 2.6. Thereby, each of the three phases contains the series interconnection of four stator coils. This means that the coils 1, 4, 7, 10, the coils 2, 5, 8, 11, and the coils 3, 6, 9, 12 are each connected in series. The terminal connections are labeled with a , b , and c for the three phases. According to the general framework for series coil interconnections, this yields $k = 3$ and $l = 4$ with

$$\mathbf{i}_{c,S} = \begin{bmatrix} \mathbf{i}_1 \\ \mathbf{i}_2 \\ \mathbf{i}_3 \end{bmatrix} = \mathbf{0} \quad (2.47a)$$

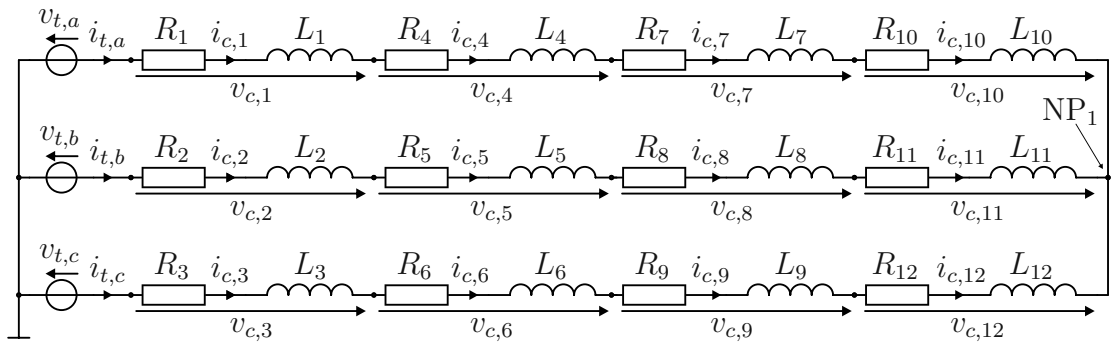


Figure 2.6: Electrical network for the healthy-circuit (HC) case in a single star three-phase series configuration with common isolated neutral point (1×3).

2.4 Application of the electric network

and

$$\mathbf{i}_1 = \begin{bmatrix} i_{c,1} - i_{c,4} \\ i_{c,1} - i_{c,7} \\ i_{c,1} - i_{c,10} \end{bmatrix}, \quad \mathbf{i}_2 = \begin{bmatrix} i_{c,2} - i_{c,5} \\ i_{c,2} - i_{c,8} \\ i_{c,2} - i_{c,11} \end{bmatrix}, \quad \mathbf{i}_3 = \begin{bmatrix} i_{c,3} - i_{c,6} \\ i_{c,3} - i_{c,9} \\ i_{c,3} - i_{c,12} \end{bmatrix}. \quad (2.47b)$$

The currents at the isolated neutral star point are considered by

$$i_{c,NP} = i_{c,1} + i_{c,2} + i_{c,3} = 0. \quad (2.48)$$

The dependent currents $\mathbf{i}_{c,d}$ are composed of (2.47) and (2.48) according to (2.27). The resulting two DOFs are chosen as the first two coil currents which yields

$$\mathbf{i}_{c,r} = [i_{c,1} \quad i_{c,2}]^T. \quad (2.49)$$

The transformation matrices are then defined as

$$\mathbf{H}_r^l = [\mathbf{I}_{2 \times 2} \quad \mathbf{0}_{2 \times 10}] \quad (2.50a)$$

and

$$\mathbf{H}_d^l = \begin{bmatrix} 1 & 0 & 0 & -1 & 0 & 0 & 0 & 0 & 0 & 0 & 0 & 0 \\ 1 & 0 & 0 & 0 & 0 & 0 & -1 & 0 & 0 & 0 & 0 & 0 \\ 1 & 0 & 0 & 0 & 0 & 0 & 0 & 0 & 0 & -1 & 0 & 0 \\ 0 & 1 & 0 & 0 & -1 & 0 & 0 & 0 & 0 & 0 & 0 & 0 \\ 0 & 1 & 0 & 0 & 0 & 0 & 0 & -1 & 0 & 0 & 0 & 0 \\ 0 & 1 & 0 & 0 & 0 & 0 & 0 & 0 & 0 & 0 & -1 & 0 \\ 0 & 0 & 1 & 0 & 0 & -1 & 0 & 0 & 0 & 0 & 0 & 0 \\ 0 & 0 & 1 & 0 & 0 & 0 & 0 & 0 & -1 & 0 & 0 & 0 \\ 0 & 0 & 1 & 0 & 0 & 0 & 0 & 0 & 0 & 0 & 0 & -1 \\ 1 & 1 & 1 & 0 & 0 & 0 & 0 & 0 & 0 & 0 & 0 & 0 \end{bmatrix} \quad (2.50b)$$

and \mathbf{H}_r^r and \mathbf{H}_d^r are given according to (2.30) by

$$\mathbf{H}_r^r = \begin{bmatrix} \mathbf{H}_3 \\ \mathbf{H}_3 \\ \mathbf{H}_3 \\ \mathbf{H}_3 \end{bmatrix} \quad (2.51a)$$

2 Mathematical model of PMSMs

and

$$\mathbf{H}_d^r = \begin{bmatrix} 0 & 0 & 0 & 0 & 0 & 0 & 0 & 0 & 0 & 0 \\ 0 & 0 & 0 & 0 & 0 & 0 & 0 & 0 & 0 & 0 \\ 0 & 0 & 0 & 0 & 0 & 0 & 0 & 0 & 0 & 1 \\ -1 & 0 & 0 & 0 & 0 & 0 & 0 & 0 & 0 & 0 \\ 0 & 0 & 0 & -1 & 0 & 0 & 0 & 0 & 0 & 0 \\ 0 & 0 & 0 & 0 & 0 & 0 & -1 & 0 & 0 & 1 \\ 0 & -1 & 0 & 0 & 0 & 0 & 0 & 0 & 0 & 0 \\ 0 & 0 & 0 & 0 & -1 & 0 & 0 & 0 & 0 & 0 \\ 0 & 0 & 0 & 0 & 0 & 0 & 0 & -1 & 0 & 1 \\ 0 & 0 & -1 & 0 & 0 & 0 & 0 & 0 & 0 & 0 \\ 0 & 0 & 0 & 0 & 0 & -1 & 0 & 0 & 0 & 0 \\ 0 & 0 & 0 & 0 & 0 & 0 & 0 & 0 & -1 & 1 \end{bmatrix}, \quad (2.51b)$$

with \mathbf{H}_3 given by (2.36c). With these definitions and following the identical transformation steps of the system, the reduced set of equations based on (2.31) is given for the HC case by with the auxiliary matrices of (2.50a) and (2.51a). Here, the dimension of the differential equation (2.31a) is given by $n_r = 2$. Therefore, the algebraic system (2.31b) contains of $n_r + \dim(\mathbf{u}_{tg}) = 2 + 28 = 30$ unknown variables.

The derived mathematical model in this chapter describes the nonlinear magnetic effects, torques, and radial forces of the considered PMSM. It is flexible for different electrical coil interconnections and multiple OC faults. This model is applied to the 1×12 and 4×3 configuration for further investigation and serves as basis for the model-based control strategy, cf. Chapter 4 and Chapter 5. However, this model needs to be calibrated with the measurements described in the next chapter.

3

Model calibration and validation

Parts of this chapter were published in similar form in the author's previous publications [1, 2].

While many parameters of the magnetic equivalent circuit (MEC) motor model are directly obtained from the construction and material data of the motor, specific parameters, such as the exact shape of the air gap or leakage permeances, are difficult to estimate from construction parameters [78]. Furthermore, the real-world behavior of the voltage source inverter (VSI) used to drive the permanent magnet synchronous machine (PMSM) is not easily obtained from its construction. Therefore, the calibration and validation of the dynamical model are presented in this chapter.

First, the utilized test stand and the multiphase VSI with its nonlinear behavior and static compensation are presented. Then, the MEC model calibration procedure is given based on an optimization problem. Finally, the high model accuracy is proven by measurements on the test stand.

3.1 Test stand

The mechanical setup of the test stand is depicted in Fig. 3.1. It comprises the considered PMSM, an incremental encoder (ENC), a torque sensor (TS), a flywheel (FW), and a load motor, which can be changed between a harmonic drive (HD) or an induction machine (IM). All elements are mechanically connected with couplings. The harmonic drive load motor has a high gear ratio of 160:1, which allows for precise position and low-speed operation, whereas the IM is used at higher speeds. The PMSM is controlled by 12 individual half-bridges distributed on four three-phase boards forming the VSI, cf. Section 3.1.1. The utilized hardware to

3 Model calibration and validation

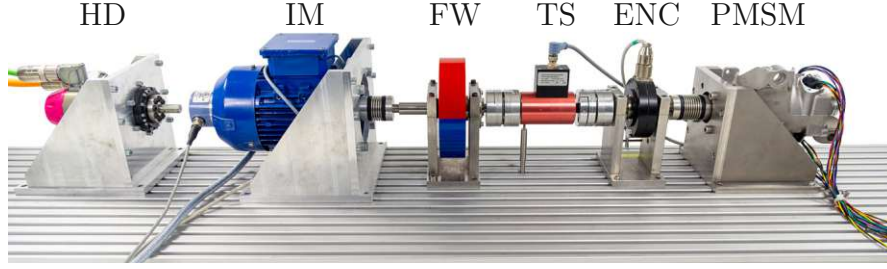


Figure 3.1: Setup of the test stand: harmonic drive (HD), induction machine (IM), flywheel (FW), torque sensor (TS), rotary encoder (ENC), multiphase PMSM (PMSM).

drive the system consists of a dSpace DS5203 FPGA board, a dSpace DS1007 processing unit, and a dSpace DS2004 ADC board [87]. The VSI is operated at a 10 kHz pulse width modulation (PWM), whose switching patterns are generated on the FPGA board. The coil currents are measured via oversampling for 801 measuring points by 12 ADCs on the FPGA board. The rotary encoder signals with 5000 increments per revolution are recorded via digital input channels. The ADC board is used to measure the dc-link voltages of each board and the torque sensor signal.

3.1.1 Voltage source inverter

The voltage source inverter (VSI) consists of four identical boards (B_1, \dots, B_4), each equipped with three half-bridges and supplied by common dc-link voltages $v_{dc}^{B_1}, \dots, v_{dc}^{B_4}$, forming together the diagonal dc-link voltages matrix

$$\mathbf{V}_{dc} = \text{diag} \left[v_{dc}^{B_1} \mathbf{I}_{3 \times 3} \quad v_{dc}^{B_2} \mathbf{I}_{3 \times 3} \quad v_{dc}^{B_3} \mathbf{I}_{3 \times 3} \quad v_{dc}^{B_4} \mathbf{I}_{3 \times 3} \right]. \quad (3.1)$$

Each half-bridge has a current measurement shunt located in the load path. Figure 3.2 shows the VSI boards with the investigated motor in the 4×3 configuration. Assuming an ideal VSI, the average terminal voltage \mathbf{v}_t results in the form

$$\mathbf{v}_t = \mathbf{V}_{dc} \boldsymbol{\delta}, \quad (3.2)$$

with the vector of duty cycles $\boldsymbol{\delta} = [\delta_1, \dots, \delta_{12}]^T$ ranging from 0 to 1 of the symmetric pulse-width modulation (PWM). The VSI has a current-dependent internal voltage drop $\mathbf{v}^{\text{VSI}}(\mathbf{i}_c)$, which should be compensated for high-performance operation. $\mathbf{v}^{\text{VSI}}(\mathbf{i}_c)$ is identified based on measurements at constant rotor positions of the PMSM in the 4×3 configuration. To do so, the desired duty cycles

$$\boldsymbol{\delta}^d = \mathbf{V}_{dc}^{-1} \mathbf{R}_c \mathbf{i}_c^d + 0.51 \quad (3.3)$$

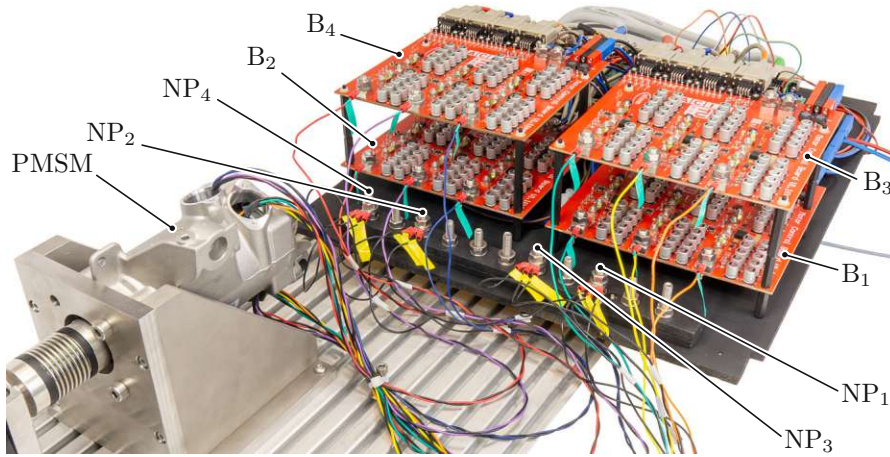


Figure 3.2: VSI setup with four three-phase boards (B_1 - B_4). The figure shows the 4×3 configuration with four isolated neutral points (NP_1 - NP_4).

are applied to the VSI, where \mathbf{R}_c is the resistance value of the healthy PMSM, cf. Section 2.3.1, and a slow triangular-shaped desired current trajectory \mathbf{i}_c^d with amplitude up to twice the nominal current i_n is used. The stator coil resistance R_c is determined by averaging static measurements for constant currents without considering temperature effects. The measured signals show a pronounced linear error of the VSI, which can be modeled well by

$$\mathbf{v}^{\text{VSI}} = \text{diag} [R_1^{\text{VSI}} \quad \dots \quad R_{12}^{\text{VSI}}] \mathbf{i}_c, \quad (3.4)$$

with the effective resistances R_j^{VSI} , $j = 1, \dots, 12$ of the VSI. With multiple measurements for the desired currents for the three dominant magnetic directions 0° , 120° , 240° of the motor, R_j^{VSI} are identified by least-squares estimation. As the differences between the identified resistances are low, the mean value

$$R^{\text{VSI}} = \frac{1}{12} \sum_{j=1}^{12} R_j^{\text{VSI}} \quad (3.5)$$

is considered. The VSI nonlinearities are shown in Fig. 3.3 for the dominant magnetic direction 0° of coil 1. The left plot shows the desired current's slow trajectory and the measured current over time. The right plot shows the voltage error without compensation and the remaining voltage error after the compensation. The resulting error cannot be further reduced due to the opposite voltage errors of the remaining two coils within the three-phase system. A further reduction of the VSI error with a static compensation is difficult due to the nonlinear behavior of the utilized half-bridges [88]. While the main VSI errors are compensated with this approach, the remaining nonlinear error must be suppressed by a feedback current controller, see Chapter 5.

3 Model calibration and validation

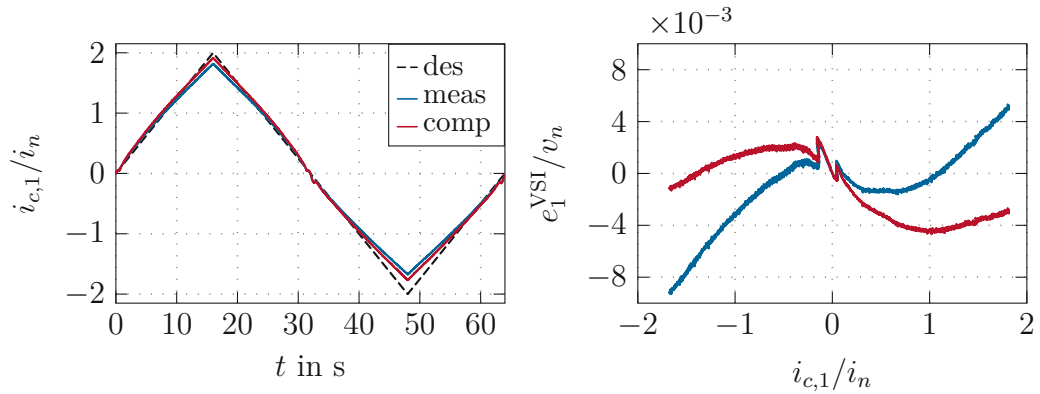


Figure 3.3: Measured and compensated VSI nonlinearities for coil 1 in the 4×3 configuration.

3.1.2 Open-circuit fault emulation

The open-circuit (OC) fault cases are emulated on the test stand in two different ways. In general, to evaluate the OC post-fault performance, the affected coils are physically disconnected from the VSI legs before the experiments are performed. This case is similar to real OC fault cases and is applied in most experiments.

However, evaluating the fault diagnosis method in Section 6.2 requires a different approach, as transitions of OC fault cases are investigated. The commonly utilized strategy of deactivating the half-bridges, see, e.g., [70], does not result in fully opening the phase, as the bypass diodes are still present and allow for an, in this case, undesired current flow. Therefore, relays are integrated into the phases c_1 , c_2 , and c_3 between the stator coils and the corresponding VSI legs, which are controlled by the digital outputs of the dSpace system. This setup, extended by the relays, is depicted in Fig. 3.4 for the 1×12 configuration. The integration of the relays increases the resistance values within the first three VSI legs due to the contact resistances and the short extension wires. This has only a minor influence on the control performance and can be neglected since the focus is on the fault diagnosis behavior and switching of the control strategies.

3.2 Model calibration

With the model calibration, the unknown model parameters of the magnetic circuit (2.10) are determined by the solution of an optimization problem. As mentioned in Section 2.2, the permeances of the rotor yoke, the rotor bar, the permanent magnets, and the stator coils are determined from the known geometry and material

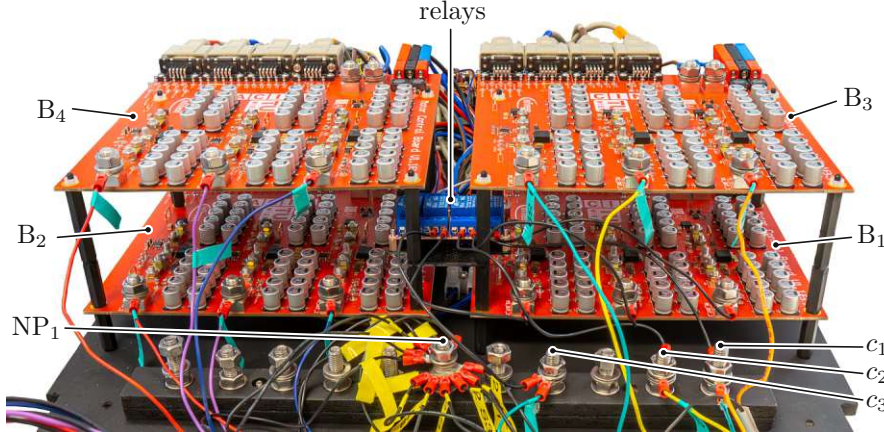


Figure 3.4: VSI setup with four three-phase boards (B_1 - B_4) in the 1×12 configuration with three relays connected between B_1 and the coils c_1 - c_3 .

parameters of the investigated PMSM [78]. Since the shape of the air gap permeances is modeled by a sum of Gaussian functions, cf. Section 2.2.3, the parameters of those Gaussian functions need to be calibrated through measurements.

A static model calibration aiming at high torque accuracy was performed for the investigated PMSM in a previous work [36], by calibrating the air gap permeances \mathcal{G}_a . This calibration approach was extended for a different PMSM in [77] by calibrating the stator leakage permeance \mathcal{G}_{sl} , which increases the coil inductance accuracy. This is beneficial since the accuracy of dynamic electric model can be enhanced. To do so, the stator leakage permeances are approximated by

$$\mathcal{G}_{sl} = \eta \mathcal{G}_{sl,nom} , \quad (3.6)$$

where $\mathcal{G}_{sl,nom}$ is the nominal value obtained by flux tube approximation of the leakage path and η is a scalar tuning factor.

All model calibration parameters are combined in the vector

$$\mathbf{x}_c = \left[A_0 \quad \dots \quad A_{n_g} \quad \sigma_0 \quad \dots \quad \sigma_{n_g} \quad \Delta\varphi_1 \quad \dots \quad \Delta\varphi_{n_g} \quad \eta \right]^T , \quad (3.7)$$

with the amplitudes A_0 and A_k , the width σ_0 and σ_k and the shifts $\Delta\varphi_k$ of the Gaussian functions according to (2.14) and the tuning factor η for the leakage permeances. The optimal model parameters are obtained by solving a constrained optimization problem based on measurements. This approach follows the main ideas of [77]. As the electric coil interconnection is irrelevant for calibrating the magnetic parameters, the PMSM is connected in the 1×3 star configuration for the healthy-circuit (HC) case, cf. Section 2.4.3, to limit the signals to a minimum number due to the reduced electric degrees of freedom (DOFs) of two. Consequently, the assumption of equal stator coils is applied. Following the approach in

3 Model calibration and validation

[77], the model calibration is based on the following measurements on a test stand, cf. Section 3.1:

- very slow (3 rpm) rotating torque measurements for constant currents ($i_a = 1.5i_n$, $i_b = i_c = -0.75i_n$), which are evaluated for $n_r = 90$ rotor positions $\varphi_r = 1, 2, \dots, 90^\circ$.
- back-electromotive force (BEMF) measurements for open terminals of the PMSM at rotor speeds of $n = 100, 200, \dots, 1000$ rpm, whose values are evaluated for $n_{\psi,\varphi} = 72$ rotor positions $\varphi_\psi = 1.25, 2.5, \dots, 90^\circ$.
- current measurements at $n_{\psi,\varphi} = 72$ different standstill rotor positions $\varphi_\psi = 1.25, 2.5, \dots, 90^\circ$ for a sinusoidal desired current trajectory with an amplitude of i_n and a constant period of $T = 25$ ms applied separately in the direct d and quadrature q axis direction, cf. Fig. 2.1.

Utilizing these measurements, the calibration is obtained by solving the constrained optimization problem

$$\min_{\mathbf{x}_c, \mathbf{u}_{tg,h}, \mathbf{u}_{tg,jk}} \frac{1}{2} (J_\tau + J_\psi + J_R) \quad (3.8a)$$

$$\text{s.t. eq. (3.13a)} \quad l = 1, \dots, n_\tau \quad (3.8b)$$

$$\text{eq. (3.13b)} \quad j = 1, \dots, n_{\psi,\varphi}, \quad k = 1, \dots, n_{\psi,i} . \quad (3.8c)$$

With the first term of the cost function

$$J_\tau = q_\tau \sum_{l=1}^{n_\tau} \left(\tau_l^m - \tau_l(\varphi_l^m, \mathbf{i}_{c,r,l}^m, \mathbf{u}_{tg,l}) \right)^2 \quad (3.9)$$

the torque error is minimized, where measured variables are indicated by the superscript m . The second term

$$J_\psi = \sum_{j=1}^{n_{\psi,\varphi}} \sum_{k=1}^{n_{\psi,i}} \mathbf{e}_{\psi,jk}(\varphi_{jk}^m, \mathbf{i}_{c,r,k}^m, \mathbf{u}_{tg,jk}) \mathbf{I}_{2 \times 2} \mathbf{e}_{\psi,jk}^T(\varphi_{jk}^m, \mathbf{i}_{c,r,k}^m, \mathbf{u}_{tg,jk}) \quad (3.10)$$

weights the flux linkage errors $\mathbf{e}_{\psi,jk} = \boldsymbol{\psi}_{c,r,jk}^m - \boldsymbol{\psi}_{c,r,jk}$. Note that the flux linkages can not be measured directly. Instead, the first row of (2.31b) is rearranged to

$$\boldsymbol{\psi}_{c,r,jk}^m = \mathbf{H}_r^l \bar{\mathbf{D}}_c \mathcal{G}_c(\varphi_{jk}^m, \mathbf{i}_{c,r,jk}^m, \mathbf{u}_{tg,jk}) \left(\bar{\mathbf{D}}_c^T \mathbf{H}_r^r \mathbf{i}_{c,r,jk}^m + \mathbf{D}_g^T \mathbf{u}_{tg,jk} + \mathbf{D}_m^T \mathbf{u}_{ms} \right) \quad (3.11)$$

with \mathbf{H}_r^l and \mathbf{H}_r^r derived in Section 2.4.3 and evaluated with the measured signals of the rotor position and currents. The last term of (3.8a)

$$J_R = q_\psi \max\{0, -\eta\}^2 + \sum_{p=0}^{n_g} \left(q_\sigma \max\{0, e_{\sigma,p}\}^2 + q_\Delta \max\{0, e_{\Delta\varphi,p}\}^2 \right) \quad (3.12)$$

is introduced as a regularization term. Here, the first part penalizes negative values of the scaling factor η , to ensure a positive value of the stator leakage permeance. The second part ensures a reasonable shape of the air gap permeances through barrier functions, which penalize the widths $e_{\sigma,p} = \sigma_{min} - \sigma_p$ and position distances $e_{\Delta\varphi,p} = \Delta\varphi_{min} - \Delta\varphi_p$ of the Gaussian functions smaller than σ_{min} and $\Delta\varphi_{min}$, respectively. The scalar positive weighting factors q_τ , q_ψ , q_σ , and q_Δ are used to weight the importance of the different cost functions parts of (3.8a).

The optimization variables consist of the desired calibration variables \mathbf{x}_c , cf. (3.7), as independent part and the mmfs of the permeances $\mathbf{u}_{tg,l}$, $\mathbf{u}_{tg,jk}$ as dependent optimization variables. The latter variables are calculated by the model constraints, cf. (2.31b)

$$\begin{aligned} \mathbf{D}_g \mathcal{G}_c(\varphi_l^m, \mathbf{x}_c) \left(\bar{\mathbf{D}}_c^T \mathbf{H}_r^r \mathbf{i}_{c,r,l}^m + \mathbf{D}_m^T \mathbf{u}_m \right) \\ + \left(\mathcal{G}_t(\varphi_l^m, \mathbf{x}_c) + \mathbf{D}_g \mathcal{G}_c(\varphi_l^m, \mathbf{x}_c) \mathbf{D}_g^T \right) \mathbf{u}_{tg,l} = \mathbf{0} \end{aligned} \quad (3.13a)$$

$$\begin{aligned} \mathbf{D}_g \mathcal{G}_c(\varphi_{jk}^m, \mathbf{x}_c) \left(\bar{\mathbf{D}}_c^T \mathbf{H}_r^r \mathbf{i}_{c,r,k}^m + \mathbf{D}_m^T \mathbf{u}_m \right) \\ + \left(\mathcal{G}_t(\varphi_{jk}^m, \mathbf{x}_c) + \mathbf{D}_g \mathcal{G}_c(\varphi_{jk}^m, \mathbf{x}_c) \mathbf{D}_g^T \right) \mathbf{u}_{tg,jk} = \mathbf{0} . \end{aligned} \quad (3.13b)$$

The solution of the optimization problem by using the quasi-newton solver of MATLAB requires approximately 15 min on a computer with 3.7 GHz Intel Core i7.

3.3 Model validation

The calibrated model is validated using measurements on a test stand, cf. Section 3.1, utilizing the multiphase VSI, cf. Section 3.1.1. Several experiments are performed showing the model validation for static and dynamic behavior in the HC case and for a single OC fault case. Since the radial forces cannot be measured at the test stand and the torque sensor signal is disturbed at higher rotor speeds due to mechanical vibrations of the test stand, these values are obtained by (2.11) and (2.13), which require the currents, the rotor position and the mmf of the tree permeances as variable inputs. Since the currents \mathbf{i}_c^m and the rotor position φ^m are measured, the mmf of the tree permeances are calculated based on the quasi-static magnetic model, which is given by the rearranged second row of the algebraic system of equations (2.23b) by

$$\mathbf{D}_g \mathcal{G}_c(\varphi^m) \left(\bar{\mathbf{D}}_c^T \mathbf{i}_c^m + \mathbf{D}_m^T \mathbf{u}_{ms} \right) + \left(\mathcal{G}_t(\varphi^m) + \mathbf{D}_g \mathcal{G}_c(\varphi^m) \mathbf{D}_g^T \right) \mathbf{u}_{tg} = \mathbf{0} . \quad (3.14)$$

This equation is solved at each sample time step by a quasi-newton solver.

3 Model calibration and validation

The essential quantity is the torque accuracy, which is validated in the first experiment by slow rotations ($n = 4$ rpm) of the PMSM in the 4×3 configuration, cf. Section 2.4.1, at different constant currents $i_{c,1,4,7,10} = i^d$ and $i_{c,2,3,5,6,8,9,11,12} = -0.5i^d$. A simple current controller is used to track the constant desired currents. Figure 3.5a shows the rated torque comparison of the measurements (colored lines) and evaluated model results (black dashed lines). The results show a very high torque accuracy even for up to twice the nominal current range. In addition, the cogging torque for zero currents is visible. The second experiment is performed regarding the BEMF of the PMSM. In Fig. 3.5b, the measured and evaluated BEMF is drawn for the first three coils of the motor. This measurement is performed for open terminals at a rotational speed of $n = 720$ rpm. The major non-fundamental BEMF harmonic components are the fifth and seventh harmonics. Again, an excellent model accuracy is achieved.

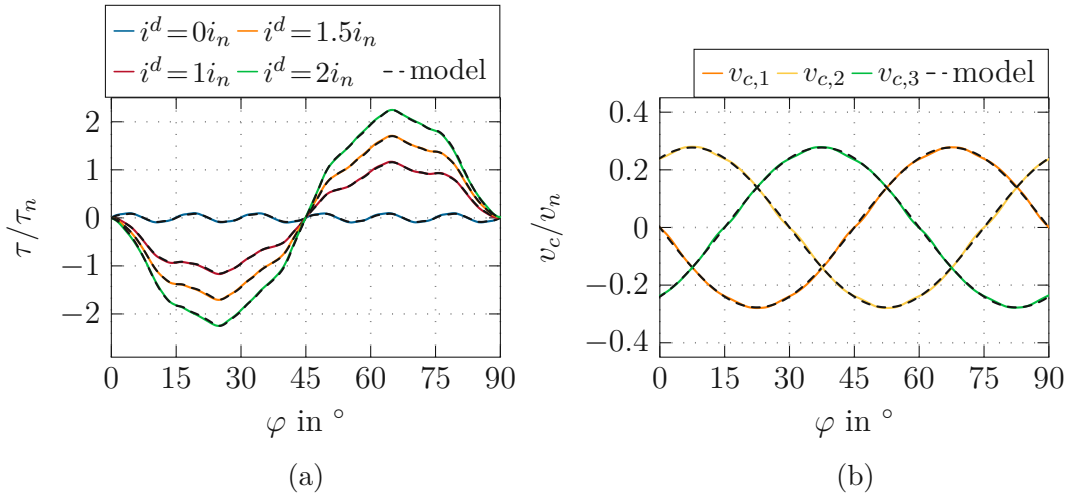


Figure 3.5: MEC model validation for the HC case in the 4×3 configuration: a) normalized torque with constant currents $i_{c,1,4,7,10} = i^d$ and $i_{c,2,3,5,6,8,9,11,12} = -0.5i^d$ for $n = 4$ rpm, b) BEMF at $n = 720$ rpm for open terminals.

The third experiment is performed to analyze the inductance behavior, which is mainly influenced by the stator leakage permeances. A sinusoidal desired current with an amplitude of twice the nominal current and a frequency of 100 Hz is specified in the direct d and quadrature q axis for the dynamic model validation. Thereby, the rotor is fixed at a constant rotor position. For this model evaluation, the dynamic model of (2.23a) is fed by the coil voltages $\mathbf{v}_c = \mathbf{V}_{dc}^m (\boldsymbol{\delta}^m - 0.5\mathbf{1})$, with the measured duty cycles and the measured dc-link voltages rearranged by (3.1). Figure 3.6 shows the rated current comparison between the currents obtained by the model and the measured ones at a constant rotor position $\varphi = 0^\circ$ for the first three coil currents since the other coil currents are similar. The calibrated model

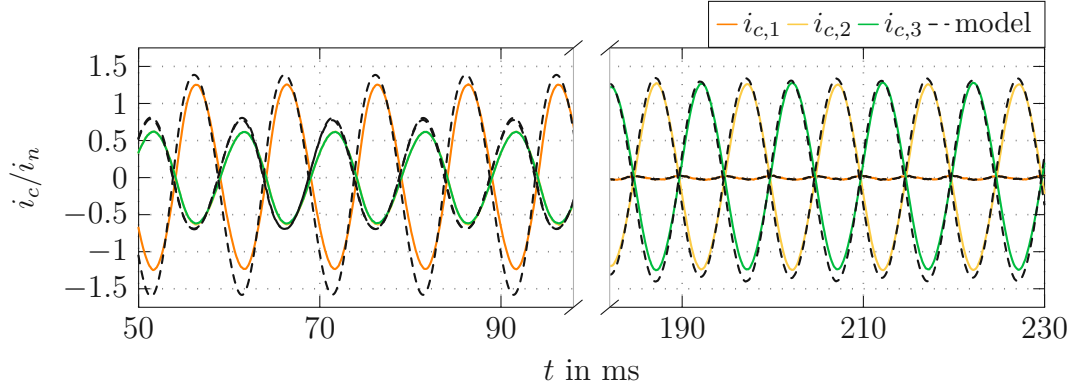


Figure 3.6: MEC model validation for the HC case in the 4×3 configuration: dynamic current response at fixed rotor position $\varphi = 0^\circ$ for the first three coils.

exhibits good accuracy in terms of the phase and amplitude. The minor amplitude deviations of the model mainly result from the non-ideal VSI behavior, which is not included in the dynamic model.

The last experiments investigate the model accuracy for constant torques in the HC case and for a single OC fault of coil 1 in the 1×12 configuration to show the model accuracy additionally in the event of an OC fault case without fault mitigation strategies. The results of the approximation of the optimized currents for the HC case $i_c^{d,HC}$, that will be derived in Chapter 4, are used for this purpose. In the OC fault case, the current in the faulty coil 1 is zero $i_{c,1} = 0$. Therefore, it is not possible to enforce the same currents for the remaining coils as in the HC case since Kirchhoff's current law must hold for the remaining 11 coil currents, i.e. $\sum_{k=2}^{12} i_{c,k} = 0$. To get physically meaningful desired currents, also for the OC fault case, the sum of the desired coil currents of coil j is subtracted from the desired currents,

$$i_{c,j}^{d,OC1} = i_{c,j}^{d,HC} - \frac{1}{11} \sum_{k=2}^{12} i_{c,k}^{d,HC}, \quad (3.15)$$

with $j = 2, \dots, 12$ and $i_{c,1}^{d,OC1} = 0$.

Fig. 3.7a shows the comparison of torque measurements with the MEC model for the HC case and the case of an OC fault of coil 1 at a constant rotational speed of $n = 20$ rpm. It can be seen that the measured and modeled torque accurately match, and thus, a high model accuracy can be achieved for both the HC and the OC fault case. Furthermore, utilizing nominal currents for the OC fault yields large torque deviations with an error up to 25%.

The measured currents for the HC case of coil 1 to 3 for the nominal torque are depicted in the upper plot of Fig. 3.7b (the currents of the other coils have a similar

3 Model calibration and validation

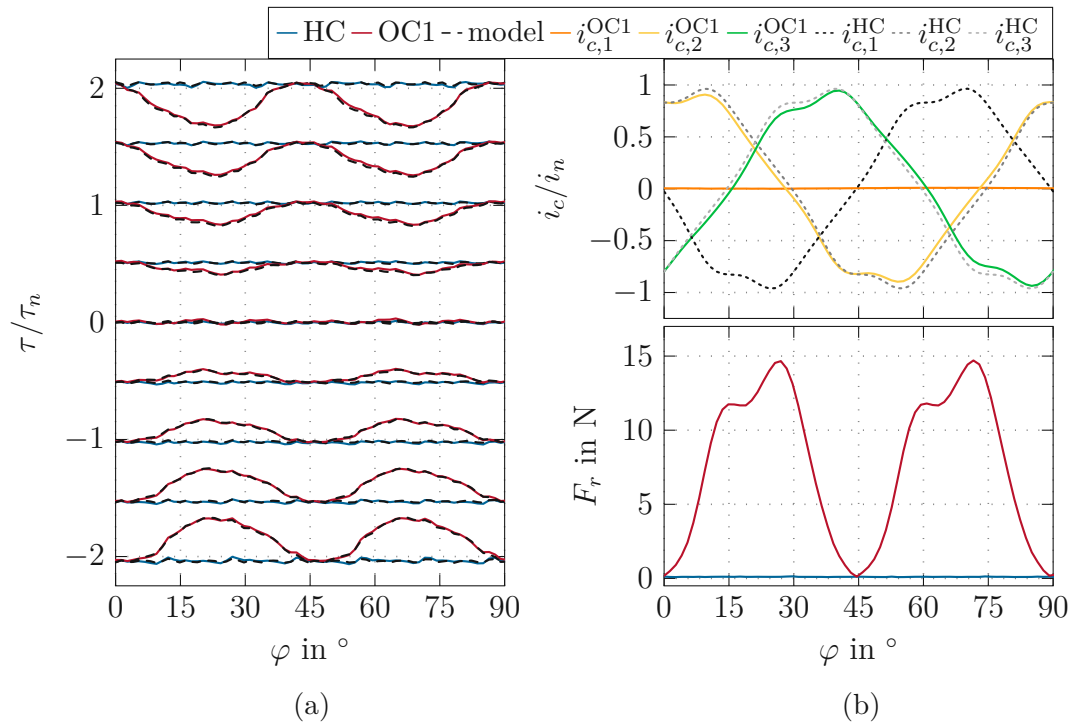


Figure 3.7: MEC model validation for constant torques in the HC case and under a single OC fault of coil 1 without fault mitigation for the 1×12 configuration at $n = 20$ rpm. a) torques, b) corresponding currents and radial forces for the nominal torque $\tau = \tau_n$ case.

pattern). It can be seen that rather strong deviations from sinusoidal currents are required for the studied PMSM in order to achieve an approximately constant torque. This is due to the specific design of the PMSM, which also features rather large cogging torques, see the detailed analysis in [36]. Finally, the radial force is depicted in the lower plot of Fig. 3.7b. As expected, the radial force is zero for the HC case. However, utilizing the unsuitable coil currents of the HC case for the OC fault yields rather large radial forces. This explains the motivation of this work to mitigate the influence of OC faults on both the torque and the radial force.

In conclusion, this model validation confirms a good agreement between the measurements and the calibrated MEC model. The calibrated MEC model accurately covers the main nonlinear effects of cogging torque, non-fundamental BEMF, and magnetic saturation. Furthermore, the PMSM behavior is accurately predicted both for the HC and the OC fault case. Thus, this model serves as a solid basis for the model-based calculation of optimal currents in the next section.

4

Current optimization with radial force compensation

Parts of this chapter were published in similar form in the author's previous publications [1, 2].

In this chapter, a current optimization method with radial force compensation for multiple open-circuit (OC) fault cases is proposed and derived based on the calibrated nonlinear magnetic equivalent circuit (MEC) model of the previous chapters. Its generalized formulation is suitable for several electrical coil interconnections and OC fault cases and applied to multiple OC fault cases in the 1×12 and the 4×3 configuration. The resulting optimized currents will be utilized as desired currents for the current controller in Chapter 5. With the proposed current optimization strategy, the increased number of degrees of freedom (DOFs) of the multiphase permanent magnet synchronous machine (PMSM) is systematically used to minimize the radial forces in the event of OC fault cases in addition to the usual control goals such as torque tracking error and power losses. Real-time capability is achieved by approximating the optimized currents using Fourier series approximation, which significantly reduces the computing effort and memory requirements.

4.1 Current optimization problem formulation

The current optimization is developed to achieve the following three goals:

1. The torque tracking error $e_\tau = \tau^d - \tau$ is minimized to follow the desired torque τ^d accurately, both for the healthy-circuit (HC) and the multiple OC

4 Current optimization with radial force compensation

fault case. This, of course, includes the compensation of the torque ripples due to cogging.

2. The PMSM's efficiency is maximized by minimizing the ohmic power losses, i.e., by reducing the sum of the squared coil currents.
3. The compensation of radial forces within the PMSM that occur in OC fault cases.

Radial force compensation can also be helpful in HC cases if the motor design entails known but undesired radial forces, e.g., due to rotor eccentricity effects, cf. Section 2.2.3.

For linear PMSMs, an analytical solution of the well-known maximum torque per ampere (MTPA) approach in the dq0-reference frame exists [80]. However, this optimization task is more complex with the given nonlinear and non-sinusoidal behavior of the investigated PMSM. The optimization problem is formulated as

$$\min_{\mathbf{x}_o} \frac{1}{2} \left(w_\tau (\tau^d - \tau)^2 + w_c \mathbf{i}_{c,r}^T \mathbf{i}_{c,r} + w_F F_r^2 \right) \quad (4.1a)$$

$$\text{s.t. } \mathbf{D}_g \mathcal{G}_c (\bar{\mathbf{D}}_c^T \mathbf{H}_r^r \mathbf{i}_{c,r} + \mathbf{D}_m^T \mathbf{u}_{tm}) + (\mathcal{G}_t + \mathbf{D}_g \mathcal{G}_c \mathbf{D}_g^T) \mathbf{u}_{tg} = \mathbf{0} , \quad (4.1b)$$

where (4.1b) describes the quasi-static model of the PMSM, and the radial force is calculated according to (2.13). By expressing the coil currents by the reduced coil currents $\mathbf{i}_c = \mathbf{H}_r^r \mathbf{i}_{c,r}$ and by adapting \mathbf{H}_r^r according to the considered electrical coil interconnection and case, arbitrary multiple OC faults can be considered, cf. Section 2.3 and Section 2.4. The optimization variables

$$\mathbf{x}_o = \begin{bmatrix} \mathbf{i}_{c,r} \\ \mathbf{u}_{tg} \end{bmatrix} \quad (4.2)$$

consist of the reduced coil currents $\mathbf{i}_{c,r}$ and the magnetomotive force (mmf) of the tree permeances \mathbf{u}_{tg} . The positive weighting factors w_τ , w_c , and w_F for torque tracking error, power losses, and radial force compensation are adjusted to scale the three goals. Obviously, $w_F = 0$ switches off the radial force compensation, which is meaningful to simplify the optimization in the HC case, where $F_r = 0$ is automatically fulfilled. It is important to mention that in [37], a similar optimization problem was formulated, however, without taking into account the radial forces. Furthermore, the goal $\tau^d - \tau = 0$ was formulated as an equality constraint in the optimization problem. Using the optimization problem (4.1) is beneficial since it allows to specifically weight the different goals and provides smoother current trajectories. This comes at the expense of torque tracking errors, which, however, can be kept small by a suitable choice of the weights.

The optimization problem (4.1) is solved for each rotor position and a desired torque individually. The solution speed is enhanced by using the previous optimization results as initial guess. The dimension of the optimization problem is

given by the constant size of 28 mmf of the tree permeances and a variable size of up to $n_c - 1$ coil currents, which depend on the considered electrical interconnection and the number of OC faults, cf. Section 2.4. The optimization problem (4.1) is formulated within the CasADi framework [89] and solved with the interior point optimizer IPOPT [90]. The computation time required for one single optimization point is about 10 ms (achieved with MATLAB 2022b on a computer with 3.7 GHz Intel Core i7 and 24 GB RAM), far from the real-time capability for a typical sampling (pulse width modulation) frequency of 10 kHz. Therefore, the optimization problem is solved offline, and an approach to approximate the optimized current patterns will be presented after the optimization results in the following sections.

4.2 Current optimization results

This section presents the results of the current optimization and discusses the selection of the three weighting factors for the optimization problem in (4.1).

4.2.1 Cases without radial force compensation

The optimization results of the HC case for constant and dynamic desired torques are discussed in this section. Here, the radial force compensation is disabled by $w_F = 0$. In Fig. 4.1, the results for the nominal desired torque in the 4×3 configuration with the rated torque on the left and the corresponding optimized currents on the right plot are presented. Thereby, only the currents of the first three coils are shown as all other coil currents are similar due to the geometry. The weights

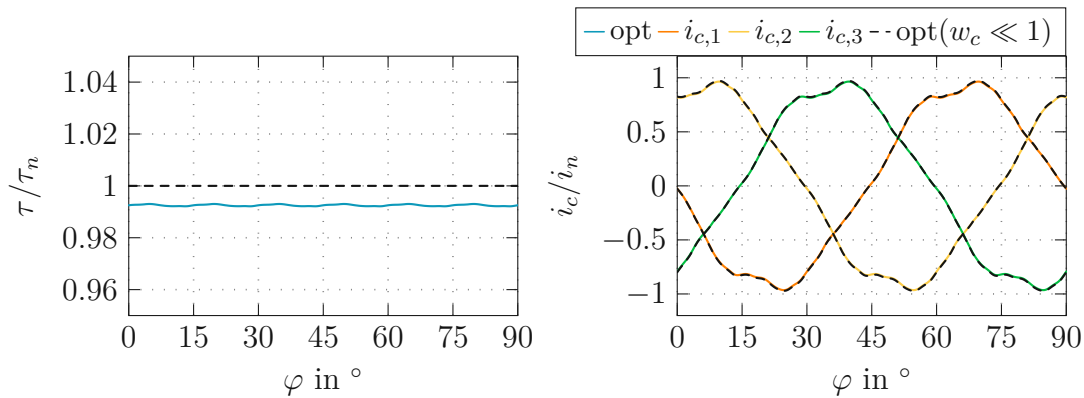


Figure 4.1: Results of the optimal torque and currents over the rotor position for the HC case in the 4×3 configuration at the nominal constant desired torque. Comparison of torque tracking error and power loss weighting.

4 Current optimization with radial force compensation

for torque tracking and power losses are chosen as $w_\tau = 280$ and $w_c = 0.1$ (solid lines), which is a good compromise between torque tracking accuracy and power losses, particularly if OC faults are considered. It is further important to mention that the optimal current shape exhibits a significant non-fundamental wave behavior, which has already been observed and discussed in Chapter 3. A smaller weighting of the power losses w_c (dashed lines in Fig. 4.1) leads to a higher torque tracking accuracy, which comes close to considering the torque tracking error as an optimization constraint. As the visible difference in the current waveforms in the HC case for both weighting factor choices is very small, a smaller weighting of the power losses would be better at first glance. However, this results in larger losses, particularly for the OC fault cases, and renders the current patterns less smooth. This will cause problems for the approximation of the current patterns and the tracking within the current control loop. Thus, the smaller weighting of the power losses does not lead to an advantage for all considered cases. The specific values of the weighting factors $w_\tau = 280$ and $w_c = 0.1$ are selected to keep the torque error below 1% of the nominal torque τ_n . Besides, this torque tracking error lies below the achievable model accuracy for typical variations of the motors in series production.

In a second optimization scenario, the dynamic torque tracking in the HC case and a single OC fault case of coil 1 is studied for the 1×12 configuration. To do so, a linear chirp function of the desired torque τ^d with respect to the rotor angle φ and an amplitude of twice the nominal torque is selected. The desired torque trajectory is discretized in $N_\varphi = 1000$ equally spaced rotor position steps for one mechanical revolution. Figure 4.2 shows the results of the torque, the torque error, and the currents in the HC and in the OC fault case of coil 1. In the upper left plot, the desired torque trajectory and the resulting torques for both cases are depicted. The torque error shown in the lower left plot is small and in the identical range for both cases. Note that this desired torque pattern changes rapidly in amplitude and is used to demonstrate the effectiveness of the current optimization method. In the upper right plot of Fig. 4.2, the shape of the optimal currents for the HC and the OC fault case are compared for coils 12, 1, and 2. These currents are of specific interest since the OC fault occurs in coil 1 and coils 12 and 2 are the neighboring coils. The currents of the coils opposed to the fault 6, 7, and 8 are depicted in the lower right plot. Taking first a look at the HC case (dashed lines), it is evident that identical current patterns are given for the coils that are rotated by 90° at the stator (e.g., coils 1, 4, 7, and 10). This result is expected and directly related to the symmetry of the motor design. In the OC fault case of the first coil, the correspondent current $i_{c,1}$ equals zero. Interestingly, there are only minor changes in the optimal currents for the adjacent coils 12 and 2. The same holds true also for the currents of coils 6 and 8. In contrast, the

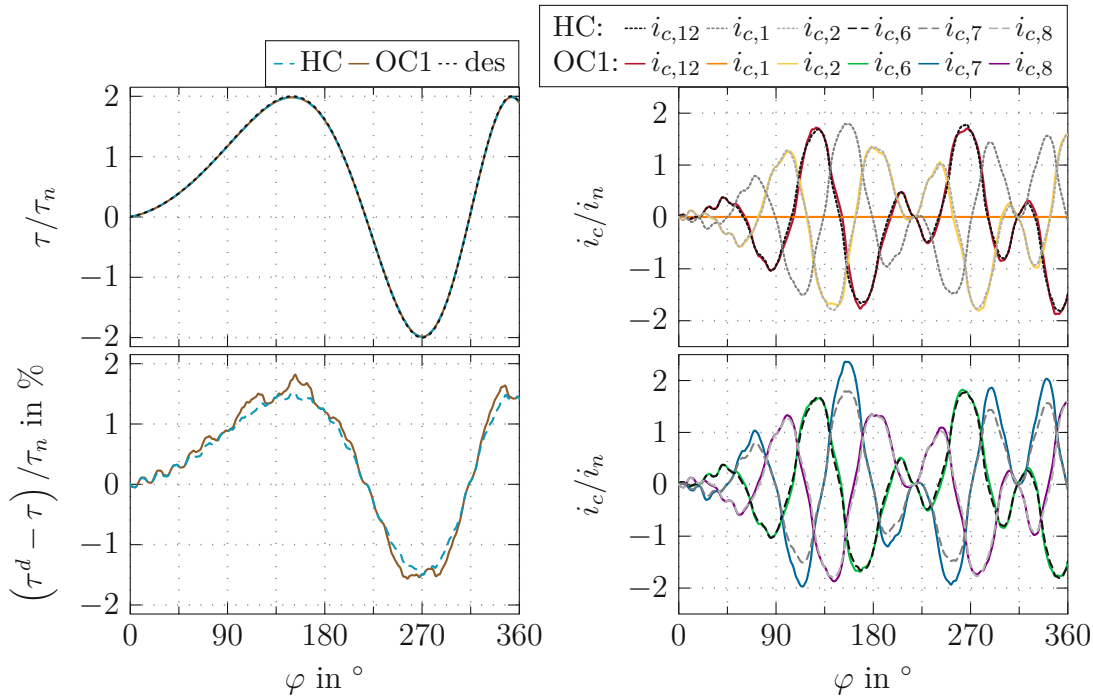


Figure 4.2: Optimization results without radial force compensation for the HC case and the OC fault case of coil 1 in the 1×12 configuration.

current of the opposite coil $i_{c,7}$ is significantly changed (increased), which is also the case for coil 4 and 10 as they have the same current pattern as coil 7. These coils have to compensate for the OC fault of coil 1 since they are placed in the same orientation with respect to the permanent magnet field.

4.2.2 Open-circuit fault cases with radial force compensation

Neglecting the radial force in the optimization yields a high torque accuracy but also high radial forces in the PMSM. Thus, in the next scenario, the influence of w_F , see (4.1), on the radial force compensation is studied in the OC fault case of coil 1 in Fig. 4.3 in the 1×12 configuration. Here, a constant desired torque $\tau^d = 2\tau_n$ is chosen. Figure 4.3 shows the results for three weighting factors w_F , which correspond to no radial force compensation $w_F = 0$, strong radial force compensation $w_F = 0.1$ and a medium radial force compensation $w_F = 0.001$. The upper right plot shows the radial forces over one electrical revolution of 90° . As expected, the pattern of the radial force is repeated twice due to the missing contribution of coil 1. It is also seen that the proposed optimal currents are able to significantly reduce the amplitude of the radial force by a factor of more than

4 Current optimization with radial force compensation

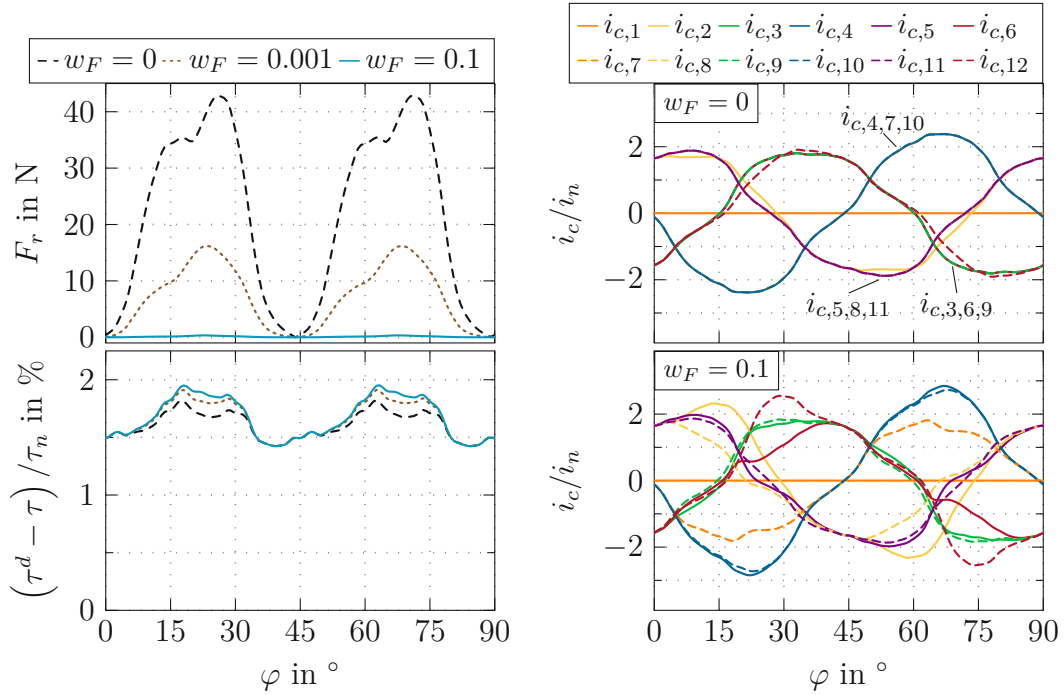


Figure 4.3: Comparison of radial forces, torque errors, and current patterns for different radial force weighting factors w_F in the OC fault case of coil 1 in the 1×12 configuration.

500 for $w_F = 0.1$. This, of course, has adverse effects on the torque error, depicted on the lower right plot, which is slightly increasing. However, this increase of the torque error remains considerably low and thus will be acceptable for real operation. A significantly larger impact of radial force compensation occurs in the required currents, as shown in the plots on the right. Here, the currents for $w_F = 0$ (no radial force compensation) and $w_F = 0.1$ are depicted in the upper and lower plot, respectively. It is evident that in order to compensate for radial forces, significantly higher currents (the maximum current values increase by a factor of approximately 1.6) are required. Additionally, and in contrast to the case without radial force compensation, no symmetry is recognizable in the current patterns.

Based on these results, the question of the correlation between the degree of radial force compensation and the power losses

$$P_l = \mathbf{i}_c^T (\mathbf{R}_c + \mathbf{R}^{\text{VSI}}) \mathbf{i}_c \quad (4.3)$$

arises. This relation is depicted in Fig. 4.4 for different radial force weighting factors w_F , where the power losses P_l are averaged over one full rotation of the rotor

4.3 Approximation for real-time application

and related to the power losses of the motor without radial force compensation $P_{l,0} = P_l(w_F = 0)$. It is interesting to see that the significant increase of the current

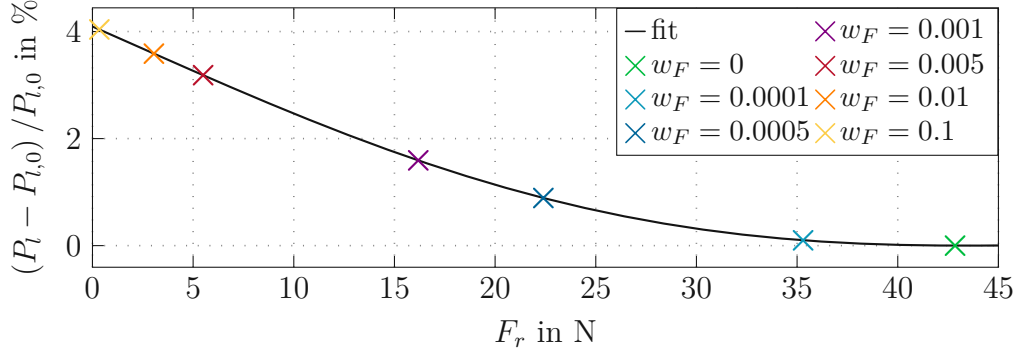


Figure 4.4: Rated average power losses P_l for different weighting factors w_F as a function of the maximum values of radial forces in the OC fault case of coil 1 for the 1×12 configuration.

amplitude of specific coils only brings about a very minor increase of the overall power losses. Thus, strong radial force compensation is possible if the maximum currents of the inverter and the coils are not exceeded. Figure 4.3 shows that it is easily possible to control the degree of radial force compensation by means of w_F . Therefore, it is possible to choose the degree of radial force compensation according to the motor's operating point.

4.3 Approximation for real-time application

A real-time solution for the optimized current patterns is given in this section. Since the required optimization time is far from real-time capability, cf. Section 4.1, the solution of the current optimization is approximated. Simply saving the offline solutions of the current optimization obtained by (4.1) would result in a large number of current patterns, which require significant memory on a real-time system. Therefore, in this section, a Fourier series approximation of the optimal current patterns is proposed to reduce the memory requirements. The approximated currents are given by

$$\mathbf{i}_c^d(\varphi, \tau^d) = \sum_{k=1}^{n_h} \left(\mathbf{c}_k(\tau^d) \cos(h_k n_p \varphi) + \mathbf{s}_k(\tau^d) \sin(h_k n_p \varphi) \right), \quad (4.4)$$

with the desired torque-dependent cosine and sine coefficients vectors $\mathbf{c}_k(\tau^d)$ and $\mathbf{s}_k(\tau^d)$, respectively. The relevant harmonics are defined in the harmonic order

4 Current optimization with radial force compensation


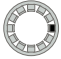



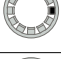
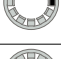
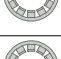
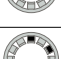
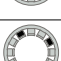
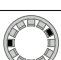
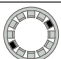




vector \mathbf{h} , and n_h indicates its length. The main advantage of this approximation is that only the coefficient vectors \mathbf{c}_k and \mathbf{s}_k are needed to define the optimal current reference signals. They can be efficiently stored in lookup tables (LUT), minimizing computation time and memory space. As briefly discussed, the optimal current patterns differ for different scenarios, ranging from HC to single OC, double OC, and triple OC fault cases for the 1×12 and 4×3 configuration.

The number of physically different OC fault cases is given by the binomial coefficients with the number of coils n_c over the number of OC faults n_{OC} , resulting in 12, 66, and 220 different cases for the single, double, and triple OC fault case, respectively. However, due to the rotor symmetry, only the relative position of the faulty coils to each other is relevant for the different fault scenarios, which reduces the number of relevant fault cases. In particular, double OC fault cases in one three-phase system of the 4×3 configuration lead to an uncontrollable three-phase system due to Kirchhoff's current law. Therefore, this type of fault case is similar to a triple OC fault case. Additionally, for one three-phase system in the 4×3 configuration, only the distinction between the central coil and edge coils has to be considered due to the rotor symmetry, which further reduces the different fault cases. The disconnection of one three-phase system in the 4×3 configuration is considered by the triple OC fault case of adjacent coils. Further triple OC fault cases are not covered in this work, although all presented methods are generalized and suitable for the description of more than triple OC fault cases. The resulting number of unique fault cases is listed in Tab. 4.1.

To generate the required LUT, the current optimization problem of (4.1) is solved for all unique fault scenarios. For each scenario, torque demands of $\tau^d/\tau_n = -3, -2.75, \dots, 3$ for the rotor position values $\varphi = 1^\circ k/n_p$, $k = 0, 1, \dots, 360$ are applied. The weighting factors are selected so that the torque tracking error is kept below 1% of the nominal torque and that a good suppression of radial forces is obtained, see the discussion in Section 4.2. The weighting factors $w_\tau = 280$, $w_c = 0.1$, and $w_F = 0.002$ are suitable to achieve these goals. A fast fourier transform (FFT) analysis is performed on the optimal current patterns to identify the relevant harmonics for the approximation. As expected, the relevant harmonic orders mainly depend on the considered fault cases, and considering higher harmonics reduces the current approximation error. However, the current approximation error is not directly transferable to the resulting torque errors and radial forces, which are essential for the performance of the PMSM. Therefore, further analysis is performed by evaluating the influence of the chosen harmonic orders on the following errors

4.3 Approximation for real-time application

Table 4.1: Unique fault cases for HC, single OC fault, double OC fault, and triple adjacent OC fault cases in the 1×12 and the 4×3 configuration. The table also contains the resulting DOFs (independent currents) and the occurrence of unbalanced radial forces.

Case	1×12		4×3		Stator coils	Unbalanced radial forces
	Faulty coils	DOFs	Faulty coils	DOFs		
HC	-	11	-	8		no
Single OC	1	10	1	7		yes
			2	7		yes
Double OC	1,2	9				yes
	1,3	9				yes
	1,4	9	1,4	6		yes
	1,5	9	1,5	6		yes
	1,6	9	1,6	6		yes
	1,7	9	1,7	6		no
			2,4	6		yes
			2,5	6		yes
			2,7	6		yes
			2,8	6		no
			3,4	6		yes
			3,7	6		yes
Triple adjacent OC	1,2,3	8	1,2,3	6		yes

4 Current optimization with radial force compensation

for the torque and radial forces

$$e_\tau = \sqrt{\frac{1}{n_\varphi n_\tau} \sum_{j=1}^{n_\tau} \sum_{l=1}^{n_\varphi} \left(\tau_j^d - \tau(\varphi_l, \mathbf{i}_c^d(\tau_j^d, \varphi_l)) \right)^2} \quad (4.5a)$$

$$e_{F_r} = \sqrt{\frac{1}{n_\varphi n_\tau} \sum_{j=1}^{n_\tau} \sum_{l=1}^{n_\varphi} \left(\sum_{k=1}^{n_h} F_r(\varphi_l, \mathbf{i}_c^d(\tau_j^d, \varphi_l)) \right)^2}. \quad (4.5b)$$

These errors are calculated for different current approximations \mathbf{i}_c^d , defined by the chosen vector of harmonics \mathbf{h} . The results for the current approximation utilizing different harmonic orders for HC, single, double, and triple adjacent OC fault cases with radial force compensation are visualized in Fig. 4.5 for the 4×3 and in Fig. 4.6 for the 1×12 configuration.

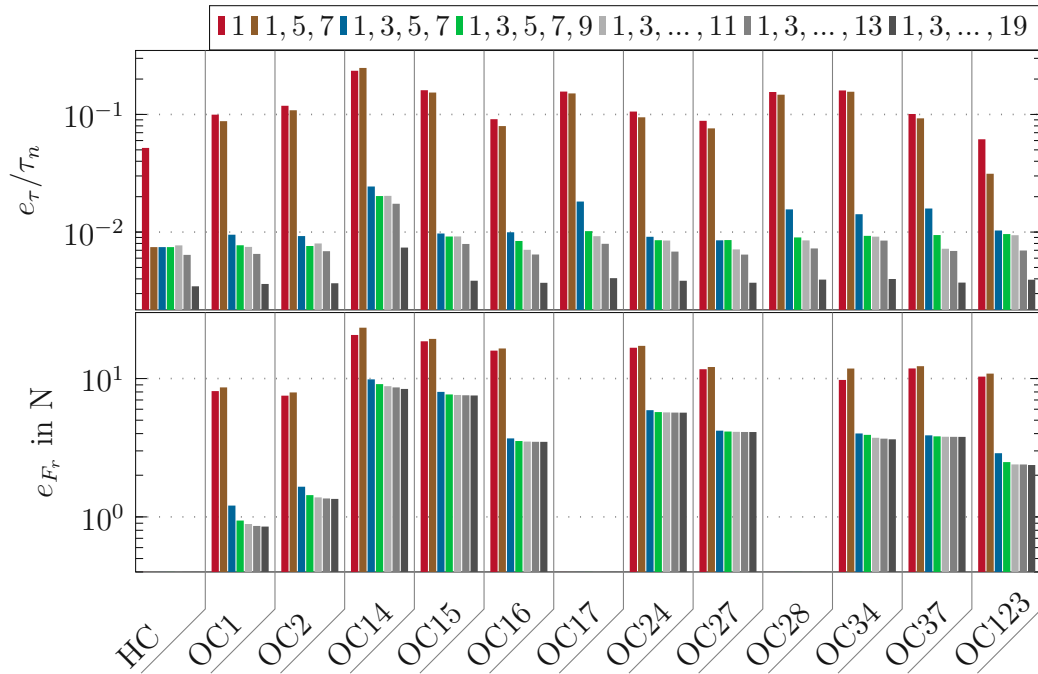


Figure 4.5: Simulated approximation error for the torque and radial forces of the 4×3 configuration as a function of the harmonic orders.

Within these plots, the digits in the label OC relate to the faulty coils. E.g., OC17 describes an open circuit fault of coils 1 and 7. Furthermore, the numbers in the legend give the harmonics considered in \mathbf{h} for the optimal current approximation. The results show that considering only the fundamental wave leads to significant errors in all cases, even for the HC case. The additional consideration of the fifth and seventh harmonic significantly reduces the torque error for the HC case.

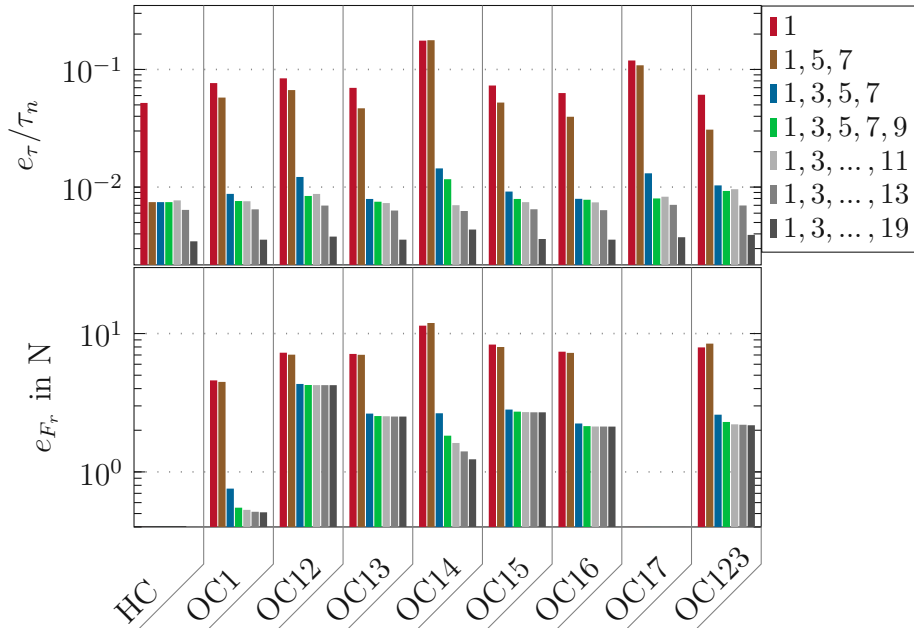


Figure 4.6: Simulated approximation error for the torque and radial forces of the 1×12 configuration as a function of the harmonic orders.

However, it improves neither the torque nor the radial force compensation in OC fault cases. Here, taking into account the third harmonics is essential to improve accuracy. Adding higher harmonics yields a slight increase in torque and radial force accuracy, and for harmonics up to the 19th, no further improvement of torque or radial force accuracy can be achieved. Similar conclusions are also valid for the 1×12 configuration. Considering these results, the harmonic orders $\mathbf{h}^{\text{HC}} = [1, 5, 7]$ for the HC case and $\mathbf{h}^{\text{OC}} = [1, 3, 5, 7, 9]$ for all OC cases constitute a good compromise between approximation accuracy and the number of required harmonics.

4.3.1 Approximation results

Given the specified required current harmonics, the current approximation results are analyzed in the following. In OC fault cases, the performance deterioration decreases the torque and leads to torque oscillations when the HC current patterns are maintained, cf. Fig. 3.7. Now, when applying the current patterns optimized for the OC fault cases, either the torque can be maintained if higher current amplitudes are available or if the current amplitudes are the limiting factor, the available torque is reduced [29]. The latter scenario is used in the following to give an overview of the challenges occurring in different OC fault cases when the

4 Current optimization with radial force compensation

current amplitudes are limited to the nominal current. The achieved torque values under this condition are compared in Fig. 4.7 for cases with ($w_F \neq 0$) and without ($w_F = 0$) radial force compensation in both the 4×3 and the 1×12 configuration.

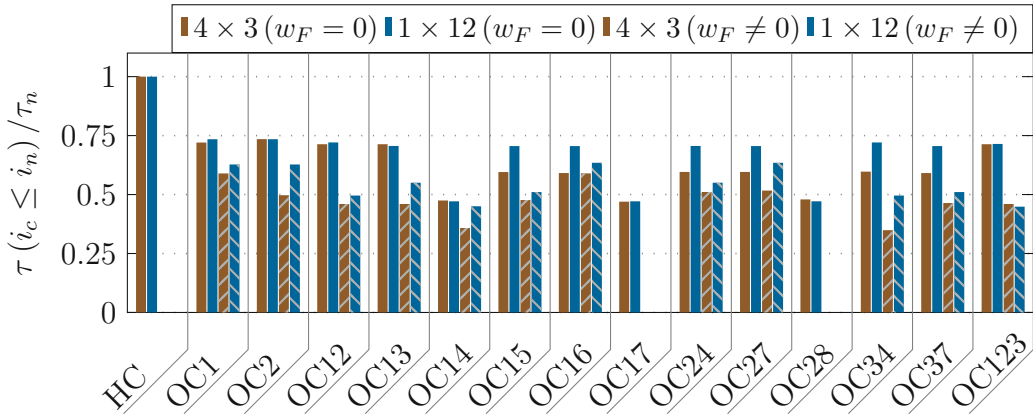


Figure 4.7: Comparison of simulation results for torque reduction at equal current amplitudes with and without radial force compensation in the 4×3 and the 1×12 configuration.

In OC fault cases, the resulting torque is decreased by a minimum of over 25% compared to the HC case for both configurations. In single OC fault cases (OC1 and OC2), the reduced torques are similar without radial force compensation but favor the 1×12 configuration when considering radial force compensation. The largest torque reductions are visible in double OC fault cases when the affected coils are shifted by multiples of 90° (coils 1 and 4, coils 1 and 7, coils 2 and 8). Similar or higher torques are achievable for all double and the triple OC fault cases in the 1×12 configuration. The lowest achievable torques result in the double OC fault cases of coils 1 and 4, and coils 3 and 4 in the 4×3 configuration. Therefore, these cases are analyzed in more detail.

In Fig. 4.8a, the approximation results for the 4×3 configuration in the OC fault case of coils 1 and 4 are studied since this case shows the largest approximation error, see Fig. 4.5. In addition to the case with radial force compensation, the case without radial force compensation (i.e., for $w_F = 0$) is shown. The plot of the resulting torques gives similar errors in the range of approximately 2% of the nominal torque. This slightly increased error compared to the optimal solution in Fig. 4.1 can be attributed to the current pattern approximation. Thus, a significant reduction of the radial forces can be achieved without a relevant influence on the torque tracking accuracy. The corresponding current patterns for the case without and with radial force compensation are depicted on the top and lower right side of Fig. 4.8a. It is visible that the uncompensated radial force case's current patterns

4.3 Approximation for real-time application

are almost similar for coils shifted by 90° . The current amplitudes of coils 7 and 10 are higher due to the failure of their opposite coils.

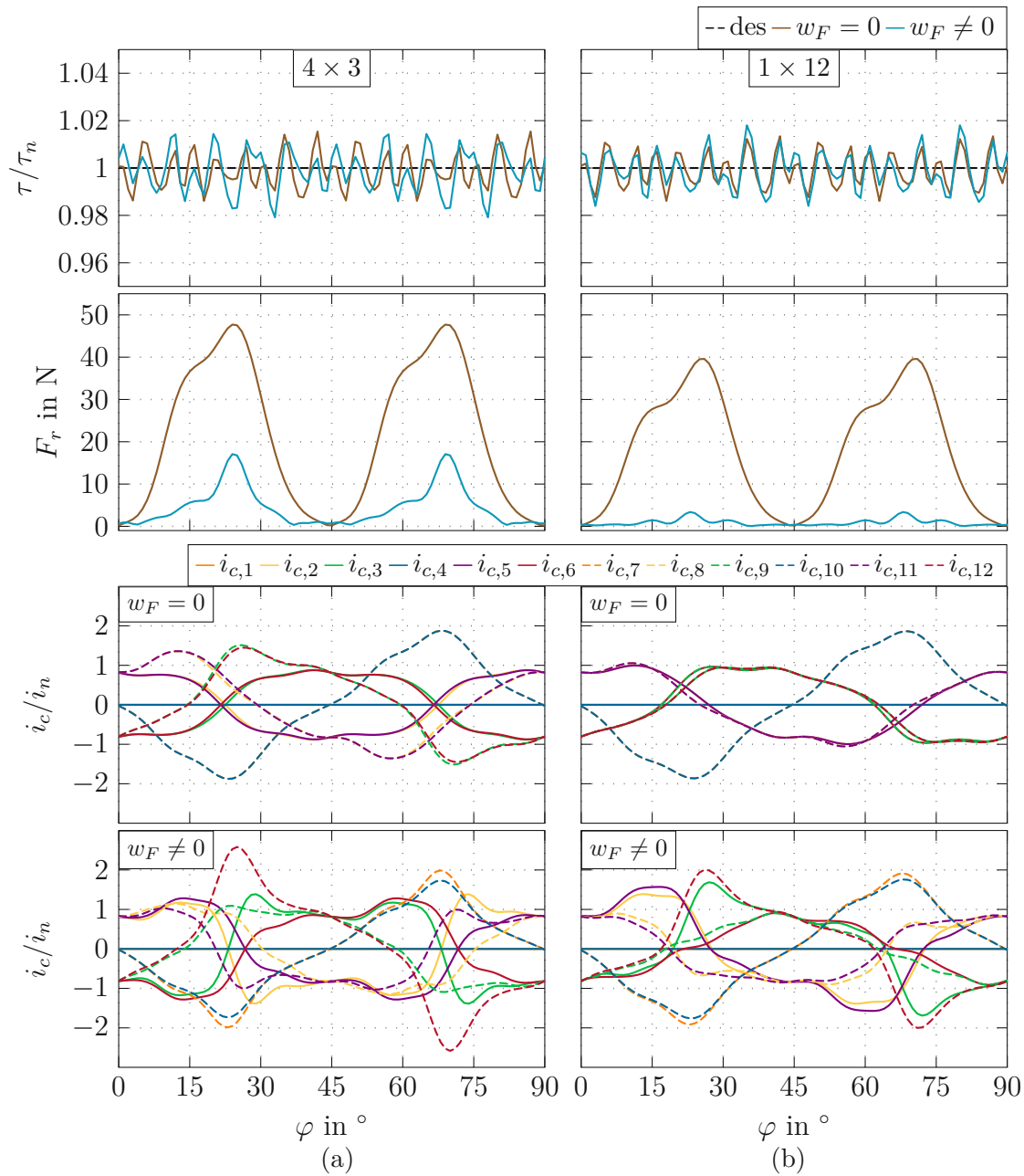


Figure 4.8: Simulation results for the double OC fault case of coils 1 and 4 in a) the 4×3 and b) the 1×12 configuration. The cases without ($w_F = 0$) and with ($w_F \neq 0$) radial force compensation are compared.

4 Current optimization with radial force compensation

In contrast, no symmetry is recognizable in the case with radial force compensation. Additionally, the currents' amplitude is higher for the 12th coil, which belongs to a healthy three-phase system but is adjacent to faulty coil 1. Finally, the current patterns for the case with radial force compensation show slightly faster changes than those without. Tracking these optimal current patterns by a current controller can be challenging.

The same is studied for the 1×12 configuration in Fig. 4.8b. While the torque error is similar to the 4×3 configuration, the radial force compensation is much more effective. Here, the resulting radial force is reduced to about 25% of the radial force achieved in the 4×3 configuration. This is an interesting result since the maximum current amplitude is smaller than for the 4×3 configuration.

A similar scenario is analyzed, now for the double OC fault case of coils 3 and 4 in the 4×3 configuration in Fig. 4.9a and in Fig. 4.9b for the 1×12 configuration. Again, low torque errors are given for all cases in the range of approximately 2% of the nominal torque. The radial forces are decreased in both cases without radial force compensation compared to the double OC fault case of coils 1 and 4. The radial force compensation yields similar amplitudes for both configurations which are slightly increased compared to the previous case. The symmetries within the current patterns are only visible in the case without radial force compensation, where the additional constraints due to Kirchoff's current law are given by in the 4×3 configuration within coils 1 and 2, and 4 and 5. Again, when considering the radial force compensation, no symmetry but fast changes are observable within the current patterns. In addition, the current amplitudes in the 1×12 configuration are lower in this case.

In conclusion, with the current optimization, the defined goals can be accurately achieved for all scenarios, and only minor deviations in the acceptable range occur due to the current approximation procedure. Furthermore, both presented approximation scenarios lead to the conclusion that the additional DOFs of the 1×12 configuration are beneficially utilized in the OC fault cases.

4.3 Approximation for real-time application

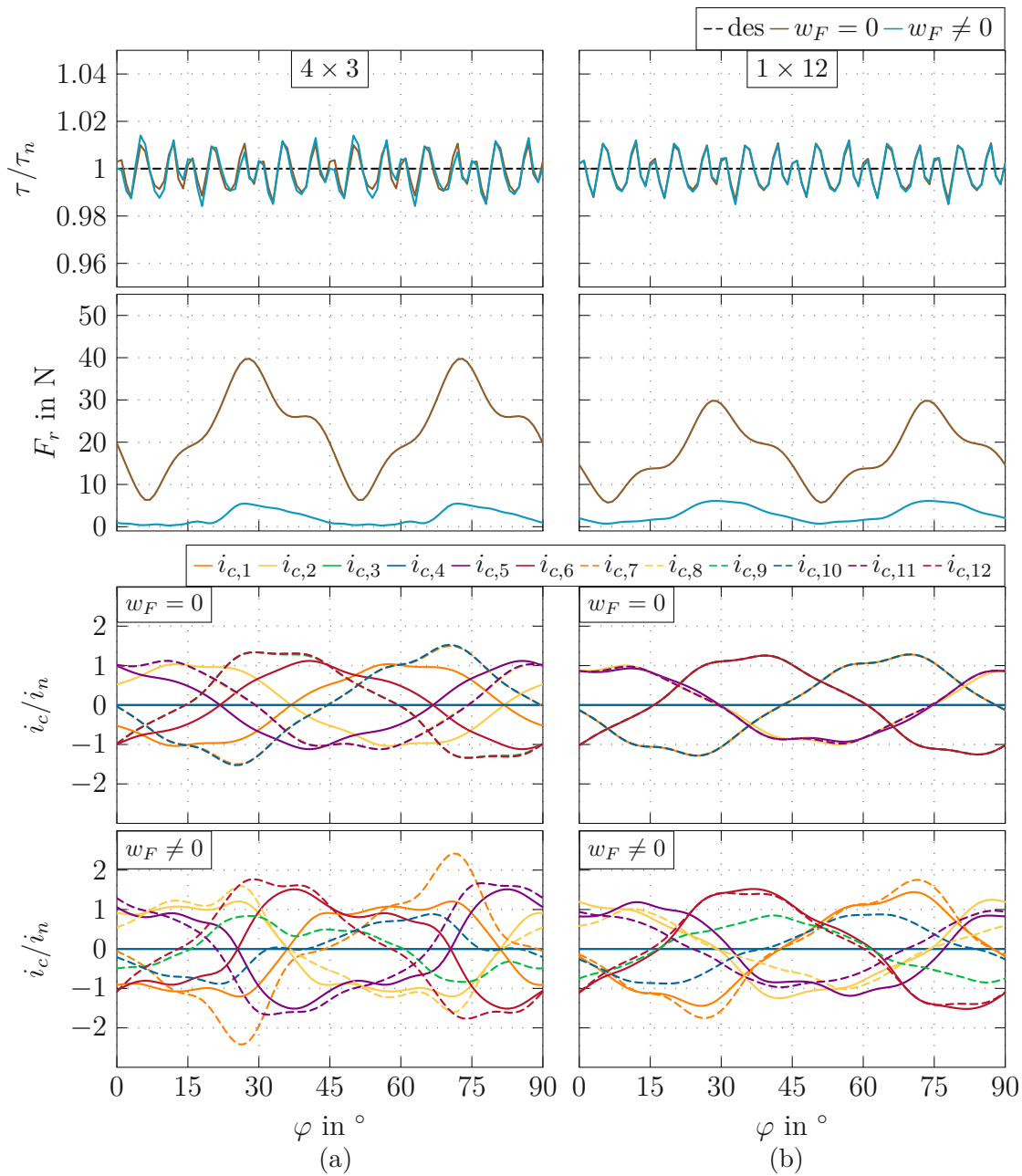


Figure 4.9: Simulation results for the double OC fault case of coils 3 and 4 a) in the 4×3 and b) the 1×12 configuration. The cases without ($w_F = 0$) and with ($w_F \neq 0$) radial force compensation are compared.

5

Fault-tolerant control

Parts of this chapter were published in similar form in the author's previous publication [2].

This chapter is devoted to the fault-tolerant control (FTC) strategy of the multiphase permanent magnet synchronous machine (PMSM). Given the (approximated) optimal current patterns, derived in the previous chapter, the task of the FTC strategy is to track the desired currents as accurately as possible. The basic setup of the proposed FTC strategy is independent of the specific electric circuit configuration, which allows the application of a similar FTC strategy for the healthy-circuit (HC) and open-circuit (OC) fault cases. The current tracking challenges arise from the higher harmonics within the desired current patterns, resulting in fast-changing current amplitudes and unknown disturbances, mainly due to the nonlinear voltage source inverter (VSI) behavior. To overcome these challenges, the FTC strategy consists of a model-based feedforward part (FF), presented in Section 5.1.2, a feedback controller (PI), given in Section 5.1.3, and an iterative learning control (ILC) part, described in Section 5.1.4. For the derivation of the FTC strategy, it is assumed that the voltages \mathbf{v}_c of the 12 stator coils are the (virtual) control input. Thereby, only the available degrees of freedom (DOFs) of the coil currents can be controlled, which are reduced in OC fault cases. An adaptive structure considers this aspect for the feedback controller. The mapping of the coil voltages to the real control input, i.e., the duty cycles $\boldsymbol{\delta}$ of the 12 half-bridges of the VSI, is presented in Section 5.1.5. The block diagram of the proposed control strategy is depicted in Fig. 5.1. Finally, the proposed FTC strategy is compared with a state-of-the-art control strategy including a proportional integral resonant (PIR) controller.

5 Fault-tolerant control

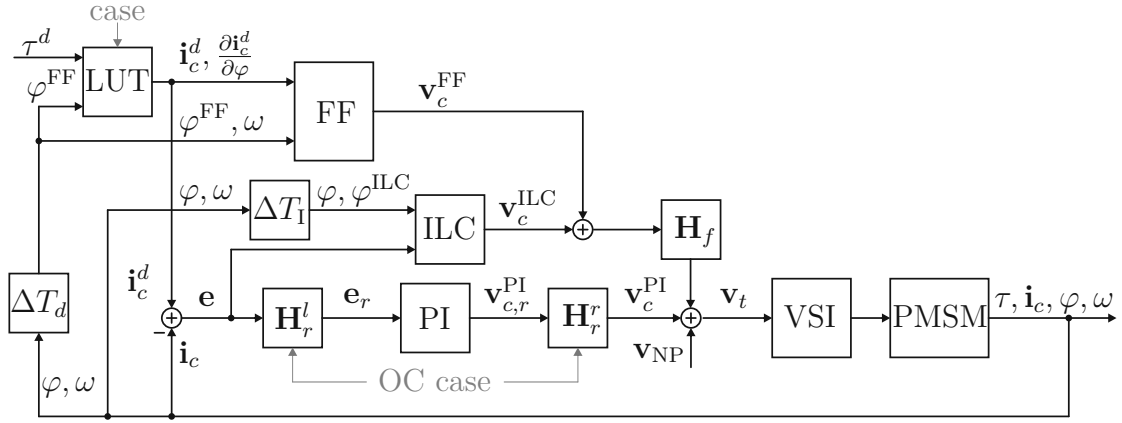


Figure 5.1: Block diagram of the proposed FTC strategy.

5.1 Fault-tolerant control strategy

5.1.1 Current reference signals

The approximated optimized currents derived in Section 4.3 are represented by the Fourier coefficients stored in lookup tables (LUTs) for a number n_τ of desired torque values and all relevant electrical configurations and fault cases. The calculation steps on the real-time system result in the known time delay $\Delta T_d = 2T_s$, with the sampling time $T_s = 100 \mu\text{s}$, from the measurement of the rotor position φ to the output of the corresponding control input. This time delay is approximately compensated by predicting the rotor position in the form

$$\varphi^{FF} = \varphi + \omega \Delta T_d, \quad (5.1)$$

where the assumption that the rotor speed ω remains constant within the time delay is used. This prediction is essential to accurately map the control voltages (particularly of the feedforward control part) to the actual rotor position of the PMSM.

With this delay compensation, the desired currents and the desired current derivatives with respect to the rotor position are given according to (4.4) by

$$\mathbf{i}_c^d(\varphi^{FF}, \tau^d) = \sum_{k=1}^{n_h} \left(\mathbf{c}_k(\tau^d) \cos(\varphi_h^{FF}) + \mathbf{s}_k(\tau^d) \sin(\varphi_h^{FF}) \right) \quad (5.2a)$$

$$\frac{\partial \mathbf{i}_c^d(\varphi^{FF}, \tau^d)}{\partial \varphi} = \sum_{k=1}^{n_h} h_k \left(-\mathbf{c}_k(\tau^d) \sin(\varphi_h^{FF}) + \mathbf{s}_k(\tau^d) \cos(\varphi_h^{FF}) \right) \quad (5.2b)$$

with $\varphi_h^{FF} = h_k n_p \varphi^{FF}$. Advantageously, the derivative does not require additional computing time, as the sine and cosine terms must also be evaluated for the desired

currents. The Fourier coefficients are linearly interpolated to obtain the desired currents for the actual desired torque τ^d .

5.1.2 Feedforward part

Using the model knowledge, the feedforward voltages are derived from Faraday's law of induction (2.21)

$$\mathbf{v}_c = (R_c + R^{\text{VSI}}) \mathbf{i}_c + \frac{d}{dt} \boldsymbol{\psi}_c. \quad (5.3)$$

The first part on the right side of (5.3) is attributed to the resistance of the stator coils and the VSI and is taken into account by

$$\mathbf{v}_c^{\text{R}} = (R_c + R^{\text{VSI}}) \mathbf{i}_c^d \quad (5.4)$$

using the desired optimal currents $\mathbf{i}_c^d = \mathbf{i}_c^d(\varphi^{\text{FF}}, \tau^d)$. The second part can be further evaluated to

$$\frac{d}{dt} \boldsymbol{\psi}_c = \frac{\partial \boldsymbol{\psi}_c}{\partial \varphi} \omega + \frac{\partial \boldsymbol{\psi}_c}{\partial \mathbf{i}_c^d} \frac{d}{dt} \mathbf{i}_c^d, \quad (5.5)$$

which are attributed to the BEMF and stator coil inductances.

Taking a closer look at the back-electromotive force (BEMF) (i.e., the first term of (5.5)), the derivative of the flux linkages with respect to the rotor position must be evaluated at the desired current and rotor position, which is computationally demanding. To simplify calculation in this step, the BEMF is approximated by the BEMF at $\mathbf{i}_c^d = \mathbf{0}$. To do so, the flux linkages are calculated for $\mathbf{i}_c = \mathbf{0}$ by rearranging the first set of equations in (2.23b) to

$$\boldsymbol{\psi}_c \Big|_{\mathbf{i}_c=\mathbf{0}} = \bar{\mathbf{D}}_c \mathcal{G}_c (\mathbf{D}_m^{\text{T}} \mathbf{u}_{tm} + \mathbf{D}_g^{\text{T}} \mathbf{u}_{tg}). \quad (5.6)$$

The values of $\boldsymbol{\psi}_c$ at rotor positions $\varphi = [0^\circ, \Delta\varphi, \dots, 360^\circ/n_p]$, with a rotor position increment of $\Delta\varphi = 0.16^\circ$, are approximated by a Fourier series

$$\check{\boldsymbol{\psi}}_c(\varphi) = \sum_{k=1}^3 (\mathbf{c}_{\psi,k} \cos(h_{\psi,k} n_p \varphi) + \mathbf{s}_{\psi,k} \sin(h_{\psi,k} n_p \varphi)). \quad (5.7)$$

The choice of $\mathbf{h}_{\psi} = [h_{\psi,1}, h_{\psi,2}, h_{\psi,3}]^{\text{T}} = [1, 5, 7]^{\text{T}}$ yields an root-mean-square approximation error below 0.14% of the maximum flux linkage value for all coils. The feedforward BEMF voltages are then calculated by

$$\mathbf{v}_c^{\text{BEMF}} = \omega \frac{\partial \check{\boldsymbol{\psi}}_c(\varphi^{\text{FF}})}{\partial \varphi}. \quad (5.8)$$

5 Fault-tolerant control

Taking into account the definition of the desired currents, the second part of (5.5) can be expanded as

$$\frac{\partial \psi_c}{\partial \mathbf{i}_c^d} \frac{d}{dt} \mathbf{i}_c^d = \frac{\partial \psi_c}{\partial \mathbf{i}_c^d} \left(\frac{\partial \mathbf{i}_c^d}{\partial \varphi} \omega + \frac{\partial \mathbf{i}_c^d}{\partial \tau^d} \frac{d}{dt} \tau^d \right). \quad (5.9)$$

The following approximations are meaningful:

1. The user or a superordinate control loop defines the desired torque τ^d . Thus, typically, no information on the time derivative of the desired torque is available, and it makes sense to use $d\tau^d/dt = 0$ within the feedforward part.
2. Although $\partial \psi_c / \partial \mathbf{i}_c^d$ (i.e., the inductance matrix) can be calculated similarly to the BEMF by using the desired currents in the model (2.23b), this calculation is time-consuming and thus not feasible for real-time implementation. To analyze the inductance matrix of the PMSM, $\partial \psi_c / \partial \mathbf{i}_c^d$ is evaluated offline for various coil currents and rotor positions. The results show a dominant self-inductance $L_{c,s} = \partial \psi_{c,k} / \partial i_{c,k}$ and a small symmetric coupling inductance to the adjacent coils $L_{c,c} = \partial \psi_{c,k\pm 1} / \partial i_{c,k}$. Both self- and coupling inductances show almost no current amplitude dependency but a rotor position dependency. Only the mean value of the self-inductance $L_s = \bar{L}_{c,s}$ is used to keep the real-time implementation simple.

With these approximations, the overall simplified second part of (5.5) reads as

$$\mathbf{v}_c^L = L_s \omega \frac{\partial \mathbf{i}_c^d(\varphi^{\text{FF}}, \tau^d)}{\partial \varphi}, \quad (5.10)$$

where the desired current derivative with respect to the rotor position is given by (5.2a). In total, the feedforward voltages \mathbf{v}_c^{FF} are composed of the three terms given by

$$\mathbf{v}_c^{\text{FF}} = \mathbf{v}_c^{\text{R}} + \mathbf{v}_c^{\text{BEMF}} + \mathbf{v}_c^L. \quad (5.11)$$

derived from the approximated terms for (5.3) and (5.5).

It has to be noted that this approach covers the dominant parts of the feedforward control and renders low computational costs. Feedback control is required to reduce the influence of the errors introduced by these simplifications and to compensate for model-plant mismatch, as described in the subsequent sections.

5.1.3 PI controller

The PI controller is derived by applying $\mathbf{v}_c = \mathbf{v}_c^{\text{FF}} + \mathbf{v}_c^{\text{PI}}$, with the feedforward voltages \mathbf{v}_c^{FF} according to (5.11) to (2.21), which gives

$$\left(\frac{\partial \psi_c}{\partial \varphi} - \frac{\partial \check{\psi}_c}{\partial \varphi} \right) \omega + \frac{\partial \psi_c}{\partial \mathbf{i}_c} \frac{d}{dt} \mathbf{i}_c - L_s \frac{\partial \mathbf{i}_c^d}{\partial \varphi} \omega = (R_c + R^{\text{VSI}}) \mathbf{e} + \mathbf{v}_c^{\text{PI}}, \quad (5.12)$$

with $\mathbf{e} = \mathbf{i}_c^d - \mathbf{i}_c$. Assuming that the error in the BEMF is small and using a similar approximation of the inductance matrix $\partial\boldsymbol{\psi}_c/\partial\mathbf{i}_c \approx \text{diag}[L_s, \dots, L_s]$ as in the feedforward part results in the simplified error dynamics

$$L_s \frac{d}{dt} \mathbf{e} = - (R_c + R^{\text{VSI}}) \mathbf{e} - \mathbf{v}_c^{\text{PI}}, \quad (5.13)$$

which is the basis for the design of the PI controller.

It was discussed in detail in Section 2.4 that due to the electric interconnection and possible OC faults, not all coil currents can be chosen independently. Therefore, the PI controller is only applied to the independent (controllable) currents. The currents and voltages are transformed by left multiplication of (5.13) with \mathbf{H}_r^t (see Section 2.4), yielding the reduced current error $\mathbf{e}_r = \mathbf{i}_{c,r}^d - \mathbf{i}_{c,r}$, the transformed voltage $\mathbf{v}_{c,r}^{\text{PI}}$, and transformed simplified error dynamics

$$L_s \frac{d}{dt} \mathbf{e}_r = - (R_c + R^{\text{VSI}}) \mathbf{e}_r - \mathbf{v}_{c,r}^{\text{PI}}. \quad (5.14)$$

The PI controller

$$\mathbf{v}_{c,r}^{\text{PI}} = - (R_c + R^{\text{VSI}} + L_s \lambda_p) \mathbf{e}_r - L_s \lambda_i \int \mathbf{e}_r dt, \quad (5.15)$$

with the controller parameters $\lambda_p > 0$ and $\lambda_i > 0$, guarantees exponential stability of the simplified error dynamics. The tuning of the controller parameters is based on pole assignment.

5.1.4 Iterative learning control (ILC)

Accurate current tracking is required for the optimal operation of the PMSM. The primary challenge is the high relevance of harmonics up to order 9 of the optimal current patterns for the OC fault cases. Due to the PI controller's limited bandwidth, it is impossible to completely suppress current errors resulting from model simplifications and nonlinear VSI effects, particularly at high rotor speeds. Therefore, an ILC part is added as a third part of the control strategy to reduce the current tracking error further.

ILC strategies have been recently investigated in the literature for the control of PMSMs to reduce unknown or unmodeled periodic effects. This strategy is commonly used for compensating nonlinear effects such as cogging torque and non-fundamental wave behavior. Thereby, different error signals are considered to learn the required adaptations which will further decrease the error, i.e., the speed error is investigated in [91–93], the torque error is considered in [58, 94–98] and current errors are regarded in [32, 60, 92]. Advantageously, the rotor position

5 Fault-tolerant control

can be utilized as a repetitive learning grid for drive applications, see [60, 94–96, 99], in which the proposed ILC strategies consist of proportional learning gains including forgetting factors to vanish the influence of older measurement signals. However, the available system knowledge is not used to design the ILC strategies. In contrast, the presented ILC in this work utilizes a stochastic optimal, model-based learning law, representing a regularized system inversion, see e.g., [100], according to the expected signal-to-noise ratio. The stochastic approach proposed in [101] is considered to suppress the current errors down to almost the current sensor noise level. The main idea is to utilize the periodicity of the current patterns with respect to the rotor position to learn the required additional coil voltages $\mathbf{v}_c^{\text{ILC}}$, i.e., $\mathbf{v}_c = \mathbf{v}_c^{\text{FF}} + \mathbf{v}_c^{\text{PI}} + \mathbf{v}_c^{\text{ILC}}$, such that the current error $\mathbf{e} = \mathbf{i}_c^d - \mathbf{i}_c$ is minimized. An equally spaced grid of the rotor positions over a full rotation is applied. Decoupled error dynamics similar to (5.13) are assumed to ensure real-time capability, allowing to derive the ILC law for each coil individually. The first step is to derive the ILC learning law based on a simplified representation of the closed-loop system consisting of the electric circuit model

$$G^{\text{P}}(s) = \frac{1}{(sL_s + R_c + R^{\text{VSI}})} \quad (5.16)$$

and the PI controller

$$R^{\text{PI}}(s) = (R_c + R^{\text{VSI}} + L_s\lambda_p) + \frac{L_s\lambda_i}{s}, \quad (5.17)$$

with the complex Laplace variable s . The ILC learning filter for each coil then reads [101]

$$\mathcal{L}^{\text{ILC}}(s) = \frac{S(s)G(-s)}{G(s)S(s)G(-s) + \bar{\sigma}_i}, \quad (5.18)$$

with the ILC plant model

$$G(s) = \frac{G^{\text{P}}(s)}{1 + R^{\text{PI}}(s)G^{\text{P}}(s)}, \quad (5.19)$$

the mean variances of the current sensor's noise $\bar{\sigma}_i$, and the input error power spectral density (PSD) function $S(s)$, chosen as

$$S(s) = \frac{V}{(1 + Ts)(1 - Ts)}, \quad (5.20)$$

with low-pass characteristics tunable by the gain V and the time constant T . The non-causal impulse response of (5.18) is obtained using the inverse Fourier transform in the form $\mathcal{L}^{\text{ILC}}(t) = \mathcal{F}^{-1}(\mathcal{L}^{\text{ILC}}(\mathbf{l}\omega))$. The required filter coefficients

5.1 Fault-tolerant control strategy

of a finite-impulse response (FIR) filter approximation with a fixed filter length of $2m + 1 = 81$ steps ($m = 40$) are given by

$$\mathbf{w}^{\text{ILC}} = T_s \begin{bmatrix} \mathcal{L}^{\text{ILC}}(-mT_s) \\ \vdots \\ \mathcal{L}^{\text{ILC}}(mT_s) \end{bmatrix}, \quad (5.21)$$

where $\mathcal{L}^{\text{ILC}}(t)$ is evaluated at the time steps $t = (-m, -m+1, \dots, m) T_s$. Applying this filter to the current error e_j of coil $j = 1, \dots, 12$ yields the filtered error

$$e_{j,k-m}^{\text{ILC}} = \begin{bmatrix} e_{j,k-2m} & \dots & e_{j,k-1} & e_{j,k} \end{bmatrix} \mathbf{w}^{\text{ILC}}. \quad (5.22)$$

It is important to note that this non-causal filtering is possible since the ILC operates from one rotation of the PMSM to the next, executing repetitively the update process of the corresponding filtered current errors stored in a ring buffer at the time $k - m$.

In the second step, a learning grid of rotor positions with a grid size of $\Delta\varphi = 0.025^\circ$ within one mechanical revolution is defined. The filtered error $e_{j,k-m}^{\text{ILC}}$ is then mapped to the closest grid position Δ_k by rounding the corresponding measured rotor position value φ_{k-m} to the nearest grid index value. The update process of the ILC coil voltage vector \mathbf{V} at the k -th index value reads as

$$V_{\kappa+1,j}^{\text{ILC}}(\Delta_k) = V_{\kappa,j}^{\text{ILC}}(\Delta_k) + e_j^{\text{ILC}}(\Delta_k), \quad (5.23)$$

where $e_j^{\text{ILC}}(\Delta_k) = e_{j,k-m}^{\text{ILC}}(\varphi_{k-m})$ is the filtered current error at the corresponding grid index Δ_k for the rotor position φ_{k-m} . The ILC iteration index is indicated by κ .

Remark 2. The update process of (5.23) is only executed if a new value for the rotor position index Δ_k is provided for two consecutive update steps in the time domain $\Delta_k \neq \Delta_{k-1}$. This prevents the ILC from learning at a standstill. Due to the grid size choice, at rotational speeds above $n > \Delta\varphi n_p / (6T_s) = 166.66$ rpm, the index values can skip one or several neighboring values. In this case, a linear interpolation between the actual and the last measured index positions provides the update steps of the skipped index values. Additionally, the learning of the ILC is stopped for one iteration if the desired torque change is higher than $d\tau^d/dt > 2000\tau_n s^{-1}$. This is done to avoid learning the fast transient response, which is irrelevant to the regular ILC operation.

Finally, the additional coil voltage $v_{j,k}^{\text{ILC}}$ of the ILC is given by

$$v_{j,k}^{\text{ILC}} = V_j^{\text{ILC}} \left(\left| \frac{\varphi_k^{\text{ILC}}}{\Delta\varphi} \right| \right), \quad (5.24)$$

5 Fault-tolerant control

using the learning grid index value obtained at the predicted rotor position

$$\varphi_k^{\text{ILC}} = \varphi_k + \omega_k \Delta T_I, \quad (5.25)$$

which is given by the ILC's time delay ΔT_I analogously to (5.1). This procedure is executed for each stator coil j , resulting in the overall vector $\mathbf{v}_c^{\text{ILC}} = [v_1^{\text{ILC}}, \dots, v_{12}^{\text{ILC}}]^T$. The overall ILC concept is visualized in Fig. 5.2.

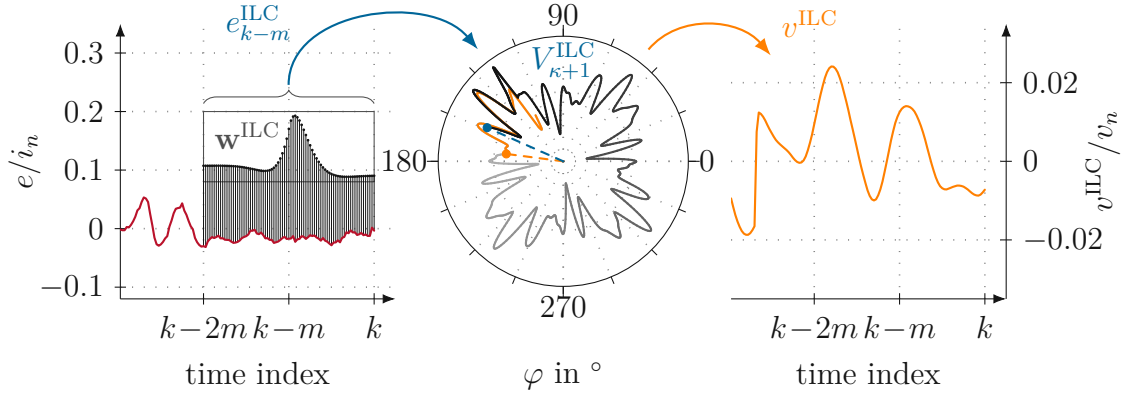


Figure 5.2: Rotor position-based ILC concept for one coil.

5.1.5 Terminal voltage mapping

In the final part of the control strategy, the coil voltages \mathbf{v}_c are mapped to the terminal voltages \mathbf{v}_t . The feedforward parts \mathbf{v}_c^{FF} and $\mathbf{v}_c^{\text{ILC}}$ are defined for all 12 coils, while the PI controller part is defined for the reduced set of coil voltages $\mathbf{v}_{c,r}^{\text{PI}}$. Thus, it is required to consider OC faults for the feedforward parts, and the reduced voltages must be mapped to the terminal voltages. For this, it is necessary to define the average isolated neutral point voltages \mathbf{v}_{NP} against ground, cf. Fig. 2.5 and Fig. 2.4. In the literature, the isolated neutral point potential is commonly set to half the dc-link voltage to enable the largest coil voltage operational area [102]. This means that the voltages $\mathbf{v}_{\text{NP}} = 0.5\mathbf{V}_{dc}$ are used. The mapping from coil voltages to terminal voltages is then given by

$$\mathbf{v}_t = \mathbf{H}_f (\mathbf{v}_c^{\text{FF}} + \mathbf{v}_c^{\text{ILC}}) + \mathbf{H}_r^r \mathbf{v}_{c,r}^{\text{PI}} + \mathbf{v}_{\text{NP}}. \quad (5.26)$$

Thereby, $\mathbf{H}_f = \mathbf{I}$ corresponds to the identity matrix in the HC case. In the OC fault case, the diagonal entry corresponding to a faulty coil f is replaced by zero. This means only the healthy coil voltages' feedforward and ILC parts are added to the terminal voltages. The reduced voltages of the PI controller $\mathbf{v}_{c,r}^{\text{PI}}$ are mapped

through the reduced matrices described in Section 2.4 to the terminal voltages. As the real control inputs are the terminal duty cycles $\boldsymbol{\delta}$, they are then expressed by

$$\boldsymbol{\delta} = (\mathbf{V}_{dc})^{-1} \mathbf{v}_t, \quad (5.27)$$

with the dc-link voltages of (3.1).

5.1.6 Proportional integral resonant (PIR) controller

To compare the proposed control strategy with scientific state-of-the-art controllers, a proportional integral resonant (PIR) control strategy is designed as described in [34, 103–105]. The PIR controller comprises a PI controller identical to Section 5.1.3 and the resonant (R) controller. This allows to systematically consider the higher harmonics of the electrical rotor angular frequency in the current error $\mathbf{e} = \mathbf{i}_c^d - \mathbf{i}_c$. Similar to the PI controller, the R controller is designed for reduced coil currents, which yields the PIR control voltages $\mathbf{v}_c^{\text{PIR}}$ given by

$$\mathbf{v}_c^{\text{PIR}} = \mathbf{H}_r^r (\mathbf{v}_{c,r}^{\text{PI}} + \mathbf{v}_{c,r}^{\text{R}}) \quad (5.28)$$

with the resonant part $\mathbf{v}_{c,r}^{\text{R}}$.

The design of the R controller is inspired by the method proposed in [103], which uses a state-space representation for the harmonic order h of the resonant part for the reduced current j

$$\frac{d}{dt} \mathbf{x}_h = \begin{bmatrix} 0 & -hn_p\omega \\ hn_p\omega & 0 \end{bmatrix} \mathbf{x}_h + \begin{bmatrix} 1 \\ 0 \end{bmatrix} e_{r,j} \quad (5.29a)$$

$$y_h = \begin{bmatrix} K_h^{\text{R}} & 0 \end{bmatrix} \mathbf{x}_h, \quad (5.29b)$$

where K_h^{R} is the controller gain. In this work, an equivalent cosine-sine representation is proposed in the following form

$$\frac{d}{dt} \mathbf{c}_h^{\text{R}} = K_h^{\text{R}} \cos(hn_p\varphi) \mathbf{e}_r \quad (5.30a)$$

$$\frac{d}{dt} \mathbf{s}_h^{\text{R}} = K_h^{\text{R}} \sin(hn_p\varphi) \mathbf{e}_r \quad (5.30b)$$

$$\mathbf{v}_{c,r,h}^{\text{R}} = \mathbf{c}_h^{\text{R}} \cos(hn_p\varphi) + \mathbf{s}_h^{\text{R}} \sin(hn_p\varphi), \quad (5.30c)$$

with the coefficient vectors \mathbf{c}_h^{R} and \mathbf{s}_h^{R} for cosine and sine for the h -th harmonic order. The equivalence of (5.29) and (5.30) is derived in Appendix A.1. The advantage of this representation is that the rotor position measurement is directly used instead of the rotor angular frequency. Furthermore, each trigonometric

5 Fault-tolerant control

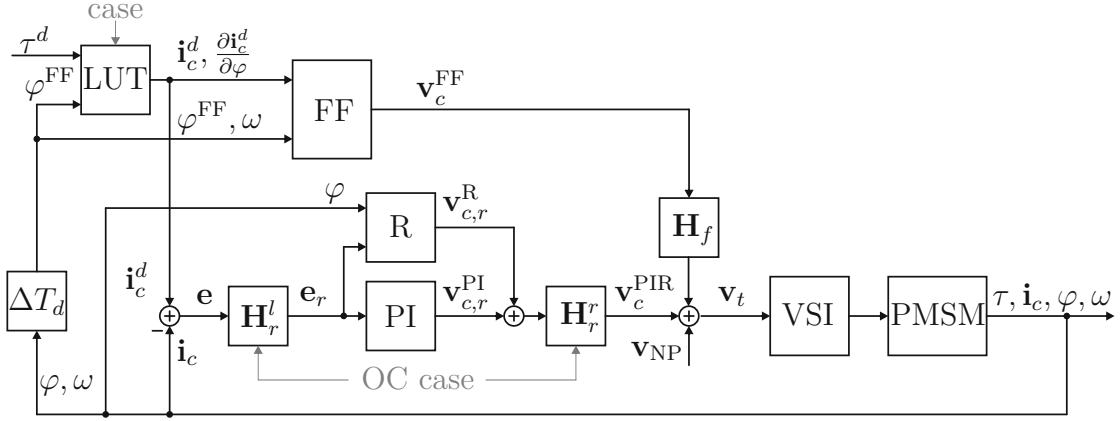


Figure 5.3: Block diagram of the PIR control strategy.

function has to be evaluated only once within each step for all current errors. Thus, the computational costs are low. In contrast to [103], the cosine-sine representation does not involve divisions.

The overall R controller voltages are given as the sum of several R controller voltages in the form

$$\mathbf{v}_{c,r}^R = \sum_{k=1}^{n_h^R} \left(\mathbf{c}_k^R \cos(h_k^R n_p \varphi) + \mathbf{s}_k^R \sin(h_k^R n_p \varphi) \right), \quad (5.31)$$

with the specific harmonic orders $\mathbf{h}^R = [1, 2, 5, 7]$ and $\mathbf{h}^R = [1, 2, 3, 5, 7, 9]$ for the HC and OC case, respectively. The corresponding length of \mathbf{h}^R is given by n_h^R . It has to be noted that the second harmonic component (which is not present in the approximation of the optimal current patterns) is added to correct the errors resulting from the approximated inductances, cf. Section 5.1.2. Although the specific form of implementation is new, the method of the R controller is state of the art in the literature. The PIR controller's resulting overall structure is shown in Fig. 5.3.

5.2 Control strategy results

In the following sections, the results of the proposed FTC strategy in post-fault situations are achieved by measurements on the test stand, cf. Section 3.1. With several scenarios, the proposed FTC strategy is extensively evaluated, and its performance compared to the PIR reference control strategy in the HC case, see Section 5.2.1. The OC post-fault performance of the proposed FTC strategy is evaluated in Section 5.2.2 for selected single, double, and triple OC fault cases.

The overall performance comparison of both the 4×3 and the 1×12 configuration are given in Section 5.2.3.

5.2.1 Healthy-circuit case

In the first scenario, the control strategy is validated for the HC case in the 4×3 configuration. First, the ILC part is omitted to show the effectiveness and limits of the feedforward control part and the PI feedback controller. Figure 5.4 presents the measurement results for various constant desired torque values up to twice the nominal torque τ_n . The PMSM is rotated by the IM at a constant speed of $n = 60$ rpm on the left and $n = 720$ rpm on the right side of Fig. 5.4. For the slow speed, good torque tracking accuracy can be achieved, which is assessed by the measurements of the torque sensor (meas.) and the model-based calculated torque (model). A high current tracking accuracy can be seen for the currents depicted in the third row and the current errors in the fourth row. The resulting terminal voltages are depicted in the last row of Fig. 5.4.

In contrast, the torque tracking errors are up to ten times higher at higher speeds, as depicted on the right side. Note that the torque sensor measurements are disturbed by the mechanical vibrations on the test stand at higher speeds and, thus, are not depicted. The higher torque tracking error is attributed to the significant current tracking errors. The PI feedback controller cannot suppress the fast-changing errors, which also explains the motivation for incorporating the ILC into the proposed control strategy. Finally, the amplitude of the terminal voltages is already close to its maximum value at $n = 720$ rpm. Thus, operation at significantly higher speeds is impossible for the given setup without field weakening control, which is not part of the proposed FTC strategy.

As described in Section 5.1.4, the ILC is introduced to reduce the current tracking error at high rotational speeds of the motor. The PIR control is also motivated in the literature by the need to reduce the current tracking error. Therefore, the following scenario compares the proposed ILC strategy with the PIR reference control strategy in the HC case for the 4×3 and the 1×12 configuration at $n = 720$ rpm. Thereby, three dynamic torque trajectories are studied: a step up to the nominal torque value and back to zero, a ramp up and down to twice the nominal torque value with a torque slope of $d\tau^d/dt = 2\tau_n s^{-1}$ and a chirp signal with an amplitude of half the nominal torque and an exponential increase of the frequency from 0.1 Hz to 50 Hz. The results depicted in Fig. 5.5 for the 4×3 and in Fig. 5.6 for the 1×12 configuration show that a torque tracking error, similar to the low-speed in Fig. 5.4, is achieved in steady state and for the ramp case. Note that the proposed FTC strategy results in approximately half of the PIR control strategy's current tracking error in steady state, which is also reflected in

5 Fault-tolerant control

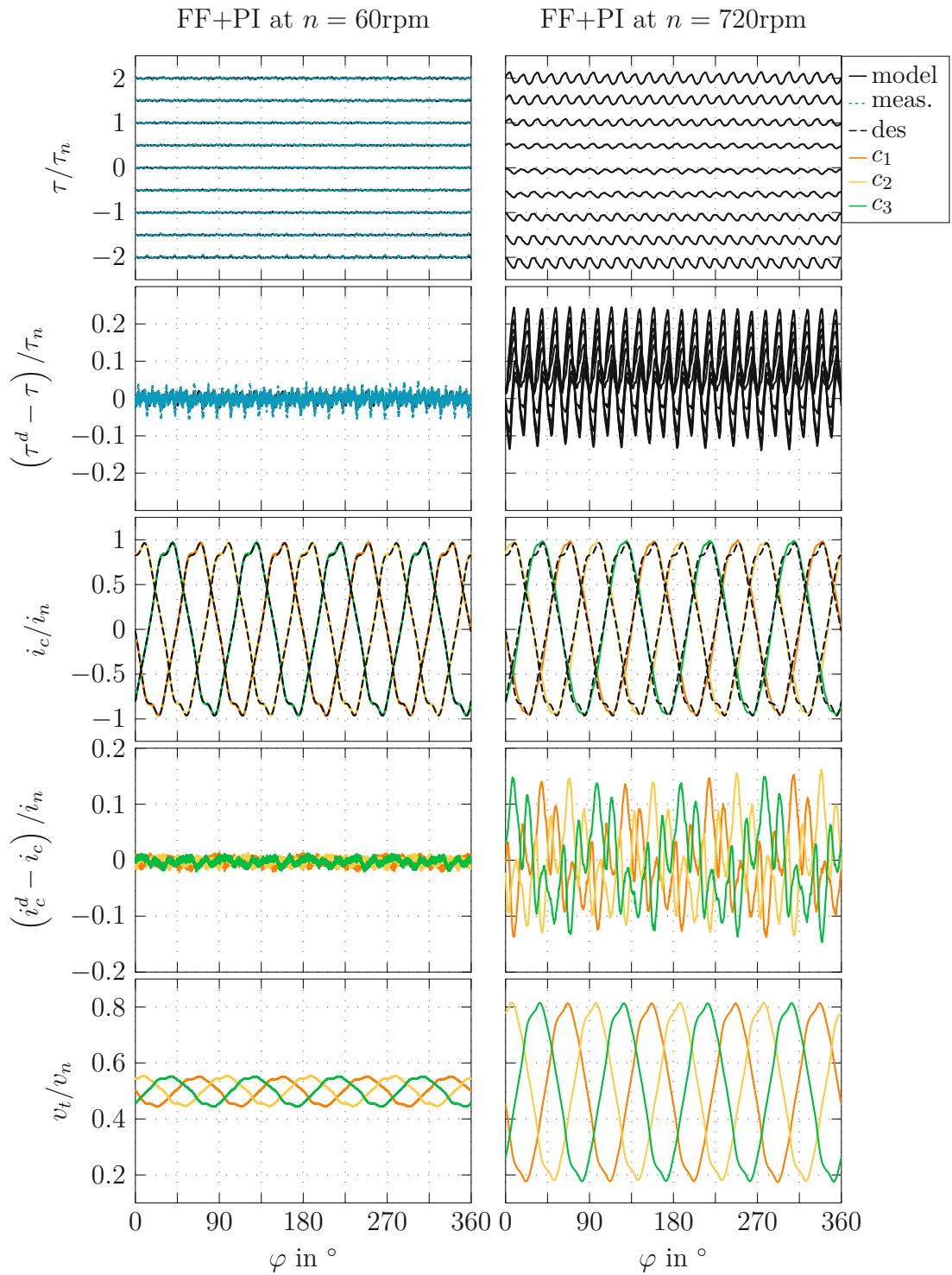


Figure 5.4: Measurement results of the feedforward and PI controller for the HC case in the 4×3 configuration: $n = 60 \text{ rpm}$ on the left side and $n = 720 \text{ rpm}$ on the right side.

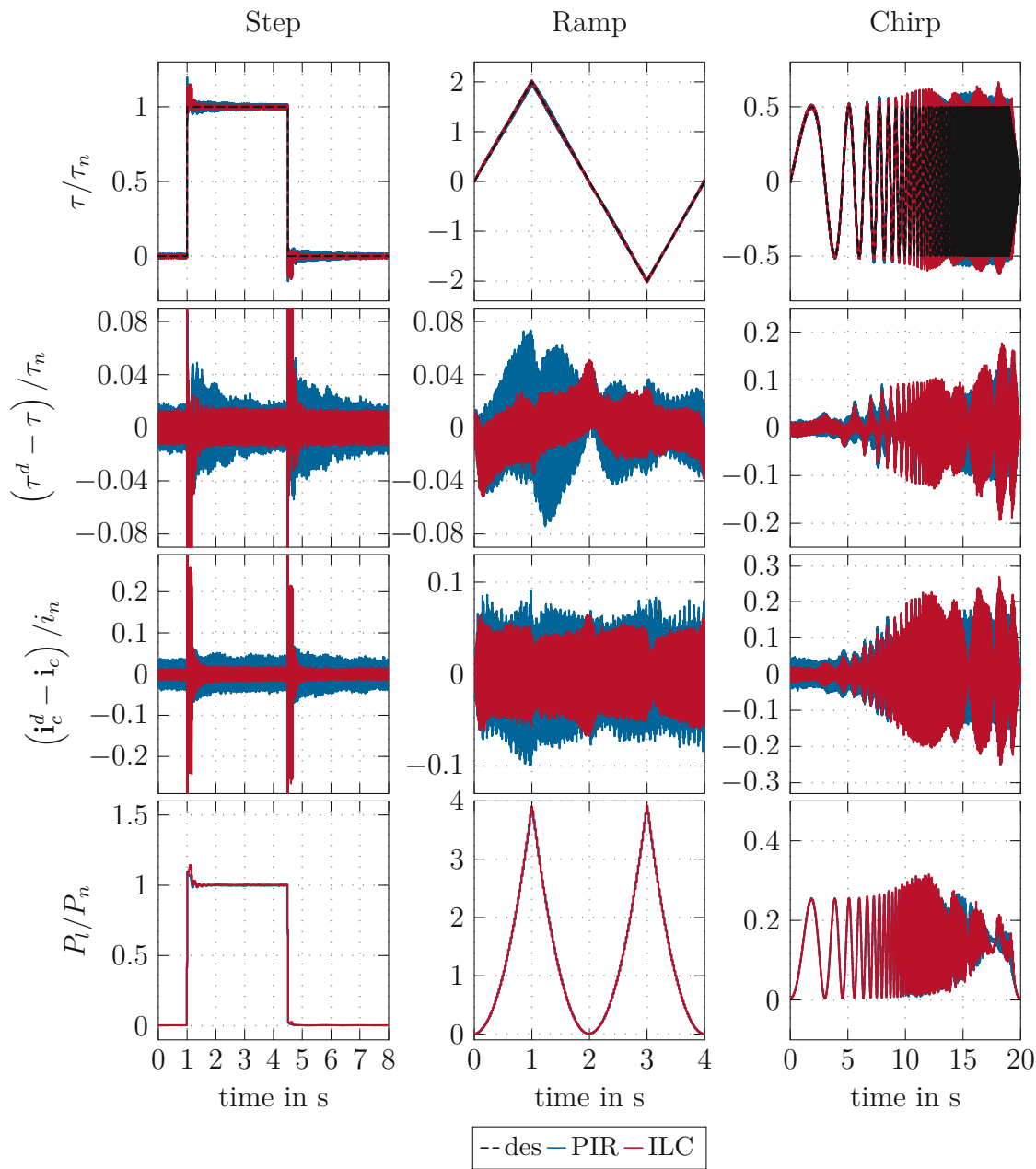


Figure 5.5: Measurement results of the FTC strategy and the reference PIR control strategy for the HC case in 4×3 configuration at high speeds $n = 720$ rpm.

a smaller torque tracking error. In the third plot rows, $i_c^d - i_c$ indicates all twelve current tracking error waveforms displayed one above the other. In the dynamic changes of the desired torque, both control strategies give approximately similar results, with slightly more consistent torque tracking for the PIR controller. This

5 Fault-tolerant control

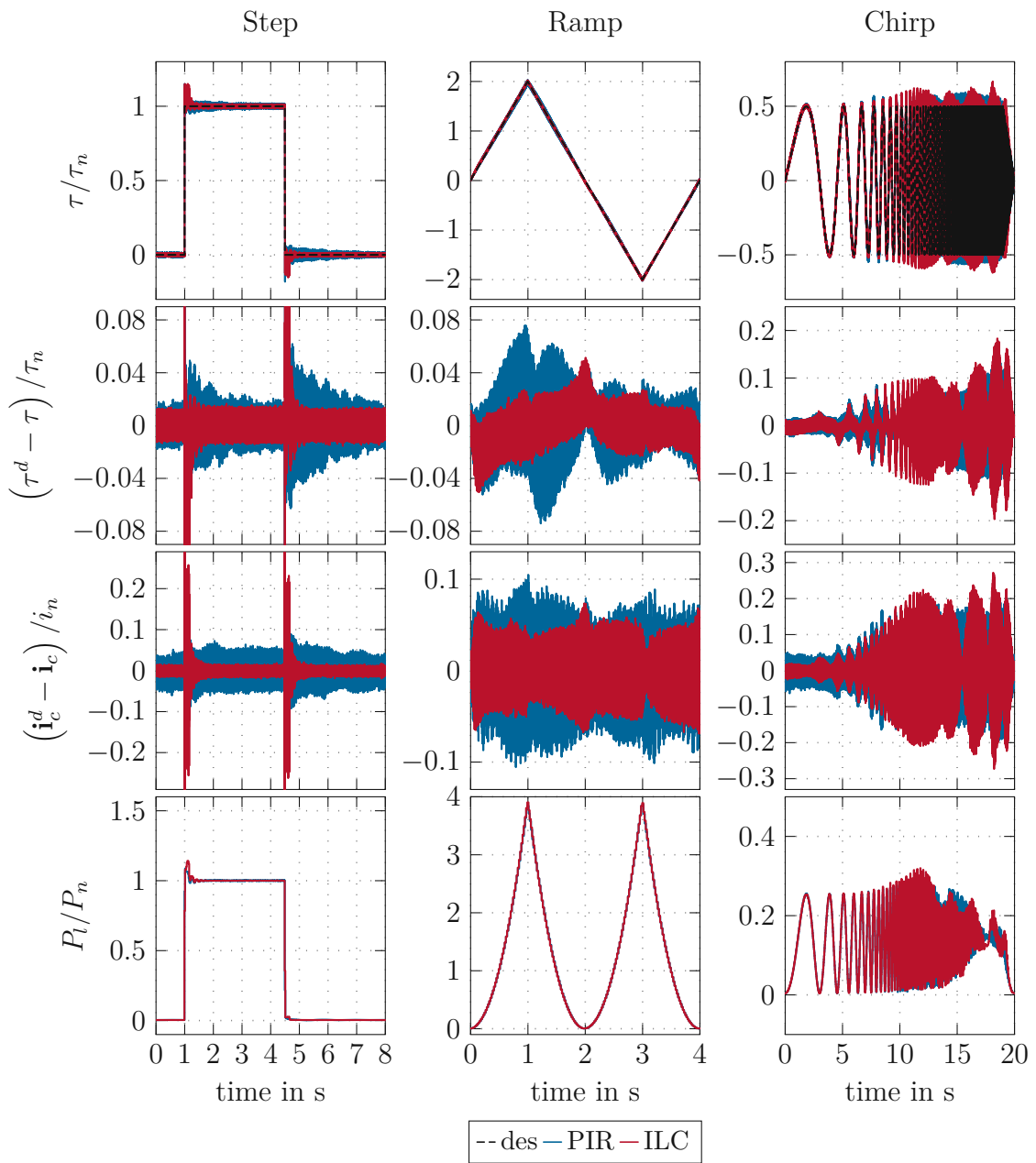


Figure 5.6: Measurement results of the FTC strategy and the reference PIR control strategy for the HC case in 1×12 configuration at high speeds $n = 720$ rpm.

is because the learning of the ILC lags behind the fast desired torque changes. Only minor deviations in the results are noticeable comparing both configurations in Fig. 5.5 and Fig. 5.6.

A detailed view of the transient response of the current errors after a step in the desired torque in Fig. 5.5 is provided in Fig. 5.7 for the 4×3 configuration. As the transient of the desired torque is higher than the threshold value for learning in the ILC, the period after the step is excluded from learning. Therefore, the current tracking error is slightly larger than for the PIR right after the step. However, it can be observed that after the first iteration of the ILC, the same magnitude of current error as for the reference control strategy is achieved and further reduced for each iteration. After 10 iterations of the ILC, the variance of the remaining current errors stays below six times the noise level, decreasing down to two times the noise level at steady state, see the time interval 0.9s to 1s in Fig. 5.7. For comparison, the achieved variance with the PIR control strategy stays below 50 and 30 times the noise level in the same periods.

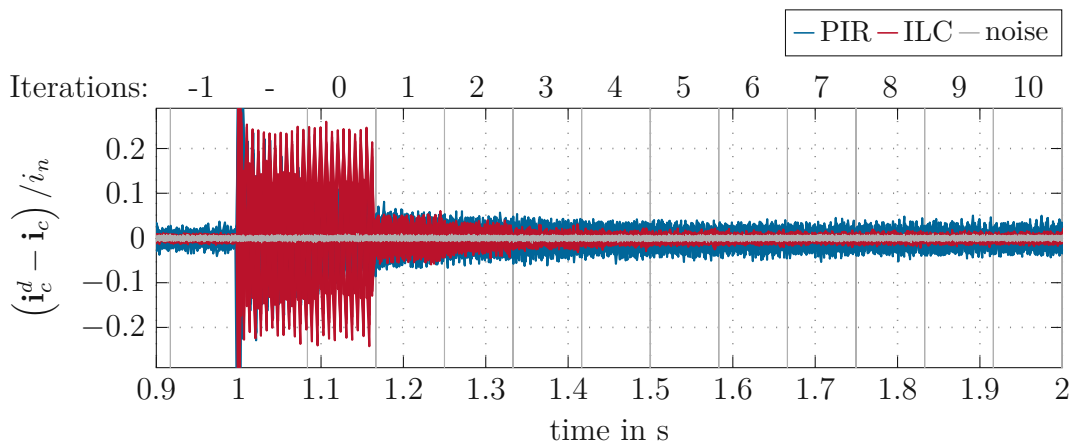


Figure 5.7: Detailed current error plot for the torque step case depicted in Fig. 5.5.

5.2.2 Multiple open-circuit post-fault cases

In this section, measurement results for OC fault cases are presented. Therein, the proposed FTC strategy is utilized for all OC fault cases. The PIR reference control strategy cannot be employed since it tends to instability at high speeds in the case of OC faults, which can only be avoided by decreasing the control gains. This, however, entails a huge loss of accuracy.

The influence of the order of the current harmonic order approximation is validated in Fig. 5.8. Constant desired torque values $\tau^d = [-1, -0.75, \dots, 1]\tau_n$ are tested, considering the specified harmonic orders in the 4×3 and the 1×12 configuration for double OC fault cases of coils 1 and 4, and coils 3 and 4. The bars indicate the errors described in (4.5). The results presented in Fig. 5.8 show that

5 Fault-tolerant control

the errors of the measurements are larger than in the simulation, which can be attributed to the inherent model errors, neglecting the VSI in simulation, and the measurement noise. However, a perfect match between the simulation results and the measurements on the test stand is achieved concerning predicting the influence of the harmonic orders on the achievable reduction in the torque error and the radial force.

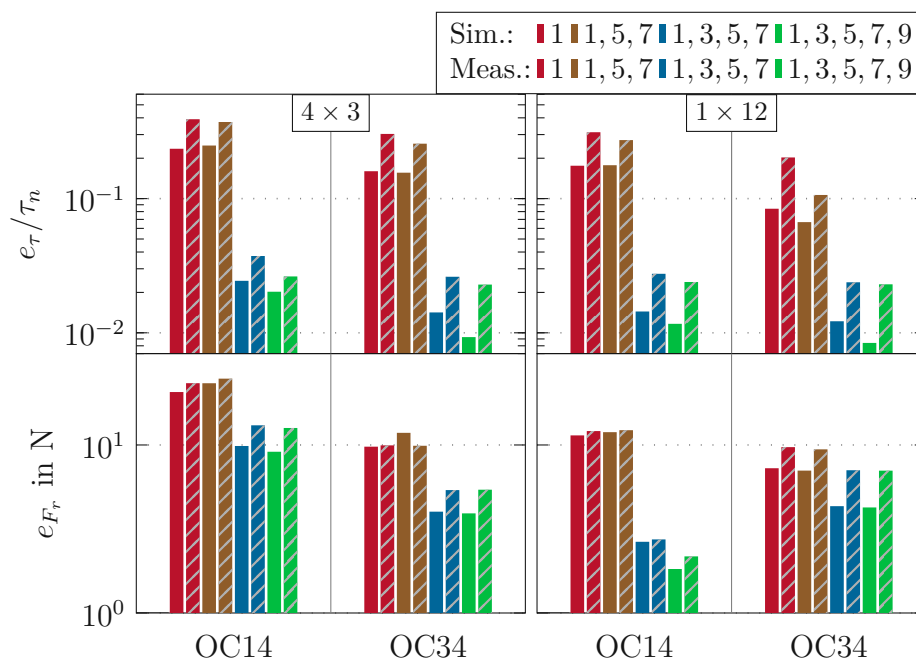


Figure 5.8: Simulated and measured current approximation errors for the torque (upper plots) and the radial forces (lower plots) in double OC fault cases of coils 1 and 4, and coils 3 and 4 of the 4×3 configuration on the left and the 1×12 configuration on the right plot column.

The single OC fault case of coil 1 is investigated for a torque step up to the nominal torque value and down to zero at high speed $n = 720$ rpm in Fig. 5.9 for the 4×3 and the 1×12 configuration. Thereby, the comparison of the cases with ($w_F \neq 0$) and without ($w_F = 0$) radial force compensation is included. The torque errors are in a similar range for both configurations with and without radial force compensation, and in comparison to the HC case, cf. Fig. 5.5 and Fig. 5.6, which proves the feasibility of the optimal current patterns and the proposed control strategy. This is due to the low current errors, especially at steady state. The differences occur in the resulting radial forces and power losses. In the 4×3 configuration, the radial force amplitudes are approximately 28% higher than in the 1×12 configuration without radial force compensation. However, the radial forces can be significantly

5.2 Control strategy results

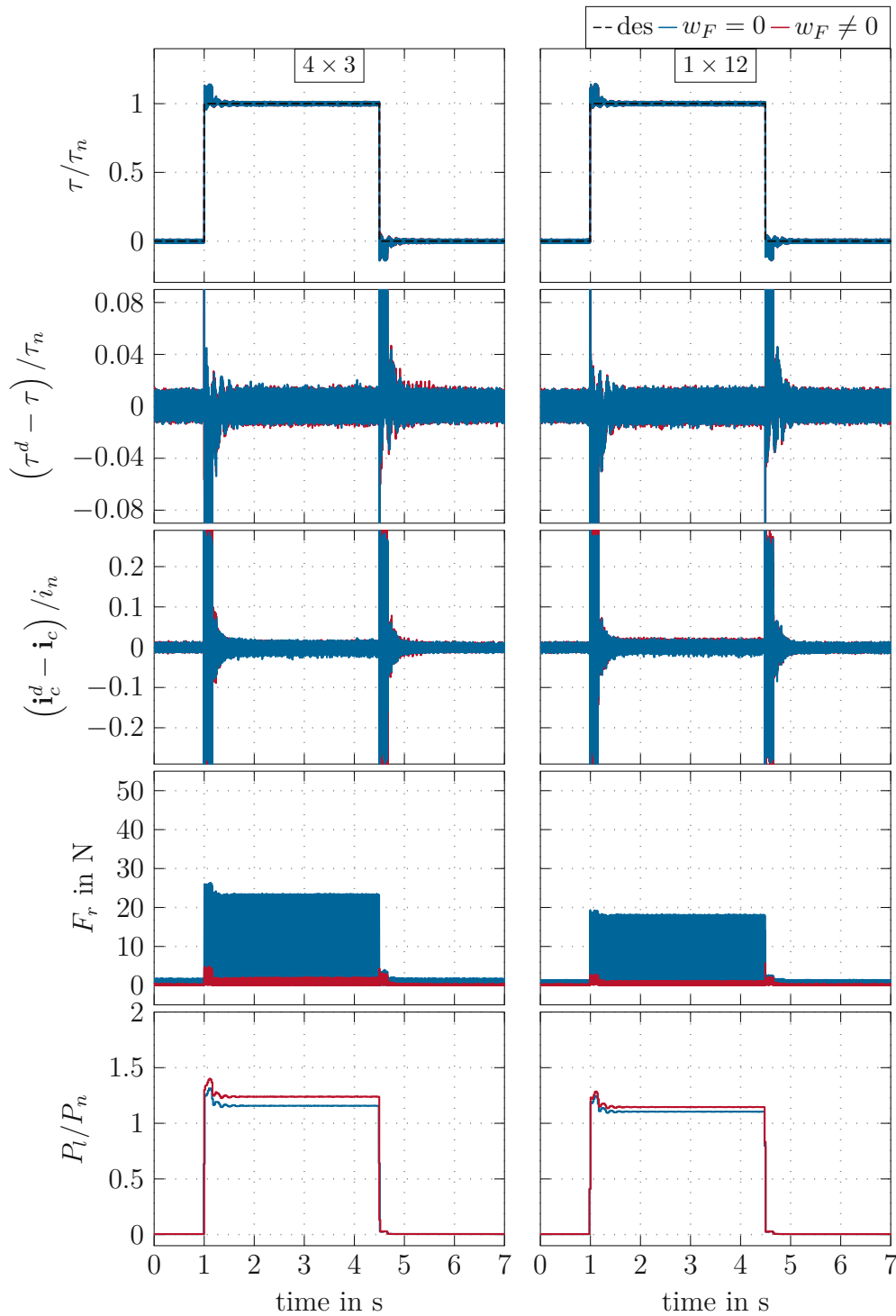


Figure 5.9: Measurement results for the single OC fault case of coil 1 in the 4×3 and the 1×12 configuration for uncompensated radial forces (blue) and with radial force compensation (red) at speed $n = 720$ rpm.

5 Fault-tolerant control

decreased with the FTC, including radial force compensation by over 90 % for both cases. The power losses are slightly higher for both configurations in the cases with radial force compensation. By comparing both configurations, it turns out that the power losses in the 1×12 configuration with radial force compensation are below the 4×3 configuration without radial force compensation.

Next, the double OC fault case of coils 1 and 4 is investigated for dynamic changes in the desired torque in Fig. 5.10. Results with ($w_F \neq 0$) and without ($w_F = 0$) radial force compensation are studied for both the 4×3 and the 1×12 configuration at high-speed operation $n = 720$ rpm. The torque errors and the current tracking accuracy are almost identical for the case with and without radial force compensation. Again, the torque error magnitude is in the same range as for the HC case, cf. Fig. 5.5 and Fig. 5.6. As expected, the radial forces are significantly higher than in the single OC case. This is attributed to the fact the electrical coil symmetry is given for coils 1, 4, 7, and 10, and by the failure of coils 1 and 4, only coils 7 and 10 are available for control. Moreover, a significant reduction of the radial forces by more than 60 % is achieved for the 4×3 configuration. The 1×12 configuration exhibits an even better result with a reduction of the radial forces by over 90 %. It is interesting to notice that the power losses of the motor P_l , see (4.3) are smaller for the 1×12 configuration than for the 4×3 configuration, although a similar high torque accuracy can be achieved. Also, the radial force compensation only requires a power loss increase of 14 % for the 1×12 configuration compared to 16 % for the 4×3 configuration.

Now, in Fig. 5.11, the double OC fault case of coil 3 and 4 is considered for the identical dynamic torque scenario at high speed of $n = 720$ rpm as in the previous scenarios. Again, the torque and current performance are similar to those of the HC case, cf. Fig. 5.5 and Fig. 5.6. The radial force amplitudes are between the single OC fault case and the double OC fault case of coils 1 and 4. The radial forces are reduced by a factor of over 85 % and 80 % for the 4×3 and the 1×12 configuration. In contrast to the OC fault case of coils 1 and 4, the radial forces amplitudes are equal for both configurations. Thereby, the power losses in the case with radial force compensation of the 1×12 configuration are lower than in the uncompensated case of the 4×3 configuration.

Finally, the triple OC fault case of the coil 1, 2, and 3 is investigated in Fig. 5.11 for the dynamic torque step at high speed of $n = 720$ rpm. Again, the torque and current error performances are similar to the previous scenarios. The results show similar performance for the radial forces and the power losses between the 4×3 and the 1×12 configuration. In contrast to the previous cases, the radial force oscillation amplitude is lower but includes a constant offset. The radial force compensation is with a reduction of about 90 % as effective as in the previous cases.

5.2 Control strategy results

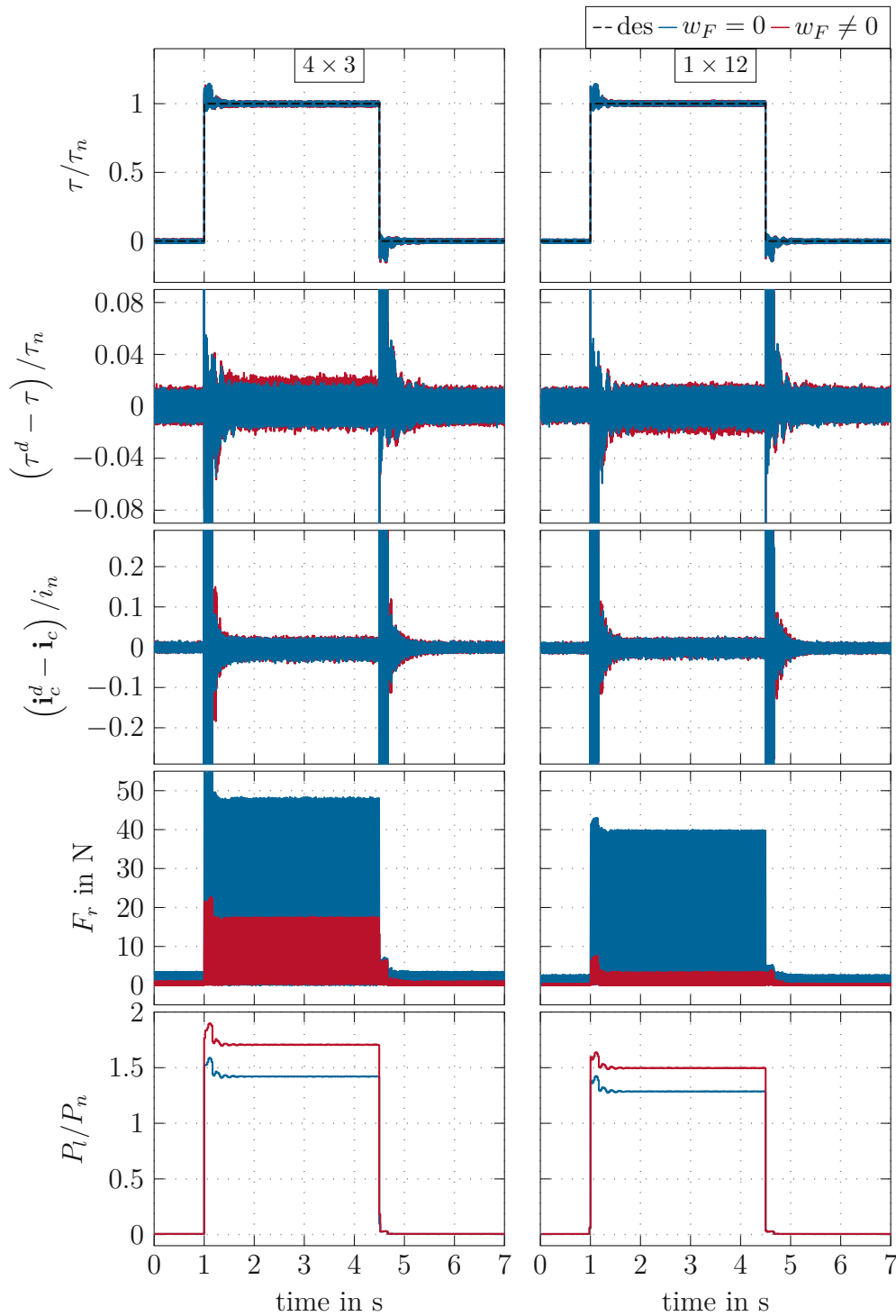


Figure 5.10: Measurement results for the double OC fault case of coils 1 and 4 in the 4×3 and the 1×12 configuration for uncompensated radial forces (blue) and with radial force compensation (red) at speed $n = 720$ rpm.

5 Fault-tolerant control

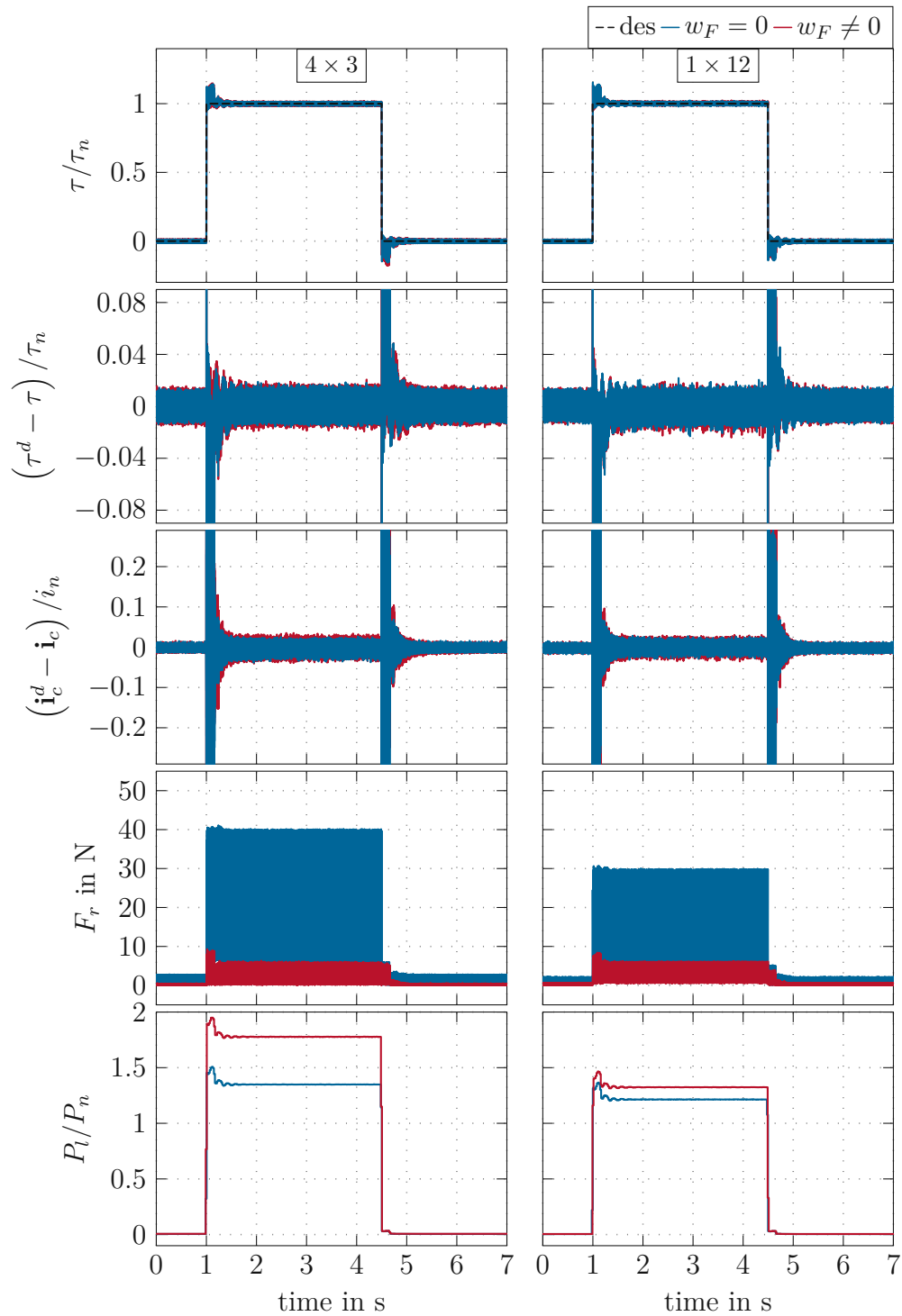


Figure 5.11: Measurement results for the double OC fault case of coils 3 and 4 in the 4×3 and the 1×12 configuration for uncompensated radial forces (blue) and with radial force compensation (red) at speed $n = 720$ rpm.

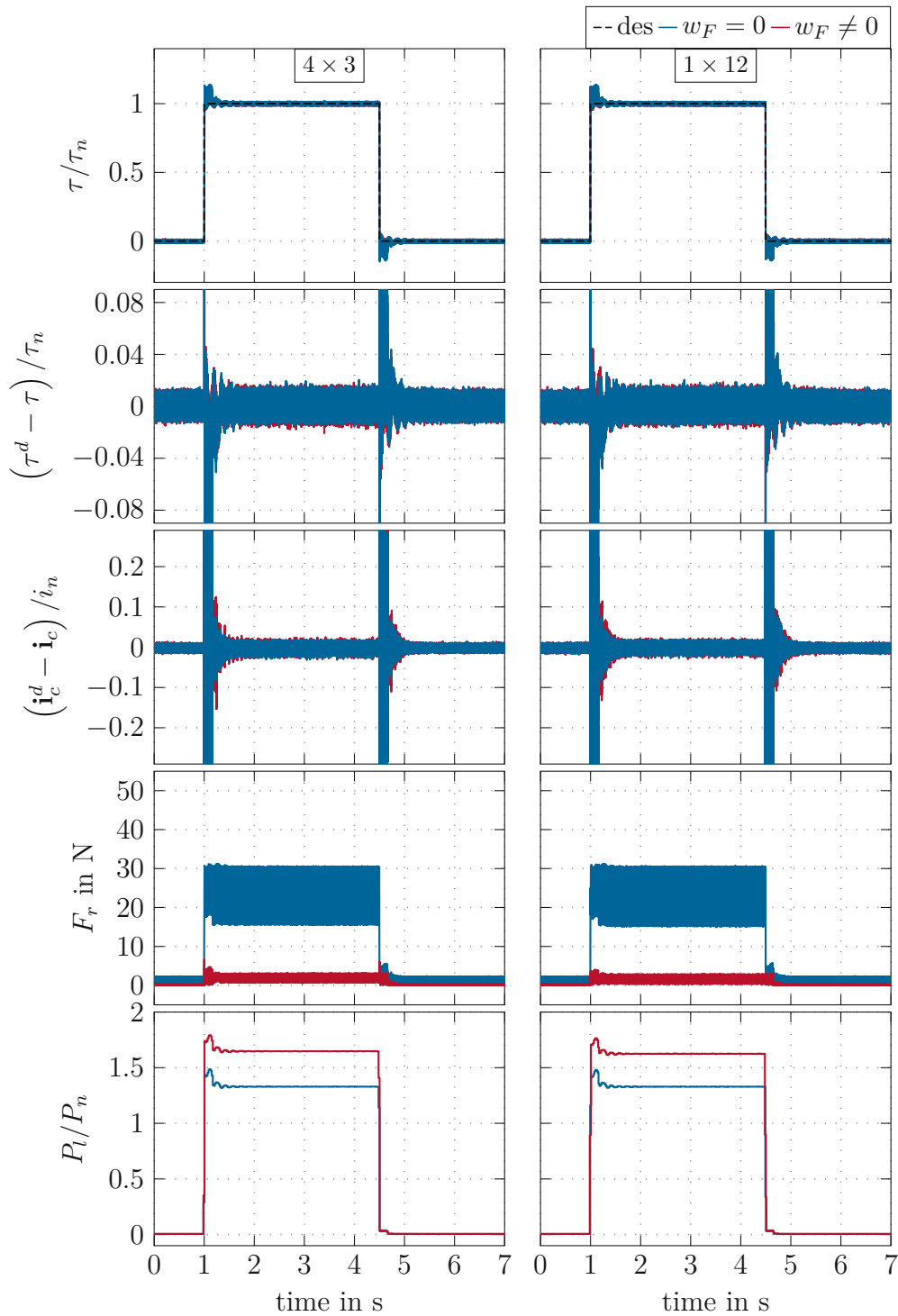


Figure 5.12: Measurement results for the triple OC fault case of coils 1, 2, and 3 in the 4×3 and the 1×12 configuration for uncompensated radial forces (blue) and with radial force compensation (red) at speed $n = 720$ rpm.

5 Fault-tolerant control

Overall, these results demonstrate the effectiveness of the proposed FTC strategy for radial force compensation under multiple OC faults. A significant performance gain can be achieved for the single and double OC faults by utilizing the 1×12 configuration due to the higher number of available DOFs compared to the 4×3 configuration while maintaining the low torque error. The performance in triple OC fault cases is almost identical for both configurations.

5.2.3 Performance comparison of 1×12 and 4×3 configuration

Finally, the performance of the 1×12 and 4×3 configurations is further compared for all considered fault cases. Measurements at $n = 720$ rpm are performed, and steady-state results for constant desired torques $\tau^d = [-1, -0.75, \dots, 1]\tau_n$ are considered. Four cases are studied: the uncompensated radial force case for the 4×3 and the 1×12 configuration and the case with radial force compensation for both configurations. The first important result of Fig. 5.13 is that the torque errors are of similar magnitude for the HC case and all OC fault cases. The single slightly higher torque errors in the 4×3 configuration with radial force compensation for the double OC fault of coils 1 and 4 result from the challenging optimization problem with high radial forces due to the magnetic field distribution. The second important result is that the radial forces for uncompensated and compensated cases are significantly lower in the 1×12 configuration than for the 4×3 case in almost all OC fault cases. The power losses are slightly higher for cases with radial force compensation than uncompensated cases in both configurations. Note that, except for the double OC fault case of coils 1 and 4 and the triple adjacent OC fault case of coils 1, 2, and 3, the power losses for the 1×12 configuration with radial force compensation are always below the losses of the uncompensated radial force cases in the 4×3 configuration. This can be attributed to the higher number of DOFs as the overall required current demand is distributed over more coils. As seen in the last plot, the loss of active coils in OC fault cases results in higher currents within the remaining coils. Similar to the power losses, the compensation of radial forces requires higher current amplitudes. The comparison between both configurations shows equal or lower maximum required currents in the 1×12 configuration.

In summary, the measurement results on the test bench lead to several conclusions. The proposed FTC strategy achieves results similar to the state-of-the-art PIR strategy in dynamic HC case scenarios. The advantages of the FTC strategy are given by its robustness in all OC fault cases and demonstrated by the low steady-state current errors of two times the current sensor noise amplitude. Measurements verify the achieved optimization results in Chapter 4 regarding the torque accuracy and radial force compensation in OC fault cases. The comprehensive comparison

5.2 Control strategy results

of all scenarios in the HC case and single up to triple adjacent OC fault cases between the 4×3 and the 1×12 configuration highlight the advantages of the higher DOFs for the latter configuration.

5 Fault-tolerant control

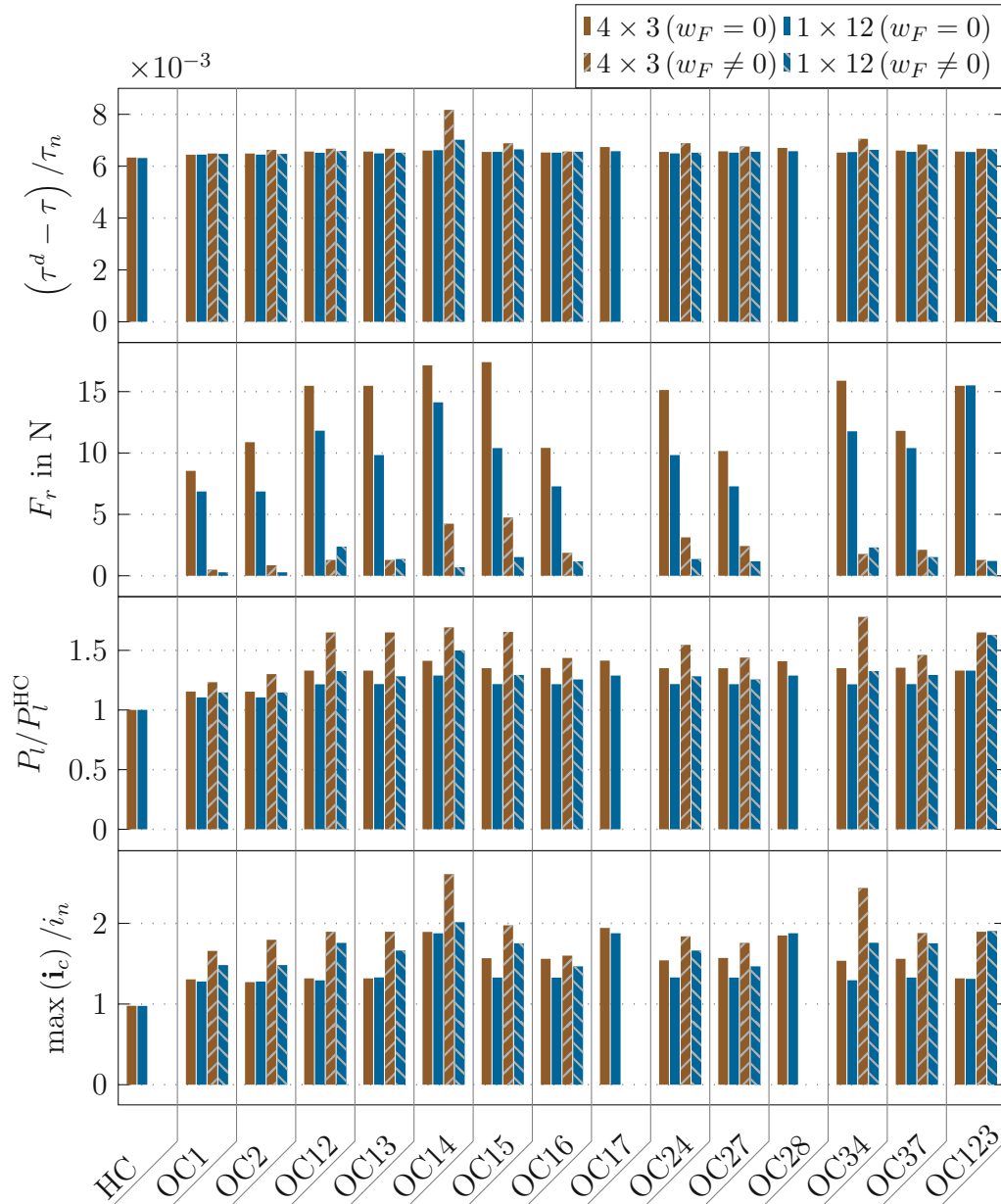


Figure 5.13: Overall comparison of the torque error, radial force, power losses, and maximum currents for the 4×3 and 1×12 configurations without and with radial force compensation.

6

Open-circuit fault diagnosis

Parts of this chapter were published in similar form in the author's previous publication [3].

In this chapter, the real-time fault diagnosis method is presented. The goal is to correctly diagnose multiple-phase open-circuit (OC) faults by only utilizing the phase current measurements, which include higher harmonic components. The derived time-domain signal-based fault diagnosis method combines the two common fault identifiers, the measurements of the phase currents and the phase control errors to meet the requirements a) - f) specified in Section 1.2. The proposed fault diagnosis method is derived in Section 6.1. In Section 6.2, the method is evaluated using the test stand, cf. Section 3.1, showing the immunity to false diagnosis and the diagnosis speed for up to triple simultaneous and sequential OC faults for both, the 4×3 and the 1×12 configuration.

6.1 Fault diagnosis method

In the case of an OC fault, the affected measured phase current i_f is zero, so only the sensor noise is measured from then on. Additionally, the desired current of this phase is unchanged, resulting in an unexpectedly large current error, which depends on the operating point. Separate diagnosis variables cover both phenomena. In the following, only the j -th coil is considered since the proposed method is independent of the number of phases n_c and the electrical coil configuration. The diagnosis variables at the time step k are given by

$$d_{j,k}^C = \frac{\langle |i_{j,k}| \rangle}{\hat{i}_{\bar{k}}} \quad (6.1)$$

6 Open-circuit fault diagnosis

for the current and

$$d_{j,k}^E = \frac{\langle |i_{j,k}^d - i_{j,k}| \rangle}{\hat{i}_{\bar{k}}} \quad (6.2)$$

for the current error, which is composed of the reference current $i_{j,k}^d$ and the phase current $i_{j,k}$. The robustness against different operating points is gained by averaging the absolute values

$$\langle |x_{j,k}| \rangle = \frac{1}{n_{avg}} \sum_{l=k-n_{avg}+1}^k |x_{j,l}|, \quad (6.3)$$

over n_{avg} points. In addition, the normalization over the maximum value of all n_c coil currents

$$\hat{i}_{\bar{k}} = \max_{1 \leq j \leq n_c, k-n_{avg}+1 \leq l \leq k} |i_{j,l}| \quad (6.4)$$

within the averaging interval is applied to achieve robustness against different current amplitudes.

The number of averaging points

$$n_{avg}(\omega_k) = \frac{1}{2} \frac{2\pi}{\omega_k n_p T_s} \quad (6.5)$$

is rounded towards the nearest integer value and chosen depending on the number of pole pairs n_p , the sampling time T_s , and the rotor speed ω_k . The rotor speed is assumed to be approximately constant over the last n_{avg} averaging points. Typically, the averaging is performed over a full current fundamental period (cfp) see, e.g., [68, 70, 74, 106]. As proposed in [67, 73, 76], shorter averaging intervals than a full cfp can be considered, which results in shorter detection times while decreasing robustness. However, the difference between positive and negative current periods, as required for switch OC faults, can be neglected for phase OC faults. This is considered in the proposed method by the absolute values in (6.1) and (6.2), together with averaging over half the cfp by the factor 1/2 in (6.5). This results in shorter detection times while maintaining the robustness due to averaging.

Both diagnosis variables (6.1) and (6.2) are strictly positive due to the averaging of the absolute values and the nonzero current sensor noise. The fault diagnosis variable $d_{j,k}^F$ is derived by combining both detection variables in the form

$$d_{j,k}^F = d_{j,k}^E - \alpha d_{j,k}^C \quad (6.6)$$

with $\alpha > 0$. An OC fault in the j -th phase is detected by a value $d_{j,k}^F > 0$. The fault identification is already included since the diagnosis variables are given individually for each phase.

In the case of perfect current tracking, i.e., $d_{j,k}^E = 0$, $d_{j,k}^F < 0$ is ensured by the negative sign of the current detection variable in (6.6). This is true for the healthy-circuit (HC) and all OC fault cases. In OC fault cases, the corresponding fault diagnosis variable is close to zero but does not exceed zero, which means that the fault detection cannot be triggered solely by the current diagnosis variable. In the event of an OC fault case, the current error is large. Therefore, the current error diagnosis variable $d_{j,k}^E \gg 0$ has a significant positive value. The robustness is guaranteed if $\alpha d_{j,k}^C \geq d_{j,k}^E$ holds for nominal operation. This can be set by a proper choice of α to avoid false diagnosis. In contrast to existing methods, where multiple variables or thresholds have to be set, e.g., [44, 68, 70, 76], the proposed method utilizes only α as a tunable parameter. For the investigated setup, $\alpha = 2$ is selected, which ensures immunity to false diagnosis in worst-case scenarios.

6.2 Fault diagnosis results

In this section, the transient fault occurrence is evaluated together with the effectiveness of the proposed fault diagnosis method by experiments on the test stand, cf. Section 3.1. The immunity to false alarms under load changes is presented, followed by diagnosis speed evaluation of different α values for a single OC fault case without mitigation. Finally, sequentially and simultaneously triple OC faults with fault mitigation for the 1×12 and the 4×3 configurations are studied.

6.2.1 Immunity to false diagnosis

The immunity to false diagnosis decisions is crucial for the reliability of the fault detection method. By analyzing the fault diagnosis variable (6.6), the worst-case scenario for the robustness of the fault diagnosis method is an instantaneous load change towards a low current amplitude. The sudden load change increases the current error and, consequently, the current error diagnosis variable. Additionally, low current amplitudes result in lower current diagnosis variables. Hence, the results of a torque step up to the nominal torque and back down to zero, performed for the HC case in the 1×12 configuration, are shown in Fig. 6.1. The left and right plot columns show the torque and the fault diagnosis variables for $\alpha = 2$ at a low speed of $n = 60$ rpm and a high speed of $n = 720$ rpm, respectively. Both experiments verify the immunity to false OC diagnosis under load steps. At low speed, the diagnosis variables are closer to zero after the second torque step because the iterative learning control (ILC) structure utilized within the fault-tolerant control (FTC) strategy requires one full mechanical rotation of the motor to significantly reduce the current error, cf. Section 5.1.4.

6 Open-circuit fault diagnosis

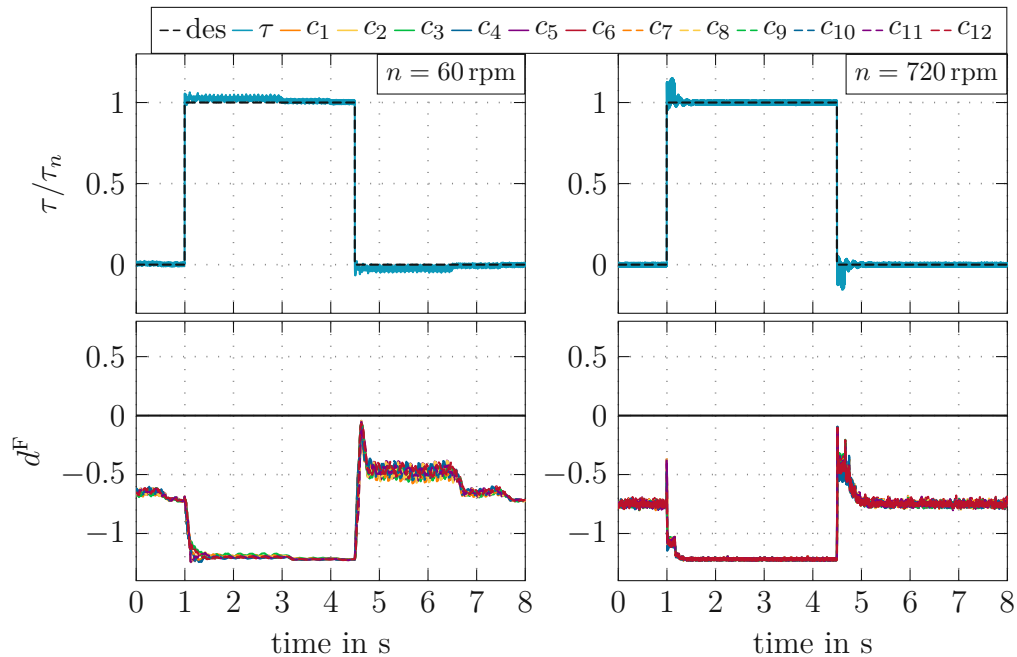


Figure 6.1: Fault diagnosis variables immunity to torque step changes in the 1×12 configuration at speeds $n = 60$ rpm on the left and $n = 720$ rpm at the right side.

6.2.2 Diagnosis speed of single open-circuit fault without mitigation

In the following the fault diagnosis performance is studied without fault mitigation at low speed in the 1×12 configuration, shown in Fig. 6.2. Thereby, the torque, the currents of the first three coils, the current errors, and the diagnosis variables are given in the plot rows. On top, the actual OC fault cases are indicated for the system and FTC strategy. The top rows show the actual OC fault case emulated on the PMSM and the applied FTC strategy. The numbers indicate an OC fault in the corresponding phase and the HC case is indicated with the $-$ symbol.

The first scenario investigates the sudden single OC fault of coil 1 at nominal torque causes a significant torque drop, which oscillates with twice the cfp, as depicted in the left plot column. As no fault mitigation is applied, the control strategy remains the same as for the HC case, and a large current error is visible for coil 1. The current errors for all remaining coil currents oscillate, attributed to the single neutral point and Kirchoff's current law for the 1×12 configuration. The diagnosis variables for $\alpha = 1, 2, 5, 10$ are depicted in the last plot. Larger values of α lead to longer diagnosis times and increase robustness since the steady-state diagnosis values are lower. However, with all values, the OC fault of coil 1 is correctly diagnosed within half of the cfp. With the chosen value $\alpha = 2$, the single

6.2 Fault diagnosis results

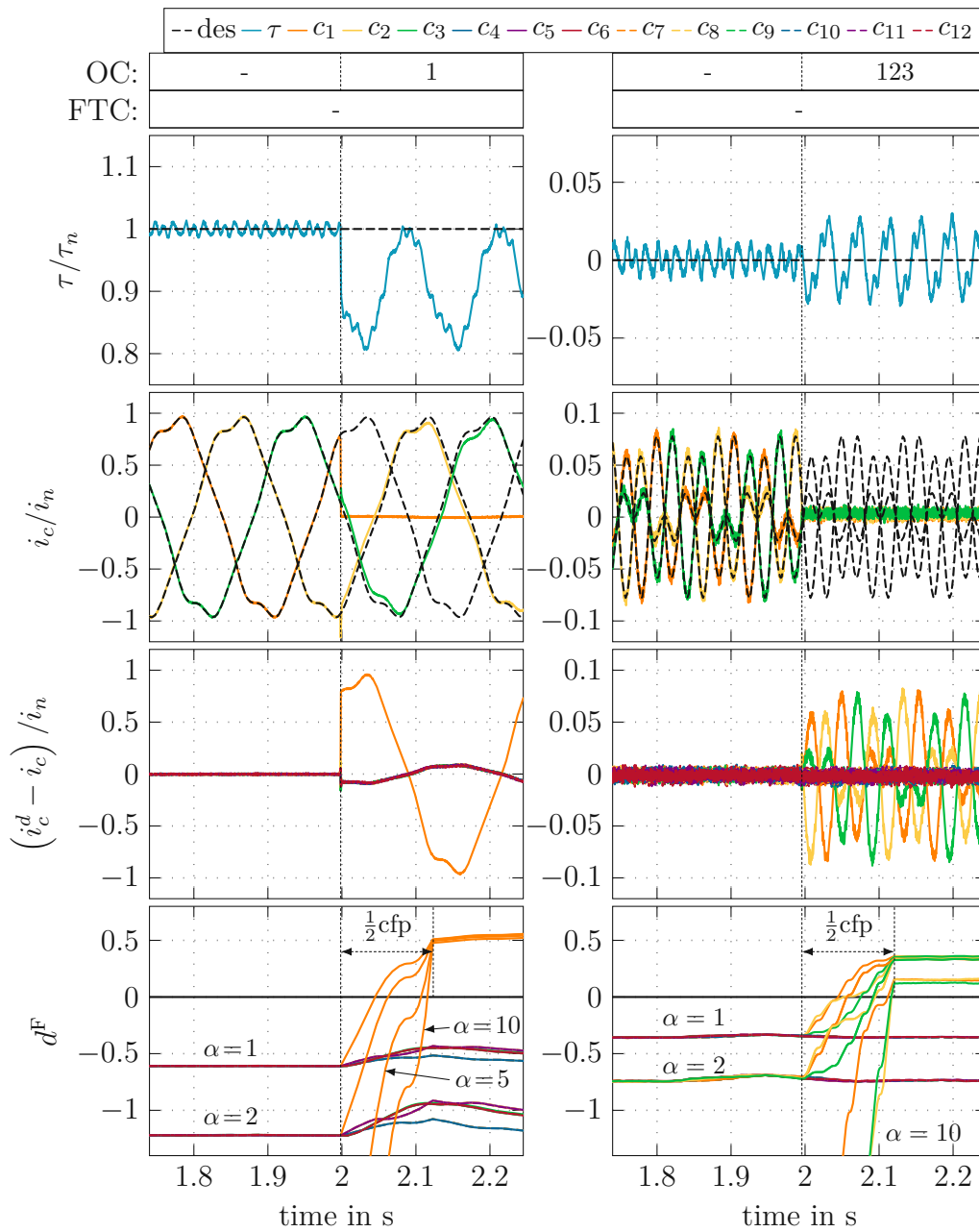


Figure 6.2: Fault diagnosis in the 1×12 configuration at speed $n = 60$ rpm for nominal desired torque on the left and zero desired torque on the right.

6 Open-circuit fault diagnosis

OC fault is diagnosed after 63.8 ms, corresponding to 25.52 % of the cfp. However, in this experiment, the FTC is not applied after the OC fault diagnosis.

The second scenario, depicted on the right plot column, investigates a simultaneous triple OC fault of coils 1, 2, and 3 at zero torque. This scenario is less severe in terms of the resulting torque error in post-fault situations but is supposed to be more challenging in terms of correct fault diagnosis. However, all three OC faults are identified correctly. As the moment in time for this sudden triple OC fault case is arbitrarily chosen, the diagnosis variables for the correspondent coils trigger at different times due to the different current amplitudes. For the chosen value $\alpha = 2$, the OC fault of coil 1 is fastest diagnosed within 24.28 %, followed by the OC fault of coil 3, which requires 38.44 %, and the OC fault case of coil 2, requiring 39.48 % of the cfp, respectively.

Both scenarios demonstrate the effectiveness of the fault diagnosis method and the required diagnosis times stay below half of the cfp.

6.2.3 Multiple open-circuit fault diagnosis and mitigation

In this section, the effectiveness of the fault diagnosis method is studied in combination with the fault mitigation achieved by the proposed FTC strategy without radial force compensation in Chapter 5. In Fig. 6.3, the evolution from the HC case to a triple OC fault case of coils 1, 2, and 3 is analyzed for the nominal torque at a high speed of $n = 720$ rpm in the 1×12 configuration. Thereby, the three columns in Fig. 6.3 correspond to the transition from the HC to the OC fault case of coil 1, followed by the double OC fault provoked by the additional sudden fault of coil 2, and the triple OC fault due to the fault of coil 3, respectively. The system and FTC states are given at the top. The OC fault times are chosen arbitrarily concerning the current amplitudes. The first OC fault in coil 1 is indicated by the first diagnosis variable, which triggers the FTC strategy to mitigate this OC fault and reduce the torque error. All other diagnosis variables are only slightly increased. Once an OC fault is diagnosed, this diagnosis variable is no longer considered. The steady state for this case is shown in the second plot column until the second OC fault is emulated. In addition, the proposed diagnosis method can reliably handle the second OC fault case without any adaptation. The second OC fault is diagnosed within coil 2, and only minor fluctuations in the remaining diagnosis variables are visible. The steady state for the double OC fault is given in the third plot column until the triple OC fault is emulated, where the successful OC fault diagnosis of coil 3 is depicted.

In Fig. 6.4, a simultaneous triple OC fault of coils 1, 2, and 3 is studied for zero torque at a high speed of $n = 720$ rpm in the 4×3 configuration. Due to the different relay delay times, the current in coil 3 is zero slightly before coils 1 and

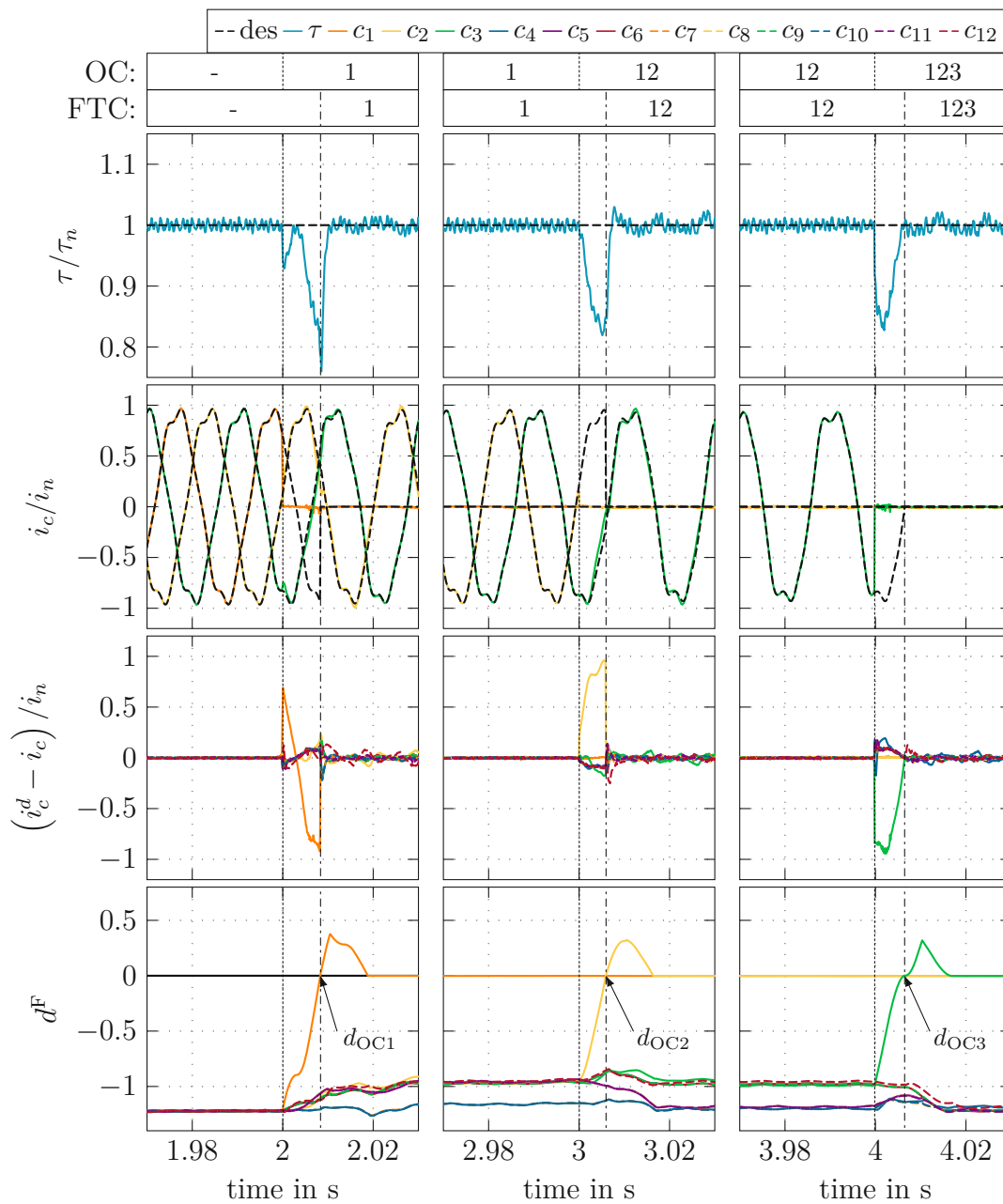


Figure 6.3: Fault diagnosis in the 1×12 configuration at speed $n = 720$ rpm for nominal desired torque. The three rows show the transition from the HC case to a triple OC fault case of coils 1-3 with fault mitigation through the FTC strategy according to the diagnosed fault cases.

6 Open-circuit fault diagnosis

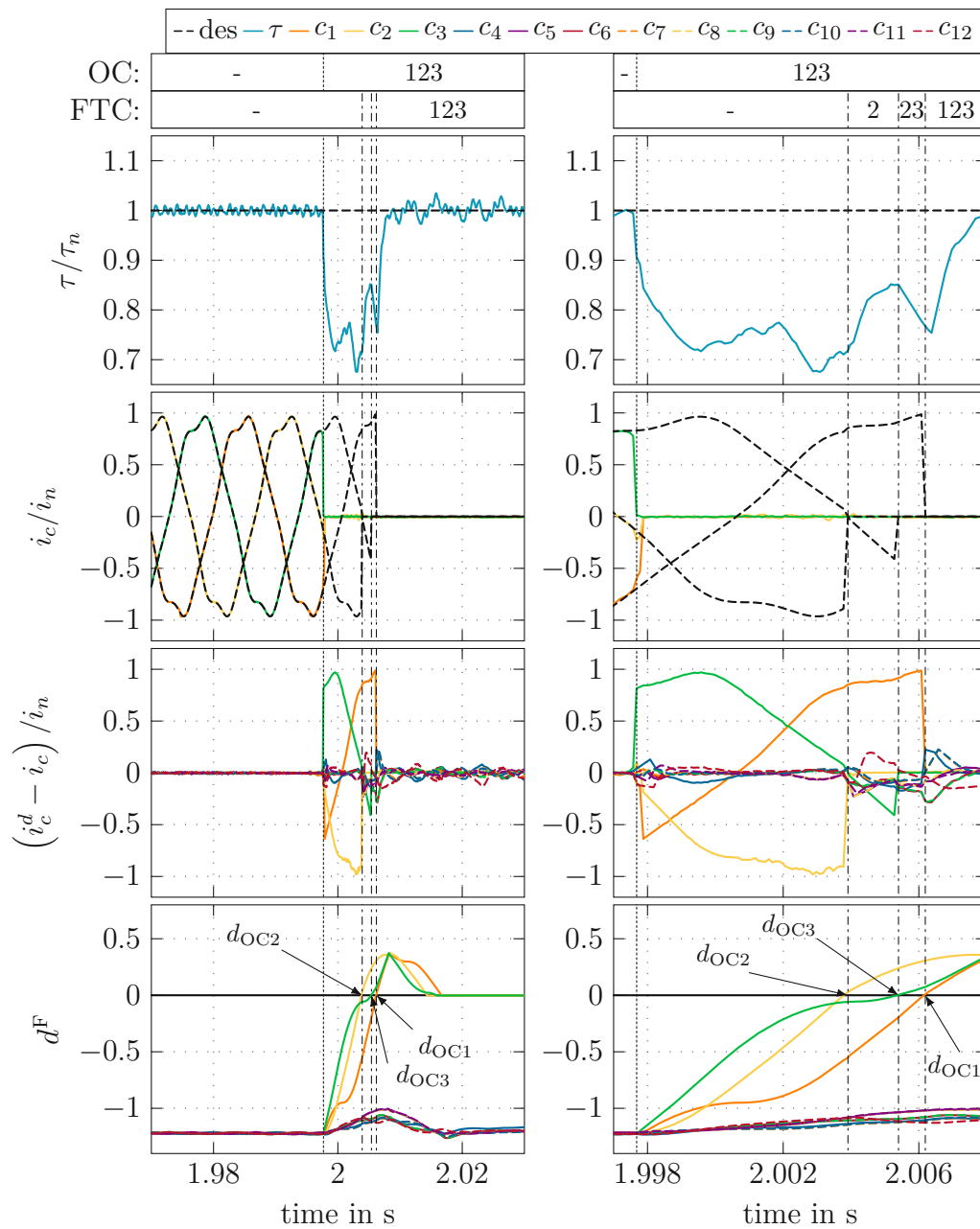


Figure 6.4: Fault diagnosis in the 1×12 configuration at speed $n = 720$ rpm for nominal desired torque for a simultaneously triple OC fault case of coil 1-3 with fault mitigation. The right plot columns are a scope of the left plot column.

2. As fewer DOFs are given for this configuration, cf. Tab. 4.1, only two DOFs are available for each three-phase system. Thus, a double OC fault results in an uncontrollable three-phase system. Hence, it is equal to a triple OC fault. All affected diagnosis variables are rising, and the OC fault of coil 1 is diagnosed first. This triggers the FTC strategy transition, and a single OC fault case for coil 1 is considered. However, the current errors for coils 2 and 3 are still rising until the second OC fault in coil 3 is diagnosed, which again triggers the FTC strategy. As a three-phase system with one coil is uncontrollable, detecting the second fault within the three-phase system equals a triple OC fault. Therefore, diagnosing the third OC fault in coil 2 has no consequences for the FTC strategy.

The diagnosis times and percentages of cfp are listed in Tab. 6.1 for different operating points at high speed $n = 720$ rpm, at low speed $n = 60$ rpm, and near standstill $n = 4$ rpm, each at nominal torque and zero torque for the 1×12 and the 4×3 configuration. The experiments near standstill highlight the effectiveness and robustness of the proposed diagnosis method even beyond the methods' design limits. Note again that the OC fault times are arbitrarily chosen concerning the current amplitudes. In all performed experiments, the emulated OC fault cases were correctly diagnosed below 41 % cfp, and no false diagnosis occurred. The gray background in Tab. 6.1 indicates the diagnosis times for the presented cases in Fig. 6.3 and Fig. 6.4.

The presented control strategy in Chapter 5 and the fault diagnosis method described in this chapter are implemented at a sampling time of $T_s = 100 \mu\text{s}$ on the dSpace DS1007 processing unit, cf. Section 3.1 and require approximately 2.3 MB of memory and about $80 \mu\text{s}$ for calculation. The focus is on real-time execution, which only partially includes hardware resource optimization.

6 Open-circuit fault diagnosis

Table 6.1: Multiple OC fault diagnosis times with fault mitigation in the 1×12 and the 4×3 configuration for different operating points. The percentage values indicate the diagnosis times in relation to the cfp.

Cases		1×12						4×3			
speed	τ/τ_n	HC to OC1		OC1 to OC12		OC12 to OC123		HC to OC1		OC1 to OC123	
Sequential triple OC											
720 rpm	1	8.33 ms	39.99%	5.92 ms	28.43%	6.62 ms	31.77%	7.33 ms	35.18%	7.42 ms	35.62%
720 rpm	0	8.23 ms	39.50%	7.82 ms	37.55%	5.62 ms	26.98%	5.33 ms	25.57%	8.32 ms	39.93%
60 rpm	1	88.53 ms	35.41%	60.92 ms	24.37%	93.83 ms	37.53%	69.32 ms	27.73%	69.4 ms	27.76%
60 rpm	0	101.93 ms	40.77%	82.92 ms	33.17%	62.81 ms	25.12%	64.32 ms	25.73%	64.4 ms	25.76%
4 rpm	1	135.74 ms	3.62%	137.52 ms	3.67%	116.32 ms	3.10%	127.32 ms	3.40%	127.5 ms	3.40%
4 rpm	0	167.54 ms	4.47%	149.12 ms	3.98%	86.32 ms	2.30%	131.22 ms	3.50%	132 ms	3.52%
Simultaneous triple OC											
speed	τ/τ_n	OC1		OC2		OC3		first OC		second OC	
720 rpm	1	8.32 ms	39.92%	6.03 ms	28.95%	7.62 ms	36.57%	5.53 ms	26.55%	7.32 ms	35.12%
720 rpm	0	5.23 ms	25.11%	8.02 ms	38.47%	7.62 ms	36.56%	5.33 ms	25.58%	7.72 ms	37.04%
60 rpm	1	62.04 ms	24.81%	97.32 ms	38.93%	93.92 ms	37.57%	56.84 ms	22.74%	86.12 ms	34.45%
60 rpm	0	75.12 ms	30.05%	57.84 ms	23.13%	97.12 ms	38.85%	67.14 ms	26.85%	82.12 ms	32.85%
4 rpm	1	149.33 ms	3.98%	106.54 ms	2.84%	137.83 ms	3.68%	72.44 ms	1.93%	133.73 ms	3.57%
4 rpm	0	93.14 ms	2.48%	104.83 ms	2.80%	120.92 ms	3.22%	65.64 ms	1.75%	77.92 ms	2.08%

7

Conclusion and outlook

A concept for fault-tolerant multiphase permanent magnet synchronous machines (PMSM) under multiple open-circuit faults was presented in this work. In particular, a fault diagnosis method and an optimal fault-tolerant control (FTC) strategy were developed and studied on a multiphase PMSM with twelve individually controllable single tooth coils. This flexibility allowed the performance comparison of different aspects of n-phase (twelve-phase 1×12 configuration with a single isolated neutral point) and multiple three-phase systems (quadruple three-phase 4×3 configuration with four isolated neutral points) in star interconnection regarding the available degrees of freedom (DOFs) under multiple OC fault cases. These higher DOFs, compared to classical three-phase drives, were beneficially exploited to reduce the occurring torque oscillations and the unbalanced radial forces, whose vibrations also stress the bearings.

A dynamic mathematical model was derived based on a nonlinear magnetic equivalent circuit (MEC) model, including the nonlinear effects such as cogging torque, magnetic saturation, and non-fundamental wave behavior of the PMSM, and provided equations for the radial forces. An approach for the electric circuit was developed that systematically considers different electric coil interconnections and multiple OC faults. The minimum state model was designed so that the reduced coil currents are physical meaningful and correspond to the available DOFs. This overall model was calibrated and validated through measurements on a test stand, and a high model accuracy was achieved in static and dynamic conditions. This model was utilized to calculate optimized currents by an optimization problem formulation that minimized the classic control goals of torque tracking error and power losses. In addition, the radial forces were minimized thanks to the higher number of available DOFs of the multiphase PMSM. The results demonstrated that the cogging torque was compensated entirely, and an accurate torque performance was given for static and dynamic scenarios in the healthy-circuit (HC) case and for a single OC fault case. Additionally, the included radial force com-

7 Conclusion and outlook

compensation achieved a radial force reduction by a factor of over 500. Fourier series approximation of the optimized currents ensured the real-time capability, and the Fourier coefficients were stored in lookup tables. Higher current harmonics of the fifth and seventh order and odd orders up to the ninth order were considered for the HC and all OC fault cases. The control task challenges arose from these higher harmonic components at higher speeds.

The FTC strategy, including a nonlinear feedforward part, a proportional-integral (PI) feedback control part, and an iterative learning control (ILC) concept, was developed. The ILC concept was introduced to mitigate the nonlinear behavior of the utilized voltage source inverter (VSI) and track the fast-changing reference currents due to the higher harmonics that were included as the bandwidth of the PI controller was limited. Advantageously, only the reduced currents of the available DOFs are controlled, which limits the changes within the FTC strategy for different OC fault cases. A proportional integral resonant (PIR) controller was implemented as a state-of-the-art controller for comparison with the proposed FTC strategy. Both control strategies were evaluated by measurements on the test stand. The HC case comparison of both control strategies showed their effectiveness under different dynamic conditions. At steady state, the achievable current errors for the PIR strategy are 30 times the current sensor noise amplitude. In contrast, the achievable current errors with the proposed FTC strategy are further reduced to twice the current sensor noise amplitude, demonstrating the high performance achievable with the proposed FTC strategy. In OC fault cases, the PIR strategy turned unstable at higher speeds and thus was excluded from further comparison. Single, double, and triple adjacent OC fault cases were analyzed in detail in post-fault situations by comparing the 4×3 configuration with the 1×12 configuration, each with and without radial force compensation. The results show similar torque tracking errors in all cases and for both configurations. By including the radial force compensation, occurring radial forces were reduced between more than 60 % to over 90 %, depending on the considered OC fault case. This highlights the effectiveness of the introduced radial force compensation. The resulting power losses are increased due to higher current amplitudes. The higher number of available DOFs in the 1×12 configuration compared to the 4×3 configuration led to decreased power losses for all considered OC fault cases. Thus, this comparison reveals the benefits in OC fault cases of the 1×12 configuration over the 4×3 configuration while utilizing equal components.

Finally, a reliable and real-time fault diagnosis procedure was developed based solely on the current measurement signals already used for the control. This method was tailored to yield fast diagnosis results with higher harmonic components within the measurement signals. No additional sensor or prior knowledge about the electrical interconnection were required. Measurements on the test stand

proved the immunity to false diagnosis under load changes; only one tuning parameter was required. The diagnosis speed was investigated in detail for sequential and simultaneous triple OC faults in different operating points for both the 4×3 and the 1×12 configuration. All emulated OC fault cases were correctly diagnosed without false detection under 41 % of the current fundamental period.

Thus, the presented closed-loop fault-tolerant concept for diagnosing and mitigating the disadvantageous effects of multiple OC fault cases was successfully investigated in this work.

The proposed framework for multiphase PMSM enables several possibilities for further research and application topics. In future work, the investigated setup can be utilized to investigate different electric coil configurations, e.g., the frequently used double three-phase configuration. Furthermore, the field weakening operation can be investigated to achieve higher rotational speeds. Research towards a real-time current optimization solution would enable changing the weighting between the control goals online. Regarding possible fault cases, an extension of the fault diagnosis method would be beneficial to monitor different fault sources. As a first step, if redundant current sensors are integrated, the derived fault diagnosis method can be applied to detect current sensor faults. Furthermore, a fault diagnosis method could be integrated for detecting further sensor faults, i.e., sensors for dc-link voltages and rotational encoder. Sensorless control in a rotational encoder fault might be an interesting research topic, especially concerning the available DOFs of multiphase machines.

A

Appendix

A.1 Resonant controller

In this appendix, the resonant (R) controller is derived, and the equivalence of (5.29) and (5.30) is shown. The transfer function of an R controller for the h -harmonic component is given by

$$G_h^R(s) = \frac{K_h^R s}{s^2 + \omega_h^2}, \quad (\text{A.1})$$

with the controller gain K_h^R and the frequency expressed by $\omega_h = hn_p\omega$ [103]. A state-space representation is given analogously to [103] by

$$\frac{d}{dt} \mathbf{x}_h = \begin{bmatrix} 0 & -\omega_h \\ \omega_h & 0 \end{bmatrix} \mathbf{x}_h + \begin{bmatrix} 1 \\ 0 \end{bmatrix} e_{r,j} \quad (\text{A.2a})$$

$$y_h = \begin{bmatrix} K_h^R & 0 \end{bmatrix} \mathbf{x}_h, \quad (\text{A.2b})$$

for the j -th reduced current error $e_{r,j}$ as input, which is equation (5.29). The states $\mathbf{x}_h = [x_{1,j}, x_{2,j}]^T$ are chosen to

$$x_{1,j} = \frac{1}{K_h^R} (c_{h,j}^R \cos(\varphi_h) + s_{h,j}^R \sin(\varphi_h)) \quad (\text{A.3a})$$

$$x_{2,j} = \frac{1}{K_h^R} (-s_{h,j}^R \cos(\varphi_h) + c_{h,j}^R \sin(\varphi_h)), \quad (\text{A.3b})$$

with the time dependent cosine and sine coefficients $c_{h,j}^R$ and $s_{h,j}^R$, respectively, and $\varphi_h = hn_p\varphi$ including the time dependent rotor position φ . By inserting (A.3) into

A Appendix

(A.2) with $\frac{d}{dt}\varphi_h = \omega_h$ yields

$$\begin{aligned} & \left(\frac{d}{dt} c_{h,j}^R \right) \cos(\varphi_h) - c_{h,j}^R \omega_h \sin(\varphi_h) + \left(\frac{d}{dt} s_{h,j}^R \right) \sin(\varphi_h) + s_{h,j}^R \omega_h \cos(\varphi_h) \\ & = -\omega_h \left(-s_{h,j}^R \cos(\varphi_h) + c_{h,j}^R \sin(\varphi_h) \right) + K_h^R e_{r,j} \end{aligned} \quad (\text{A.4a})$$

$$\begin{aligned} & - \left(\frac{d}{dt} s_{h,j}^R \right) \cos(\varphi_h) + s_{h,j}^R \omega_h \sin(\varphi_h) + \left(\frac{d}{dt} c_{h,j}^R \right) \sin(\varphi_h) + c_{h,j}^R \omega_h \cos(\varphi_h) \\ & = \omega_h \left(c_{h,j}^R \cos(\varphi_h) + s_{h,j}^R \sin(\varphi_h) \right) . \end{aligned} \quad (\text{A.4b})$$

Thereby, the non-derivative terms of cosine and sine coefficients are canceling each other out, giving

$$\cos(\varphi_h) \frac{d}{dt} c_{h,j}^R + \sin(\varphi_h) \frac{d}{dt} s_{h,j}^R = K_h^R e_{r,j} \quad (\text{A.5a})$$

$$\sin(\varphi_h) \frac{d}{dt} c_{h,j}^R - \cos(\varphi_h) \frac{d}{dt} s_{h,j}^R = 0 . \quad (\text{A.5b})$$

Rearranging these equations together with (A.3) applied to the output $y_h = v_{c,r,h,j}^R$ in (A.2b) lead to the proposed R controller for the j -th reduced coil given by

$$\frac{d}{dt} c_{h,j}^R = K_h^R \cos(\varphi_h) e_{r,j} \quad (\text{A.6a})$$

$$\frac{d}{dt} s_{h,j}^R = K_h^R \sin(\varphi_h) e_{r,j} \quad (\text{A.6b})$$

$$v_{c,r,h,j}^R = c_{h,j}^R \cos(\varphi_h) + s_{h,j}^R \sin(\varphi_h) . \quad (\text{A.6c})$$

This directly proves the equivalence of (5.30) and (5.29) as the R controller is designed for each reduced coil individually.

Bibliography

- [1] R. Lenz, A. Kugi, and W. Kemmetmüller, “Optimal torque control with radial force compensation for multiphase PMSMs under an open-circuit fault”, *IFAC-PapersOnLine*, vol. 56, no. 2, pp. 4412–4417, 2023. DOI: 10.1016/j.ifacol.2023.10.1828.
- [2] R. Lenz, A. Deutschmann-Olek, A. Kugi, and W. Kemmetmüller, “Optimal fault-tolerant control with radial force compensation for multiple open-circuit faults in multiphase PMSMs - A comparison of n-phase and multiple three-phase systems”, *Control Engineering Practice*, vol. 147, pp. 105 924, 2024. DOI: 10.1016/j.conengprac.2024.105924.
- [3] R. Lenz, A. Kugi, and W. Kemmetmüller, “Online fault diagnosis for multiple open-circuit faults in multiphase drives with current harmonics”, in *26th International Conference for Electrical Machines ICEM*, Torino, Italy, 2024, (accepted).
- [4] T. Orlowska-Kowalska *et al.*, “Fault Diagnosis and Fault-Tolerant Control of PMSM Drives—State of the Art and Future Challenges”, *IEEE Access*, vol. 10, pp. 59 979–60 024, 2022. DOI: 10.1109/ACCESS.2022.3180153.
- [5] A. G. Yepes, O. Lopez, I. Gonzalez-Prieto, M. J. Duran, and J. Doval-Gandoy, “A Comprehensive Survey on Fault Tolerance in Multiphase AC Drives, Part 1: General Overview Considering Multiple Fault Types”, *Machines*, vol. 10, no. 3, pp. 208, 2022. DOI: 10.3390/machines10030208.
- [6] E. Levi, “Advances in Converter Control and Innovative Exploitation of Additional Degrees of Freedom for Multiphase Machines”, *IEEE Transactions on Industrial Electronics*, vol. 63, no. 1, pp. 433–448, 2016. DOI: 10.1109/TIE.2015.2434999.
- [7] C. Huang, F. Naghdy, H. Du, and H. Huang, “Fault tolerant steer-by-wire systems: An overview”, *Annual Reviews in Control*, vol. 47, pp. 98–111, 2019. DOI: 10.1016/j.arcontrol.2019.04.001.

Bibliography

- [8] F. P. Pop, R. Mircea, A.-C. Pop, R. Martis, and C. Martis, “Comparative Analysis for an Electric Power Steering System”, in *2018 XIII International Conference on Electrical Machines (ICEM)*, Alexandroupoli, Greece, 2018, pp. 590–596. DOI: 10.1109/ICELMACH.2018.8507038.
- [9] E. A. Bhuiyan *et al.*, “A Survey on Fault Diagnosis and Fault Tolerant Methodologies for Permanent Magnet Synchronous Machines”, *International Journal of Automation and Computing*, vol. 17, no. 6, pp. 763–787, 2020. DOI: 10.1007/s11633-020-1250-3.
- [10] A. G. Yepes, I. Gonzalez-Prieto, O. Lopez, M. J. Duran, and J. Doval-Gandoy, “A Comprehensive Survey on Fault Tolerance in Multiphase AC Drives, Part 2: Phase and Switch Open-Circuit Faults”, *Machines*, vol. 10, no. 3, 221, 2022. DOI: 10.3390/machines10030221.
- [11] M. Blanke, C. W. Frei, F. Kraus, J. Ron Patton, and M. Staroswiecki, “What is Fault-Tolerant Control?”, *IFAC Proceedings Volumes*, vol. 33, no. 11, pp. 41–52, 2000. DOI: 10.1016/S1474-6670(17)37338-X.
- [12] R. Isermann, R. Schwarz, and S. Stölzl, “Fault-Tolerant Drive-by-Wire Systems – Concepts and Realizations –”, *IFAC Proceedings Volumes*, vol. 33, no. 11, pp. 1–15, 2000. DOI: 10.1016/S1474-6670(17)37335-4.
- [13] E. Levi, F. Barrero, and M. J. Duran, “Multiphase machines and drives - Revisited”, *IEEE Transactions on Industrial Electronics*, vol. 63, no. 1, pp. 429–432, 2016. DOI: 10.1109/TIE.2015.2493510.
- [14] M. J. Duran and F. Barrero, “Recent Advances in the Design, Modeling, and Control of Multiphase Machines—Part II”, *IEEE Transactions on Industrial Electronics*, vol. 63, no. 1, pp. 459–468, 2016. DOI: 10.1109/TIE.2015.2448211.
- [15] F. Barrero and M. J. Duran, “Recent Advances in the Design, Modeling, and Control of Multiphase Machines—Part I”, *IEEE Transactions on Industrial Electronics*, vol. 63, no. 1, pp. 449–458, 2016. DOI: 10.1109/TIE.2015.2447733.
- [16] S. Choi *et al.*, “Fault Diagnosis Techniques for Permanent Magnet AC Machine and Drives—A Review of Current State of the Art”, *IEEE Transactions on Transportation Electrification*, vol. 4, no. 2, pp. 444–463, 2018. DOI: 10.1109/TTE.2018.2819627.
- [17] A. J. M. Cardoso, Ed., *Diagnosis and Fault Tolerance of Electrical Machines, Power Electronics and Drives*. Stevenage, UK: Institution of Engineering and Technology, 2018. DOI: 10.1049/PBP0126E.

- [18] W. Zhang, D. Xu, P. N. Enjeti, H. Li, J. T. Hawke, and H. S. Krishnamoorthy, “Survey on Fault-Tolerant Techniques for Power Electronic Converters”, *IEEE Transactions on Power Electronics*, vol. 29, no. 12, pp. 6319–6331, 2014. DOI: 10.1109/TPEL.2014.2304561.
- [19] G. Feng, C. Lai, W. Li, J. Tjong, and N. C. Kar, “Open-Phase Fault Modeling and Optimized Fault-Tolerant Control of Dual Three-Phase Permanent Magnet Synchronous Machines”, *IEEE Transactions on Power Electronics*, vol. 34, no. 11, pp. 11116–11127, 2019. DOI: 10.1109/TPEL.2019.2900599.
- [20] G. Feng, Y. Lu, C. Lai, B. Ding, and N. C. Kar, “Fault Tolerant Maximum Torque Per Ampere (FT-MTPA) Control for Dual Three-Phase Interior PMSMs Under Open-Phase Fault”, *IEEE Transactions on Industrial Electronics*, vol. 69, no. 12, pp. 12030–12041, 2022. DOI: 10.1109/TIE.2022.3142404.
- [21] P. Zheng, F. Wu, Y. Sui, P. Wang, Y. Lei, and H. Wang, “Harmonic Analysis and Fault-Tolerant Capability of a Semi-12-Phase Permanent-Magnet Synchronous Machine Used for EVs”, *Energies*, vol. 5, no. 9, pp. 3586–3607, 2012. DOI: 10.3390/en5093586.
- [22] F. Magnussen and H. Lendenmann, “Parasitic Effects in PM Machines With Concentrated Windings”, *IEEE Transactions on Industry Applications*, vol. 43, no. 5, pp. 1223–1232, 2007. DOI: 10.1109/TIA.2007.904400.
- [23] Z. Song, Y. Pei, Y. Li, S. Li, and F. Chai, “Analysis of Vibration in Modular Fault-tolerant PMSM under One-phase Open-circuit Fault”, in *2018 XIII International Conference on Electrical Machines (ICEM)*, Alexandroupoli, Greece, 2018, pp. 2565–2571. DOI: 10.1109/ICELMACH.2018.8507125.
- [24] P. Song, W. Li, Z. Li, and N. C. Kar, “Comparative Analysis of Noise and Vibration for Dual Three-phase IPMSM under Healthy and Multi-phase Open-circuit Fault Operations”, *IEEE Transactions on Magnetics*, vol. 59, no. 11, pp. 1–7, 2023. DOI: 10.1109/TMAG.2023.3288831.
- [25] G. Sala, D. Gerada, C. Gerada, and A. Tani, “Radial force control for triple three-phase sectorized SPM machines. Part II: Open winding fault tolerant control”, in *2017 Workshop on Electrical Machines Design, Control and Diagnosis (WEMDCD)*, Nottingham, UK, 2017, pp. 275–280. DOI: 10.1109/WEMDCD.2017.7947759.
- [26] R. Krishnan, *Permanent Magnet Synchronous and Brushless DC Motor Drives*, 1st ed. Boca Raton, FL, USA: CRC Press, 2010. DOI: 10.1201/9781420014235.

Bibliography

- [27] E. Strangas, G. Clerc, H. Razik, and A. Soualhi, *Fault Diagnosis, Prognosis, and Reliability for Electrical Drives: Fault Diagnosis, Failure Prognosis and Their Effects on the Reliability of Electrical Machines, Drives and Power Electronics*, 1st ed. Hoboken, NJ, USA: John Wiley & Sons, 2022.
- [28] J. Lannoo, D. Vanoost, J. Peuteman, S. Debruyne, H. De Gersem, and D. Pissoort, “Improved air gap permeance model to characterise the transient behaviour of electrical machines using MAGNETIC EQUIVALENT CIRCUIT method”, *International Journal of Numerical Modelling: Electronic Networks, Devices and Fields*, vol. 33, no. 5, pp. 2749, 2020. DOI: 10.1002/jnm.2749.
- [29] E. Levi, “Multiphase Electric Machines for Variable-Speed Applications”, *IEEE Transactions on Industrial Electronics*, vol. 55, no. 5, pp. 1893–1909, 2008. DOI: 10.1109/TIE.2008.918488.
- [30] F. Baudart, B. Dehez, E. Matagne, D. Telteu-Nedelcu, P. Alexandre, and F. Labrique, “Torque Control Strategy of Polyphase Permanent-Magnet Synchronous Machines With Minimal Controller Reconfiguration Under Open-Circuit Fault of One Phase”, *IEEE Transactions on Industrial Electronics*, vol. 59, no. 6, pp. 2632–2644, 2012. DOI: 10.1109/TIE.2011.2170393.
- [31] J. Pyrhönen, T. Jokinen, and V. Hrabovcová, *Design of Rotating Electrical Machines*, 2nd ed. Chichester, UK: John Wiley & Sons, 2014. DOI: 10.1002/9781118701591.
- [32] G. Bramerdorfer, W. Amrhein, and S. Lanser, “PMSM for high demands on low torque ripple using optimized stator phase currents controlled by an iterative learning control algorithm”, in *2013 - 39th Annual Conference of the IEEE Industrial Electronics Society*, Vienna, Austria, 2013, pp. 8488–8493. DOI: 10.1109/IECON.2013.6700557.
- [33] G. Bramerdorfer and W. Amrhein, “Optimization of PMSMs Considering Multi-Harmonic Current Waveforms: Theory, Design Aspects, and Experimental Verification”, *IEEE Transactions on Industry Applications*, vol. 59, no. 1, pp. 834–844, 2023. DOI: 10.1109/TIA.2022.3217241.
- [34] O. Dieterle and T. Greiner, “Decentralized Control of a Twelve-Phase PMSM”, in *PCIM Europe 2018; International Exhibition and Conference for Power Electronics, Intelligent Motion, Renewable Energy and Energy Management*, Nuremberg, Germany, 2018, pp. 1–8.
- [35] J. Huang, Y. Sui, Z. Yuan, S. Yang, and P. Zheng, “Equal-Magnitude Sinusoidal Current Fault-Tolerant Strategy Derived from Rotating Rhombus Method for Six-Phase PMSM with Open-Circuit Fault”, in *2022 25th Inter-*

- national Conference on Electrical Machines and Systems (ICEMS)*, Chiang Mai, Thailand, 2022, pp. 1–6. DOI: 10.1109/ICEMS56177.2022.9983282.
- [36] W. Kemmetmüller, D. Faustner, and A. Kugi, “Modeling of a Permanent Magnet Synchronous Machine With Internal Magnets Using Magnetic Equivalent Circuits”, *IEEE Transactions on Magnetics*, vol. 50, no. 6, pp. 1–14, 2014. DOI: 10.1109/TMAG.2014.2299238.
- [37] W. Kemmetmüller, T. Hausberger, and A. Kugi, “Optimal torque control of PMSMs with redundant stator coils in case of open circuit faults”, in *2017 IEEE International Conference on Advanced Intelligent Mechatronics (AIM)*, Munich, Germany, 2017, pp. 969–974. DOI: 10.1109/AIM.2017.8014144.
- [38] S. Koschik, F. Adler, D. Szepanski, and R. W. De Doncker, “Scalable FPGA and DSP based control for multiphase concentrated winding permanent magnet machines with single coil integrated inverters”, in *2015 IEEE International Electric Machines & Drives Conference (IEMDC)*, Coeur d’Alene, ID, USA, 2015, pp. 1515–1521. DOI: 10.1109/IEMDC.2015.7409263.
- [39] B. Sen and J. Wang, “Stationary Frame Fault-Tolerant Current Control of Polyphase Permanent-Magnet Machines under Open-Circuit and Short-Circuit Faults”, *IEEE Transactions on Power Electronics*, vol. 31, no. 7, pp. 4684–4696, 2015. DOI: 10.1109/TPEL.2015.2478337.
- [40] A. A. Rockhill and T. A. Lipo, “A generalized transformation methodology for polyphase electric machines and networks”, in *2015 IEEE International Electric Machines & Drives Conference (IEMDC)*, Coeur d’Alene, ID, USA, 2015, pp. 27–34. DOI: 10.1109/IEMDC.2015.7409032.
- [41] M. Janaszek, “Extended Clarke Transformation For n-Phase Systems”, *Proceedings of Electrotechnical Institute*, vol. 63, no. 274, pp. 5–26, 2016. DOI: 10.5604/01.3001.0009.4333.
- [42] M.-A. Shamsi-Nejad, B. Nahid-Mobarakeh, S. Pierfederici, and F. Meibody-Tabar, “Fault Tolerant and Minimum Loss Control of Double-Star Synchronous Machines Under Open Phase Conditions”, *IEEE Transactions on Industrial Electronics*, vol. 55, no. 5, pp. 1956–1965, 2008. DOI: 10.1109/TIE.2008.918485.
- [43] W. Wang, J. Zhang, M. Cheng, and S. Li, “Fault-Tolerant Control of Dual Three-Phase Permanent-Magnet Synchronous Machine Drives Under Open-Phase Faults”, *IEEE Transactions on Power Electronics*, vol. 32, no. 3, pp. 2052–2063, 2017. DOI: 10.1109/TPEL.2016.2559498.

Bibliography

- [44] Z. Wen, G. Valente, A. Formentini, L. Papini, C. Gerada, and P. Zanchetta, “Open-Circuit Fault Control Techniques for Bearingless Multisector Permanent Magnet Synchronous Machines”, *IEEE Transactions on Industry Applications*, vol. 57, no. 3, pp. 2527–2536, 2021. DOI: 10.1109/TIA.2021.3060368.
- [45] M. Barcaro, N. Bianchi, and F. Magnussen, “Analysis and Tests of a Dual Three-Phase 12-Slot 10-Pole Permanent-Magnet Motor”, *IEEE Transactions on Industry Applications*, vol. 46, no. 6, pp. 2355–2362, 2010. DOI: 10.1109/TIA.2010.2070784.
- [46] S. H. Shah, X. Wang, U. Abubakar, and P. Gao, “Analysis of the Radial Component of Electromagnetic Force Density and Vibration Behavior of an IPMSM With Multiple Three-Phase Winding Units”, in *2021 IEEE Industrial Electronics and Applications Conference (IEACon)*, Penang, Malaysia, 2021, pp. 246–251. DOI: 10.1109/IEACon51066.2021.9654698.
- [47] A. Abdul Rahman *et al.*, “Open and Short Circuit Post-Fault Control Strategies for Multi-Three-Phase Interior Permanent Magnet Machines”, *IEEE Transactions on Energy Conversion*, vol. 37, no. 1, pp. 163–174, 2022. DOI: 10.1109/TEC.2021.3090982.
- [48] G. Sala, G. Valente, D. Gerada, P. Zanchetta, and C. Gerada, “Post-Fault Operation of Bearingless Multisector SPM Machines by Space Vector Control”, *IEEE Transactions on Power Electronics*, vol. 35, no. 4, pp. 4168–4177, 2020. DOI: 10.1109/TPEL.2019.2933922.
- [49] S. Rubino, O. Dordevic, R. Bojoi, and E. Levi, “Modular Vector Control of Multi-Three-Phase Permanent Magnet Synchronous Motors”, *IEEE Transactions on Industrial Electronics*, vol. 68, no. 10, pp. 9136–9147, 2021. DOI: 10.1109/TIE.2020.3026271.
- [50] G. Liu, M. Zhao, Q. Chen, W. Zhao, and X. Zhu, “Performance Comparison of Fault-Tolerant Control for Triple Redundant 3×3 -Phase Motors Driven by Mono-Inverter”, *IEEE Transactions on Transportation Electrification*, vol. 8, no. 2, pp. 1839–1852, 2022. DOI: 10.1109/TTE.2021.3115482.
- [51] Y. Luo and C. Liu, “Pre- and Post-Fault Tolerant Operation of a Six-Phase PMSM Motor Using FCS-MPC Without Controller Reconfiguration”, *IEEE Transactions on Vehicular Technology*, vol. 68, no. 1, pp. 254–263, 2019. DOI: 10.1109/TVT.2018.2883665.
- [52] Z. Song, Y. Yu, F. Chai, and Y. Tang, “Radial Force and Vibration Calculation for Modular Permanent Magnet Synchronous Machine With Symmetrical and Asymmetrical Open-Circuit Faults”, *IEEE Transactions on Magnetics*, vol. 54, no. 11, pp. 1–5, 2018. DOI: 10.1109/TMAG.2018.2848724.

- [53] B. Tian, Q.-T. An, J.-D. Duan, D. Semenov, D.-Y. Sun, and L. Sun, “Cancellation of Torque Ripples With FOC Strategy Under Two-Phase Failures of the Five-Phase PM Motor”, *IEEE Transactions on Power Electronics*, vol. 32, no. 7, pp. 5459–5472, 2017. DOI: 10.1109/TPEL.2016.2598778.
- [54] S. Dwari and L. Parsa, “An Optimal Control Technique for Multiphase PM Machines Under Open-Circuit Faults”, *IEEE Transactions on Industrial Electronics*, vol. 55, no. 5, pp. 1988–1995, 2008. DOI: 10.1109/TIE.2008.920643.
- [55] N. Bianchi, S. Bolognani, and M. Dai Pre, “Strategies for the Fault-Tolerant Current Control of a Five-Phase Permanent-Magnet Motor”, *IEEE Transactions on Industry Applications*, vol. 43, no. 4, pp. 960–970, 2007. DOI: 10.1109/TIA.2007.900445.
- [56] Z. Li, L. Wu, Z. Chen, Y. Shi, L. Qiu, and Y. Fang, “Single- and Two-Phase Open-Circuit Fault Tolerant Control for Dual Three-Phase PM Motor Without Phase Shifting”, *IEEE Access*, vol. 8, pp. 171 945–171 955, 2020. DOI: 10.1109/ACCESS.2020.3024736.
- [57] C. Xiong, T. Guan, P. Zhou, and H. Xu, “A Fault-Tolerant FOC Strategy for Five-Phase SPMSM With Minimum Torque Ripples in the Full Torque Operation Range Under Double-Phase Open-Circuit Fault”, *IEEE Transactions on Industrial Electronics*, vol. 67, no. 11, pp. 9059–9072, 2020. DOI: 10.1109/TIE.2019.2950851.
- [58] A. Mohammadpour, S. Mishra, and L. Parsa, “Iterative learning control for fault-tolerance in multi-phase permanent-magnet machines”, in *2013 American Control Conference*, Washington, DC, USA, 2013, pp. 5929–5934. DOI: 10.1109/ACC.2013.6580768.
- [59] A. Mohammadpour, S. Sadeghi, and L. Parsa, “A Generalized Fault-Tolerant Control Strategy for Five-Phase PM Motor Drives Considering Star, Pentagon, and Pentacle Connections of Stator Windings”, *IEEE Transactions on Industrial Electronics*, vol. 61, no. 1, pp. 63–75, 2014. DOI: 10.1109/TIE.2013.2247011.
- [60] B. Tian, L. Sun, M. Molinas, and Q.-T. An, “Repetitive Control Based Phase Voltage Modulation Amendment for FOC-Based Five-Phase PMSMs Under Single-Phase Open Fault”, *IEEE Transactions on Industrial Electronics*, vol. 68, no. 3, pp. 1949–1960, 2021. DOI: 10.1109/TIE.2020.2975502.

Bibliography

- [61] J. Ji, Y. Zhou, T. Tao, Z. Li, and W. Zhao, “Armature MMF Reconfiguration Method of Six-Phase Integral-Slot PMSMs for Zero-Order Vibration Reduction Under Open-Circuit Faults”, *IEEE Transactions on Transportation Electrification*, vol. 10, no. 1, pp. 421–431, 2024. DOI: 10.1109/TTE.2023.3266612.
- [62] S. X. Ding, *Data-Driven Design of Fault Diagnosis and Fault-Tolerant Control Systems*, 1st ed. London, UK: Springer, 2014. DOI: 10.1007/978-1-4471-6410-4.
- [63] Z. Gao, C. Cecati, and S. X. Ding, “A Survey of Fault Diagnosis and Fault-Tolerant Techniques—Part I: Fault Diagnosis With Model-Based and Signal-Based Approaches”, *IEEE Transactions on Industrial Electronics*, vol. 62, no. 6, pp. 3757–3767, 2015. DOI: 10.1109/TIE.2015.2417501.
- [64] Z. Gao, C. Cecati, and S. X. Ding, “A Survey of Fault Diagnosis and Fault-Tolerant Techniques—Part II: Fault Diagnosis with Knowledge-Based and Hybrid/Active Approaches”, *IEEE Transactions on Industrial Electronics*, vol. 62, no. 6, pp. 3768–3774, 2015. DOI: 10.1109/TIE.2015.2419013.
- [65] S.-G. Ahn, B.-G. Park, R.-Y. Kim, and D.-S. Hyun, “Fault diagnosis for open-phase faults of permanent magnet synchronous motor drives using Extended Kalman Filter”, in *IECON 2010 - 36th Annual Conference on IEEE Industrial Electronics Society*, Glendale, AZ, USA, 2010, pp. 835–840. DOI: 10.1109/IECON.2010.5675176.
- [66] I. Jlassi, J. O. Estima, S. K. El Khil, N. M. Bellaaj, and A. J. M. Cardoso, “A Robust Observer-Based Method for IGBTs and Current Sensors Fault Diagnosis in Voltage-Source Inverters of PMSM Drives”, *IEEE Transactions on Industry Applications*, vol. 53, no. 3, pp. 2894–2905, 2017. DOI: 10.1109/TIA.2016.2616398.
- [67] M. J. Duran, I. Gonzalez-Prieto, N. Rios-Garcia, and F. Barrero, “A Simple, Fast, and Robust Open-Phase Fault Detection Technique for Six-Phase Induction Motor Drives”, *IEEE Transactions on Power Electronics*, vol. 33, no. 1, pp. 547–557, 2018. DOI: 10.1109/TPEL.2017.2670924.
- [68] J. O. Estima and A. J. Marques Cardoso, “A New Approach for Real-Time Multiple Open-Circuit Fault Diagnosis in Voltage-Source Inverters”, *IEEE Transactions on Industry Applications*, vol. 47, no. 6, pp. 2487–2494, 2011. DOI: 10.1109/TIA.2011.2168800.
- [69] D. U. Campos-Delgado, J. A. Pecina-Sánchez, D. R. Espinoza-Trejo, and E. R. Arce-Santana, “Diagnosis of open-switch faults in variable speed drives by stator current analysis and pattern recognition”, *IET Electric*

- Power Applications*, vol. 7, no. 6, pp. 509–522, 2013. DOI: 10.1049/iet-epa.2013.0015.
- [70] J. O. Estima and A. J. Marques Cardoso, “A New Algorithm for Real-Time Multiple Open-Circuit Fault Diagnosis in Voltage-Fed PWM Motor Drives by the Reference Current Errors”, *IEEE Transactions on Industrial Electronics*, vol. 60, no. 8, pp. 3496–3505, 2013. DOI: 10.1109/TIE.2012.2188877.
- [71] F. Meinguet *et al.*, “A signal-based technique for fault detection and isolation of inverter faults in multi-phase drives”, in *2012 IEEE International Conference on Power Electronics, Drives and Energy Systems (PEDES)*, Bengaluru, India, 2012, pp. 1–6. DOI: 10.1109/PEDES.2012.6484321.
- [72] H. Mesai-Ahmed, I. Jlassi, A. J. M. Cardoso, and A. Bentaallah, “Multiple Open-Circuit Faults Diagnosis in Six-Phase Induction Motor Drives Using Stator Current Analysis”, *IEEE Transactions on Power Electronics*, vol. 37, no. 6, pp. 7275–7285, 2022. DOI: 10.1109/TPEL.2021.3132236.
- [73] I. González-Prieto, M. J. Duran, N. Rios-Garcia, F. Barrero, and C. Martín, “Open-Switch Fault Detection in Five-Phase Induction Motor Drives Using Model Predictive Control”, *IEEE Transactions on Industrial Electronics*, vol. 65, no. 4, pp. 3045–3055, 2018. DOI: 10.1109/TIE.2017.2748052.
- [74] M. Trabelsi, E. Semail, and N. K. Nguyen, “Experimental Investigation of Inverter Open-Circuit Fault Diagnosis for Biharmonic Five-Phase Permanent Magnet Drive”, *IEEE Journal of Emerging and Selected Topics in Power Electronics*, vol. 6, no. 1, pp. 339–351, 2018. DOI: 10.1109/JESTPE.2017.2719634.
- [75] J. Kong, K. Wang, J. Zhang, and H. Zhang, “Multiple Open-Switch Fault Diagnosis for Five-Phase Permanent Magnet Machine Utilizing Currents in Stationary Reference Frame”, *IEEE Transactions on Energy Conversion*, vol. 36, no. 1, pp. 314–324, 2021. DOI: 10.1109/TEC.2020.3011840.
- [76] J. Sun, C. Li, Z. Zheng, K. Wang, and Y. Li, “A Generalized, Fast and Robust Open-Circuit Fault Diagnosis Technique for Star-connected Symmetrical Multiphase Drives”, *IEEE Transactions on Energy Conversion*, vol. 37, no. 3, pp. 1921–1933, 2022. DOI: 10.1109/TEC.2022.3150759.
- [77] G. Forstner, A. Kugi, and W. Kemmetmüller, “A Magnetic Equivalent Circuit Based Modeling Framework for Electric Motors Applied to a PMSM With Winding Short Circuit”, *IEEE Transactions on Power Electronics*, vol. 35, no. 11, pp. 12 285–12 295, 2020. DOI: 10.1109/TPEL.2020.2986042.
- [78] V. Ostović, *Dynamics of Saturated Electric Machines*, 1st ed. New York, USA: Springer, 1989. DOI: 10.1007/978-1-4613-8933-0.

Bibliography

- [79] G. Forstner, A. Kugi, and W. Kemmetmüller, “Fault-tolerant torque control of a three-phase permanent magnet synchronous motor with interturn winding short circuit”, *Control Engineering Practice*, vol. 113, 104846, 2021. DOI: 10.1016/j.conengprac.2021.104846.
- [80] P. C. Krause, O. Wasynczuk, S. D. Sudhoff, and S. Pekarek, *Analysis of Electric Machinery and Drive Systems*, 3rd ed. Hoboken, NJ, USA: John Wiley & Sons, 2013. DOI: 10.1002/9781118524336.
- [81] A. Kugi, *Non-Linear Control Based on Physical Models*, 1st ed. London, UK: Springer, 2001. DOI: 10.1007/BFb0110339.
- [82] D. C. Hanselman, *Brushless Permanent Magnet Motor Design*, 2nd ed. Lebanon, OH, USA: Magna Physics Publishing, 2006.
- [83] S. D. Sudhoff, *Power Magnetic Devices: A Multi-Objective Design Approach*, 2nd ed. Hoboken, NJ, USA: John Wiley & Sons, 2021.
- [84] N. Christofides, *Graph Theory: An Algorithmic Approach*, 1st ed. New York, USA: Academic Press, 1975.
- [85] V. Berdichevsky, *Variational Principles of Continuum Mechanics: I. Fundamentals*. Berlin, Heidelberg, Germany: Springer, 2009. DOI: 10.1007/978-3-540-88467-5.
- [86] H. A. Toliyat, Ed., *Electric Machines: Modeling, Condition Monitoring, and Fault Diagnosis*, 1st ed. Boca Raton, FL, USA: Taylor & Francis, 2013. DOI: 10.1201/b13008.
- [87] dSpace, *PHS Bus System Hardware Reference*, 2021. [Online]. Available: https://www.dspace.com/en/pub/home/support/documentation.cfm?helpsetid=PHSBusSystemHardwareReference&externalid=Book_ov-00000004-0000-360f-0201-000000000001_--_&Language=en-us&Release=RLS2021-A (visited on 04/09/2024).
- [88] Infineon, *BTN8982TA manual*, 2013. [Online]. Available: https://www.infineon.com/dgdl/Infineon-BTN8982TA-DS-v01_00-EN.pdf?fileId=db3a30433fa9412f013fbc32289b7c17 (visited on 04/09/2024).
- [89] J. A. E. Andersson, J. Gillis, G. Horn, J. B. Rawlings, and M. Diehl, “CasADi: A software framework for nonlinear optimization and optimal control”, *Mathematical Programming Computation*, vol. 11, no. 1, pp. 1–36, 2019. DOI: 10.1007/s12532-018-0139-4.
- [90] A. Wächter and L. T. Biegler, “On the implementation of an interior-point filter line-search algorithm for large-scale nonlinear programming”, *Mathematical Programming*, vol. 106, no. 1, pp. 25–57, 2006. DOI: 10.1007/s10107-004-0559-y.

- [91] G. Bi, G. Zhang, G. Wang, Q. Wang, Y. Hu, and D. Xu, “Adaptive Iterative Learning Control-Based Rotor Position Harmonic Error Suppression Method for Sensorless PMSM Drives”, *IEEE Transactions on Industrial Electronics*, vol. 69, no. 11, pp. 10 870–10 881, 2022. DOI: 10.1109/TIE.2021.3120444.
- [92] S. A. Q. Mohammed, A. T. Nguyen, H. H. Choi, and J.-W. Jung, “Improved Iterative Learning Control Strategy for Surface-Mounted Permanent Magnet Synchronous Motor Drives”, *IEEE Transactions on Industrial Electronics*, vol. 67, no. 12, pp. 10 134–10 144, 2020. DOI: 10.1109/TIE.2019.2962454.
- [93] S. Mandra, K. Galkowski, and H. Aschemann, “Robust guaranteed cost ILC with dynamic feedforward and disturbance compensation for accurate PMSM position control”, *Control Engineering Practice*, vol. 65, pp. 36–47, 2017. DOI: 10.1016/j.conengprac.2017.05.004.
- [94] W. Qian, S. Panda, and J.-X. Xu, “Torque ripple minimization in PM synchronous motors using iterative learning control”, *IEEE Transactions on Power Electronics*, vol. 19, no. 2, pp. 272–279, 2004. DOI: 10.1109/TPEL.2003.820537.
- [95] M. Tang, P. Zanchetta, A. Gaeta, and A. Formentini, “A variable frequency angle-based repetitive control for torque ripple reduction in PMSMs”, in *8th IET International Conference on Power Electronics, Machines and Drives (PEMD 2016)*, Glasgow, UK, 2016, pp. 1–6. DOI: 10.1049/cp.2016.0325.
- [96] M. Tang, A. Gaeta, A. Formentini, and P. Zanchetta, “A Fractional Delay Variable Frequency Repetitive Control for Torque Ripple Reduction in PMSMs”, *IEEE Transactions on Industry Applications*, vol. 53, no. 6, pp. 5553–5562, 2017. DOI: 10.1109/TIA.2017.2725824.
- [97] S. F. Toloue and M. Moallem, “PMSM Torque Ripple Minimization Using an Adaptive Iterative Learning Control”, in *IECON 2020 The 46th Annual Conference of the IEEE Industrial Electronics Society*, Singapore, Singapore, 2020, pp. 335–340. DOI: 10.1109/IECON43393.2020.9255024.
- [98] A. Mohammadpour, S. Mishra, and L. Parsa, “Fault-Tolerant Operation of Multiphase Permanent-Magnet Machines Using Iterative Learning Control”, *IEEE Journal of Emerging and Selected Topics in Power Electronics*, vol. 2, no. 2, pp. 201–211, 2014. DOI: 10.1109/JESTPE.2013.2295537.
- [99] A. Wójcik and T. Pajchrowski, “Torque Ripple Compensation in PMSM Direct Drive with Position-based Iterative Learning Control”, in *2018 18th International Conference on Mechatronics - Mechatronika (ME)*, Brno, Czech Republic, 2018, pp. 1–5.

Bibliography

- [100] J. Ghosh and B. Paden, “A pseudoinverse-based iterative learning control”, *IEEE Transactions on Automatic Control*, vol. 47, no. 5, pp. 831–837, 2002. DOI: 10.1109/TAC.2002.1000282.
- [101] A. Deutschmann-Olek, G. Stadler, and A. Kugi, “Stochastic Iterative Learning Control for Lumped- and Distributed-Parameter Systems: A Wiener-Filtering Approach”, *IEEE Transactions on Automatic Control*, vol. 66, no. 8, pp. 3856–3862, 2021. DOI: 10.1109/TAC.2020.3028839.
- [102] A. M. Hava and E. Un, “Performance Analysis of Reduced Common-Mode Voltage PWM Methods and Comparison With Standard PWM Methods for Three-Phase Voltage-Source Inverters”, *IEEE Transactions on Power Electronics*, vol. 24, no. 1, pp. 241–252, 2009. DOI: 10.1109/TPEL.2008.2005719.
- [103] S. A. Khajehoddin, M. Karimi-Ghartemani, P. K. Jain, and A. Bakhshai, “A Resonant Controller With High Structural Robustness for Fixed-Point Digital Implementations”, *IEEE Transactions on Power Electronics*, vol. 27, no. 7, pp. 3352–3362, 2012. DOI: 10.1109/TPEL.2011.2181422.
- [104] A. G. Yepes, F. D. Freijedo, J. Doval-Gandoy, Ó. López, J. Malvar, and P. Fernandez-Comesaña, “Effects of Discretization Methods on the Performance of Resonant Controllers”, *IEEE Transactions on Power Electronics*, vol. 25, no. 7, pp. 1692–1712, 2010. DOI: 10.1109/TPEL.2010.2041256.
- [105] A. G. Yepes, F. D. Freijedo, Ó. Lopez, and J. Doval-Gandoy, “High-Performance Digital Resonant Controllers Implemented With Two Integrators”, *IEEE Transactions on Power Electronics*, vol. 26, no. 2, pp. 563–576, 2011. DOI: 10.1109/TPEL.2010.2066290.
- [106] P. F. C. Gonçalves, S. M. A. Cruz, and A. M. S. Mendes, “Online Diagnostic Method for the Detection of High-Resistance Connections and Open-Phase Faults in Six-Phase PMSM Drives”, *IEEE Transactions on Industry Applications*, vol. 58, no. 1, pp. 345–355, 2022. DOI: 10.1109/TIA.2021.3120239.